Structural Evolution During Spark Plasma Sintering, Oxidation and Crystallization of Iron-Based Metallic Glass

By

Tanaji Paul

Master of Engineering in Materials Engineering
Indian Institute of Science
Bangalore, India
2014

Bachelor of Engineering in Metallurgy and Materials Engineering
Bengal Engineering and Science University
Shibpur, India
2012

Submitted to the Faculty of the
Graduate College of the
Oklahoma State University
in partial fulfillment of
the requirements for
the Degree of
Doctor of Philosophy
May 2019

Structural Evolution During Spark Plasma Sintering, Oxidation and Crystallization of Iron-Based Metallic Glass

Dissertation Approved:

Dr. Sandip P. Harimkar

Dissertation Adviser

Dr. A. Kaan Kalkan

Dr. Hadi Noori

Dr. Hitesh D. Vora

ACKNOWLEDGEMENTS

My heartfelt gratitude goes to my doctoral adviser, Dr. Sandip P. Harimkar, Associate Professor, School of Mechanical and Aerospace Engineering. Right from the beginning of my doctoral research he had always introduced me to new scientific ideas, experimental routes and analytical techniques. I am fortunate to have never run out of topics to explore during the course of my research. Throughout this journey I have learned immensely from him regarding the scientific procedure of communication, specifically writing and presenting to my peers. Whenever I felt stuck lost within the immense ocean of scientific complexity he was always present to show me the way. Without his presence this thesis and me would not have been what they are. My utmost appreciation for the American people and the Federal Government for promoting STEM education among students and investing public tax dollars for realizing it. This material is based upon work supported by the National Science Foundation under Grant No. CMMI-1462602. I also thank the NSF INTERN program. I cannot overstate the herculean effort put forward by the United States Department of Energy, Scientific User Facilities Division, Office of Basic Energy Sciences for establishing

Acknowledgements reflect the views of the author and are not endorsed by committee members or Oklahoma State University

and maintaining the amazing facilities and welcoming researchers from all over the world. My warm regards to Dr. Daniel Fisher, Head of the School of Mechanical and Aerospace Engineering for his kind permission to utilize the department facilities and support whenever necessary. My huge indebtedness to Dr. Jan Ilavsky and Dr. Ivan Kuzmenko, Beamline Scientists at 9-ID Ultra-small Angle X-Ray Scattering Beamline, the Advanced Photon Source, experiments and analysis of data was instrumental in my learning of the complex theories of small angle scattering. Overnight experiments, which Argonne National Laboratory for their guidance. Their tireless efforts in appeared to be extremely daunting felt like a walk in the park for the presence and advice of Dr. Matthew G. Frith. The quality of work achieved in this thesis is largely due to the expertise offered by Dr. Narendra B. Dahotre and Dr. Shravana Katakam. Complex transmission electron microscopy seemed extremely simplified due to their experience. My heartfelt regards for the excellent opportunity for collaboration facilitated by Dr. Arvind Agarwal at Florida International University. Working with Archana was one of the most enjoyable phases during my doctoral research who became a wonderful friend and colleague even at ACerS PCSA. My articles were improved manifold due to the enriching discussions with Dr. Ravi Sankar Kottada and Dr. Niraj Chawake. It was solely due to your efforts that collaboration across 3 different time zones in the world seemed so easy. I particularly enjoyed the lectures by Dr. A. Kaan Kalkan on a diverse range of fields like nanostructured materials, corrosion engineering and thermodynamics. Dr. Kalkan's classes felt less like graduate courses and more like fun-filled chats. The home-

Acknowledgements reflect the views of the author and are not endorsed by committee members or Oklahoma State University

made cakes and dinners at the completion of courses would forever be etched in my mind. My research on characterization of materials was facilitated largely by the X-ray diffraction facility at Dr. James Puckette's laboratory. I could acquire excellent high-resolution scanning electron micrograph images and energy dispersive spectroscopic data due to the untiring help and guidance of Brent and Lisa. I also thank all the peer-reviewers, editors and publishers for permitting me to utilize the academic journals as vehicles for disseminating our research findings. Doctoral research, apparently stressful was mellowed, largely due to the presence of amazing labmates like Ashish, Habib, Sourabh, Bindu and Navin. The wonderful administrative work done by Dr. Charlotte Fore, Beth Powers, Chelsea Schaffer and Diane Compton helped me immensely. They took away the attention otherwise drawn towards paperwork that let me study and do experiments. The two of you deserve a huge thanks for being such awesome roommates. I enjoyed every second of the years I spent in our apartment. Groceries, cooking and other household chores actually felt enjoyable with you guys. I am glad that I could share so may things with you during the course of my Ph.D. That helped me a lot to do deal with the problems, both academic and non-academic. The person I am today is a result of the love you showered on me. I learned the biggest lessons from you. Thank you for such a great upbringing and supporting me through the struggles of life. This thesis is but a minute token of gratitude to the immense warmth that I received from you.

Acknowledgements reflect the views of the author and are not endorsed by committee members or Oklahoma State University

Name: Tanaji Paul

Date of Degree: May 2019

Title of Study: Structural Evolution During Spark Plasma Sintering, Oxidation and Crystallization of Iron-Based Metallic Glass

Major Field: Mechanical Engineering

Abstract:

Metallic glasses are a novel class of amorphous materials that have diverse potential applications due to their superior mechanical, electrochemical and tribological properties as compared to their polycrystalline counterparts. However, the requirement of extremely high cooling rates in solidification processing severely limits the manufacturing of these materials to small dimensions such as powder and ribbons. In order to circumvent this problem, this research investigates three thermal responses, namely sintering, oxidation and crystallization in an iron-based metallic glass powder. The resulting original scientific contribution of this dissertation is the establishment of the mechanism and kinetics of sintering, crystallization and oxidation in this iron based metallic glass powder. During sintering at a constant rate of heating, the activation energy of viscous flow decreases linearly with the logarithm of the heating rate while the macroscopic applied pressure is amplified three orders of magnitude to the interparticle contact pressure that enhances densification by micro-viscous flow deformation of the particles. Thermal oxidation leads primarily to the formation of Fe_2O_3 oxide as a polycrystalline shell around the powder core that increases in thickness rapidly at the beginning and slows down towards the end during isothermal oxidation. Crystallization in this iron based metallic glass powder encompasses four exothermic transformations occurring with a decreasing nucleation rate. These conclusions provide a foundation towards the development of manufacturing bulk sized metallic glass components for structural applications.

TABLE OF CONTENTS

List of Figures

List of Tables

Chapter I

Introduction

1 Amorphous solids

Solids devoid of any long range order in their constituent atoms are defined to be amorphous. The term 'amorphous' stems from the Greek roots 'a' meaning without and 'morphé' meaning shape or form. This definition distinctly distinguishes this group of solids from crystalline ones where the existence of long range order is the primary criterion. Crystalline solids exhibit a characteristic ensemble of positions in three dimensional space defined as the crystal lattice. These positions are at definite distances relative to a common point of origin in space and to one another. In other words, specific numbers can be assigned to these interatomic distances. Hence if the position of one lattice point is known, those of all others can be calculated or predicted. Atoms, molecules, ions or groups thereof occupy these positions in space to thereby resulting in a crystalline structure in the solid material. This repeating unit of single or groups of atoms, molecules, ions with characteristic lattice spac-

ings lies in the heart of the crystalline solid structure. In contrast, the ensemble of positions in three dimensional space for an amorphous solid is completely disordered. These positions are thus at varying distances relative to one another and it is not possible to assign a characteristic value to these distances. Even if the position of one lattice point in an amorphous solid be known, those of others cannot be predicted as in the case of a crystalline solid. Thus a repeating unit, characteristic of a particular amorphous solid, cannot be identified. This is valid even to the extent that in case of two amorphous solids of identical composition synthesized with identical dimensions, the position of identical atoms relative to the same point of origin in space may be different. This disordered atomic structure is the soul of amorphous solids and is the primary reason behind the fascinating properties exhibited by them [7].

Amorphous structures are exhibited by a large number of materials in a diverse range of forms. A number of polymers utilized daily such as low density polyethylene ('plastic') used for manufacturing bottles and toys, polyvinyl chloride (PVC) [8] in drainage pipes, Bakelite^{TM} [9] in wire insulators, Nylon^{TM} [10] used as fabric and Teflon^{TM} used in non-stick pans posses amorphous structure. One of the forms of non-crystalline carbon, commonly referred to as 'soot' is another example of a solid amorphous material. Metals, alloys and ceramics are often synthesized by various physical and chemical vapor deposition techniques that result in amorphous solid layers on substrates.

2 Metallic glasses

Glasses constitute a sub-group of materials within the broad class of amorphous solids that exhibit a characteristic 'glass transition' when cooled from their liquid state or heated from their solid state. They exist as an intermediate state between liquids and solids. According to the conventional definition, liquids do not exhibit any long range order as well as have low interatomic bonding. Solids, in general posses both long range order and very strong interatomic bonding. Glasses exhibit the disordered atomic arrangement like liquids while simultaneously possessing the strong interatomic bonding as observed in solids.

Metals, on the other hand are defined to constitute the group of solids where the interatomic bonding is metallic in nature. They can be any of the about 90 pure metals in the periodic table such as iron (Fe), aluminum (Al), lithium (Li), chromium (Cr) and so on. It can be a a mixture of multiple pure metals. A very common example is that of bronze, an alloy of copper (Cu) and tin (Sn). It can also be an alloy of multiple pure metals and non-metals. The most common example is stainless steel which is an alloy of metallic iron, chromium and nickel (Ni) and non-metallic carbon (C) and other elements.

The history of both metals and glasses dates back several millenia. Gold has been known to humans since as early as 6000 B.C. In the Stone Age, the popularity of gold stemmed primarily due to its luster and scarcity which are the same reasons of its value at present day. Gold was one of the first metals humans utilized as it could be found in its pure form naturally due to it stability against oxidation. A significant usage of metal came with the utilization of copper and its alloy with tin that ushered the Bronze Age around 2500

B.C. The next landmark was that of the Iron Age around 1200 B.C. This heralded a major era of human civilization and a large number of iron based alloys are utilized at present in daily human necessities.

Archaeological evidence of 'obsidian' [11], a naturally occurring volcanic glass, has been obtained also as early as the Stone Age. This vitreous solid is formed when lava from volcano cools rapidly with very little growth of crystals. It is high in silicon content and forms the earliest predecessor of the broad class of common silicate glasses commonly used in window panes and decorative objects. Its high hardness was utilized for making cutting an hunting tools such as sharp blades and arrowheads but at the same time was brittle in nature. The development of metals and glasses thus progressed independently over the same period of time starting about 8000 years ago.

The development of metallic glasses, in contrast, is comparatively new. The first report of a metallic system existing in glassy form was that of a gold-silicon alloy, again utilizing the high viscosity brought about in a system due to the presence of silicon. The alloy with composition of $Au_{75}Si_{25}$ (at.%) was reported [12] to be produced in the form of a ribbon by rapidly quenching the liquid alloy melt at an extremely fast cooling rate of about $10^6\,\mathrm{K\,s^{-1}}$. It clearly demonstrated that the formation of thermodynamically stable crystalline phases by nucleation and growth can be completely avoided by tailored kinetics to process metastable amorphous alloys, for example, in Pd-based alloy systems such as Pd-Cu-Si and Pd-Ag-Si [13]. Fundamental investigations laid the foundations of understanding the key criteria of forming metallic glasses. These can be summarized in three empirical

rules [14] for metallic glass formation, namely,

- The existence of a multicomponent system with more than three elements
- A mismatch in the sizes of constituent atoms by about 14% and
- A large negative heat of mixing.

This understanding has led to the development of metallic glasses in a wide range of alloy systems over the last five decades. These can classified into two broad groups, namely metal-metal and metal-metalloid. Further categories based on the groups in the periodic table and the metallic glasses reported are tabulated below [15]. One of the foremost commercial metallic glasses is $Zr_{41}Ti_{14}Cu_{12}Ni_{10}Be_{23}$ or *Vitreloy 1*^{R} [16]. It was followed by a number of metallic glasses in similar systems such as Pd-Cu-Ni-P [17], Pt-Co-Ni-Cu-P [18], Ti-Ni-Cu-Sn [19], Ni-Zr-Cr-B [20] and La-Al-Ni-Cu-Co [21].

It can be immediately observed that the constituent elements in these metallic glasses are extremely expensive. The attention thus naturally shifted to the development of comparatively cheaper iron based metallic glasses [22]. Following the first in this group, namely Fe-Al-Ga-P-C-B [23], a large number of alloy systems have been reported to form metallic glasses by a variety of processing techniques. In these iron based metallic glasses, the typical elements such as iron, chromium, cobalt, molybdenum and nickel constitute about 80% of the alloy composition while the rest 20% is a mixture of metalloids such as boron and silicon. For example, one of the alloys of key importance in this group is $Fe_{50}Cr_{15}Mo_{14}C_{15}B_6$ that is often referred to as 'amorphous steel'. Considerable research is focused on modifying this alloy by addition of rare earth elements such as Dy, Er, Tm and Y [24, 25] for improving its

Table 1: Classification of elements forming metallic glass alloy systems and their examples

Group in Periodic Table	Example of metallic glass system
Group IA and Group IIA Metals	Ca, Be, Mg
Group IIA and Group IVA Metals	Al, Ga
Group IVB to Group VIIB Metals	Ti, Zr, Hf, Nb, Ta, Cr, Mo, Mn
Group IB, Group IIB and Group VIIIB Metals	Fe, Co, Ni, Cu, Pd, Pt, Ag, Au, Zn
Sc, Y and lanthanides	Sc, Y, La, Ce, Nd, Gd
Nonmetals and metalloids	B, C, P, Si, Ge

properties. $Fe_{48}Cr_{15}Mo_{14}Y_2C_{15}B_6$, in particular, exhibits a high elastic modulus of 200 GPa, compressive fracture strength of 3200 MPa, and hardness of about 13 GPa [26, 27]. Its superior wear and corrosion resistance has also been utilized as amorphous coatings [28, 29].

3 Properties and applications

High strength and large elastic limit of metallic glasses have led to their applications in a variety of sports goods such as golf clubs, baseball bats, fishing and skiing gear.The success of the golf clubs essentially stems from the repulsion efficiency of the club head and ball pair which is greater than that in conventional alloy heads. The energy transferred from the club, given by the modulus of resilience, is considerably higher that has led to successful commercialization of these metallic glass gears by Dunlop Corporation in Japan and Liquidmetal Technologies in the Unites States. The superior mechanical properties of metallic glasses can also potentially be employed in valves for automotive parts where shorter and thinner springs can reduce the total weight of engine cylinders and hence bring down the

overall fuel consumption. Metallic glasses are especially suitable for high pressure sensor diaphragms. The high Young's modulus is extremely useful for increasing the sensitivity of these components. Commercial shot peening processes require high strength, endurance against cyclic loading and corrosion resistance. Metallic glasses appear to be suitable alternative to high carbon steel balls, since mass production would be effective for reducing the cost of the spherical parts.

The amorphous nature of metallic glasses makes the materials homogeneous, even at the nanometric length scales. This is particularly suitable for manufacturing precision instruments such as micro-gears [30]. These are further utilized to fabricate micro-gear motors. The dimensions of these components have been reducing progressively over time with the smallest metallic glass motor being of 1.5 mm. Due to their small sizes and precise mobility, there exists a large potential for applications in advanced medical equipments in endoscopy, thrombus removal catheters and so on.

The corrosion resistance of metallic glasses finds potential applications in proton exchange membrane fuel cells used for domestic and automotive utility due to their high output current density and low temperature operation. This property of metallic glasses also makes them excellent candidates for applications in hard, corrosion resistant coatings applied by a number of spraying techniques such atmospheric plasma spraying, high velocity oxy-fuel spraying [31], etc. The outstanding soft magnetic properties of iron based metallic glasses makes them excellent candidates for transformers. Metallic glass ribbons with high permeability and low coercivity of are being extensively employed in cores of transformers

and in the miniaturization of micro-electro-mechanical systems (MEMS) and nano-electro-mechanical systems (NEMS). The low surface chemical reactivity of these materials also propel them for fabrication of surgical devices and instruments for biomedical applications. Replacements for hip joints, teeth and screws for fixing plates are, to name a few, some of the highly investigated areas for metallic glass applications.

4 Viscosity

The single most important physical property of metallic glasses is the viscosity. From the manufacturing perspective, it determines the glass forming ability of the alloy, the critical cooling rate for the formation of glass structure and the size of components that can be fabricated. From the point of view of materials science, it determines, among other parameters, the structure of the glasses and can be utilized to determine critical information such as the short to medium range order, coordination number and packing density in metallic glasses. These, in turn, yields insight into the structural relaxation in the metallic glasses upon annealing and hence the flow behavior of the material. Thus, overall, the dependence of viscosity of metallic glasses on temperature is essential to studying its synthesis, fabrication, properties and applications. The importance of viscosity in understanding metallic glasses is so essential that the glass transition temperature of metallic glasses is defined to be the temperature at which the viscosity attains a value of 10^{12} Pa s.

The apparent viscosity of metallic glasses at a particular temperature increases with time during isothermal annealing. After the initial increase, the viscosity saturates to a constant value at that particular temperature which is defined as the equilibrium viscosity at

that temperature. The time necessary to acquire this value is characteristic of the relaxation required by the metallic glass to attain equilibrium in the supercooled liquid region. The value of the equilibrium viscosity can be described as a function of time and temperature as

$$log\eta(t,T) = log\eta_{\mathrm{g}} + log\frac{\eta_{\mathrm{eq}}(T)}{\eta_{\mathrm{g}}}\left[1 - exp\left\{1 - \left(\frac{t}{\tau}\right)^{\beta}\right\}\right] \tag{I.1}$$

where η (Pa s) is the measured apparent viscosity, η_{g} (Pa s) is the apparent viscosity for the as cast glassy alloy, η_{eq} (Pa s) is th equilibrium viscosity at temperature T (K), t (s) is the time, τ (s) is the relaxation time for shear viscous flow and β is the stretched exponent.

4.1 Experimental measurement techniques

The apparent viscosity, η can be measured experimentally, as the resistance to shear flow at different strain rates as

$$\eta = \frac{\sigma_{\mathrm{flow}}}{\dot{\gamma}} \tag{I.2}$$

where σ_{flow} (Pa) is the equilibrium flow stress and σ_{flow} (s^{-1}) is the strain rate. This is accomplished by the three point beam bending method where the measurement of the deflection of a beam under a load and supported at two points yields the viscosity as

$$\eta = \frac{gL^3}{144I_{\mathrm{c}}v}\left(M + \frac{5\rho AL}{8}\right) \tag{I.3}$$

where g ($\mathrm{m\,s^{-2}}$) is the acceleration due to gravity, L (m) is the length span of the beam, $\mathrm{I_c}$ ($\mathrm{m^4}$) is the moment of inertia, v ($\mathrm{m\,s^{-1}}$) is the velocity of deflection, M (kg) is the mass of the applied load, ρ ($\mathrm{kg\,m^{-3}}$) is the density of the metallic glass alloy and A ($\mathrm{m^2}$) is the cross sectional area of the specimen.

4.2 Temperature dependence

At the liquidus temperature, the viscosity of metallic glasses attain values of about 0.1 to 1 Pa s. Experimental techniques for the measurement of viscosity of metallic glasses in the liquid state is challenging due to the fact that contact with surfaces of the instrument tends to behave as heterogenous nucleation sites within the liquid melt thereby impeding the measurement of the viscosity of the pure alloy melt. Additionally, transition melts used to synthesize the alloy composition of a number of metallic glasses is reactive such as Ni, Ti and Zr. Non-contact measurement such as the drop oscillation technique employed within the vacuum environment of a electrostatic levitator provides an excellent solution for the accurate measurement of both surface tension as well as viscosity of metallic glass alloys in the liquid state in a single experiment. The surface tension of the metallic glass during axisymmetric oscillations as an individual molten drop can be estimated using

$$\omega^2 = \frac{8\sigma}{\rho r^3} \tag{I.4}$$

where ω ($\mathrm{s^{-1}}$) is the resonant oscillation frequency of the molten drop of metallic glass alloy, σ ($\mathrm{N\,m^{-1}}$) is the surface tension. r (m) is the radius of the liquid drop and ρ ($\mathrm{kg\,m^{-3}}$) is the

density of the alloy. The viscosity of the alloy can be measured according to

$$\eta = \frac{\rho r^2}{5\tau} \tag{I.5}$$

where τ is the decay time constant of free oscillation of the liquid drop.

With a decrease in temperature from that of the liquid melt alloy, the viscosity of the metallic glass decreases drastically, by orders of magnitude. The dependence of viscosity of metallic glass with temperature in the supercooled liquid region, can be mathematically described by the Vogel-Fulcher-Tammann equation expressed as [32]

$$\eta = \eta_{\mathrm{o}} exp\left(\frac{B}{T - T_{\mathrm{o}}}\right) \tag{I.6}$$

where η_{o} is the pre-exponential factor and $\mathrm{T_o}$ (K) is the fictive temperature. Eq. I.6 can be rewritten as

$$\eta = \eta_{\mathrm{o}} exp\left(\frac{D^* T_{\mathrm{o}}}{T - T_{\mathrm{o}}}\right) \tag{I.7}$$

where $\mathrm{D^*}$ is the fragility parameter. Following Agnell's theory, metallic glasses, according to the equation can be classified further into two groups, depending on their fragility index. This parameter, represented as m, can be expressed as the slope, at the glass transition temperature, of the plot of viscosity of the metallic glass with the reduced glass transition temperature, $\mathrm{T_g/T}$ in a semi-log scale according to

$$m = \frac{d(log\eta)}{d(T_{\mathrm{g}}/T)}\Big|_{T=T_{\mathrm{g}}} \tag{I.8}$$

This equation accounts for the observed deviation of the viscosity in metallic glasses away from the Arrhenius equation above the glass transition temperature. Metallic glasses with lower values of the fragility index, m, or in other words, 'strong glasses' follow the Arrhenius equation right through the temperature range from below the glass transition temperature to above the supercooled liquid region. A representative strong glass is silicon dioxide whose viscosity versus temperature plot according to the above equation is a straight line across the whole temperature range. Metallic glasses are more 'fragile' in comparison to silicon dioxide exhibiting a higher value of m in the viscosity versus temperature plot.

Just below the glass transition temperature, $\mathrm{T_g}$ the viscosity of metallic glasses follows a simple Arrhenius equation of the form

$$\eta = \eta_{\mathrm{o}} exp\left(\frac{Q}{RT}\right) \tag{I.9}$$

where Q ($\mathrm{J\,mol^{-1}}$) is the activation energy barrier for viscous flow and R ($8.314\,\mathrm{J\,K^{-1}\,mol^{-1}}$) is the universal gas constant. The pre-exponential factor, η_{o} can be easily observed to be the value attained by *eta* when the temperature is close to infinity or in other words very high values. This can also be considered to be approximately equal to the viscosity of the molten of liquid metallic glass alloy. It can be measured indirectly as

$$\eta_{\mathrm{o}} = \frac{N_{\mathrm{A}} h}{V_{\mathrm{m}}} \tag{I.10}$$

where $\mathrm{N_A}$ ($6.022 \times 10^{23}\,\mathrm{mol^{-1}}$) is the Avogadro's constant, h ($6.626 \times 10^{-34}\,\mathrm{J\,s}$) is the Planck's constant and $\mathrm{V_m}$ ($\mathrm{m^3}$) is the molar volume.

4.3 Heating rate dependence

The viscosity of metallic glasses during non-isothermal annealing below their glass transition is observed to depend upon the constant rate of heating. The framework of the directional structural relaxation model is employed to derive theoretical understanding of this phenomenon. Under this model the structural relaxation of metallic glasses is considered to be a set of irreversible atomic rearrangements localized at certain atomic relaxation centers. According to this model the viscosity of metallic glasses under constant rates of annealing can be expressed as [33]

$$\eta = \frac{1}{3ACN_{\mathrm{o}}\Pi c} \tag{I.11}$$

where $\mathrm{N_o}$ is the number of relaxation centers per unit activation energy and volume, Π is the volume throughout which the structural relaxation occurs, C accounts for the orientation of the external stress and resultant viscosity, A is the activation energy associated with the relaxation phenomenon and c is the heating rate. The term, $\mathrm{3ACN_o}$ is dependent solely on the temperature. Hence Eq. I.11 predicts that isothermal sections of plots of η versus T dependencies should exhibit a linear relationship with the inverse of the heating rate.

5 Manufacturing challenges

Metallic glasses have been manufactured in a large number of alloy systems with the best results in terms of dimensions and mechanical properties being exhibited by palladium, platinum, zirconium, titanium and neodymium. However, these materials are extremely rare and expensive due to their specialized extraction processes. It is imperative for large scale, industrial applications that metallic glasses with reliable properties be produced economically. This necessitates the manufacturing of metallic glasses with considerably cheaper metals that offer the same superior advantages in terms of mechanical and corrosion properties.

In this regard, iron based metallic glasses are especially attractive due to their low cost. They also exhibit high strength in addition to possessing good soft magnetic properties such as high saturation magnetization and low coercivity. However, manufacturing iron based metallic glasses presents a major challenge due to their limited glass forming ability. During conventional solidification processing of metallic glasses, heat must be removed from the alloy liquid melt to 'freeze' the constituent atoms in a disordered state. This requires high cooling rates being indispensable for retaining fully amorphous structure in bulk sized iron based metallic glass components. These cooling rates can be achieved only if the dimension of the metallic glass component in the direction of extraction of heat is extremely small up to about a few micro meters. Hence the majority of iron based metallic glasses are manufactured in the forms of ribbons, wires and powders. For example, Fe-Si-B ribbons are extensively employed as cores in transformers. However, major large scale applications of metallic glasses for structural components are severely limited. Thus it is critical to develop

manufacturing techniques for large scale production of bulk iron based metallic glasses for utilization of their superior properties.

6 Sintering

Sintering as a fabrication process is almost as old as human civilization itself. Usage of primitive forms of the process is frozen in the numerous archaeological findings unearthed in the cradles of early human civilizations and the products are found to date back millennia. Much prior to the advent of written records, there lies only historical evidence that suggest the utilization of rudimentary firing techniques that were applied to clay ceramics to make pots and vessels used for storing water. Advances in the design of kilns enabled higher firing temperatures to be acquired which paved the way for the usage of highly valuable porcelain in dishes found in China at the times of the Tsing dynasty. Trade routes along numerous directions spread both the products and technologies in countries like Turkey, Italy and Japan. This generated enthusiasm to realize such products in and around the European mainland.

Emergence of sintered metallic objects followed as exemplified by sintered iron artifacts found in Tutankhamens tomb in Egypt, the Delhi Iron Pillar in India, sintered platinum crucibles and gold-platinum jewelery found in the Inca civilizations. A landmark in the history of sintering was the development of a sintered filament using tungsten powder by Coolidge that was to be applied in the electric bulb. The preservation of ductility in a sintered filament brought about by the low oxygen impurity content and grain boundary pinning by sodium silicate and alumina dispersoids was critical to the success of Coolidges

filament design [34].

Production of filaments demanded the making of durable dies which would enable the drawing of wires made out of such hard metals. Synthesis of carbides of tungsten along with additions of molybdenum carbides, iron and transition metals preceded the eventual sintering of tungsten carbide with additions of cobalt enabling liquid phase sintering to form a tungsten carbide-cobalt composite. This was the fruit of a collaboration of several giants in the field like DGA, Siemens Lap and AEG who filed patents which were later used by companies like Krupp and General Electric. This can be seen as advent of industrial giants utilizing sintering process for the large scale manufacturing of products.

6.1 Theory

Considerable success was achieved in making products by varying sintering processes without any understanding of the underlying phenomena that were involved therein. Even now it is seen that progress in practice stood way ahead of theory. As diverse observations were made in this regard, production could be achieved without the need of a quantitative theory. Additionally, emergence of quantitative theory was thwarted by the absence of concrete knowledge about the structure of atoms, their arrangement and motion in a solid or liquid body and ideas like surface energy and microstructure. Inability of accurate measurement of temperature and realization of versatile furnaces also limited its development.

The first step in quantitative sintering theory emerged in the form of a two sphere model described by Frenkel in which he explained sintering to occur in two different but often overlapping steps. The first stage involves the increase in the contact area between

two particles due to viscous flow driven by a reduction in surface energy resulting in the formation of pores. This is followed by the second stage where the above pores, treated as a huge agglomeration of vacancies, are overrun by atomic diffusion occurring throughout the volume of the material. Although this model ignored crystal structure and hence any interparticle grain boundary or dihedral angle thus being applicable only to amorphous materials, nevertheless was a starting point on which further advances could be built upon. Further additions of the neck growth model and shrinkage theory followed by liquid phase sintering problem bolstered the foundations of this phenomenon.

Frenkels theory on the viscous flow of materials was the necessary spark that ignited a string of research activities on sintering phenomena. The outcome was a large number of independent treatments and improvements of various explanations of the myriad of events that constitute sintering. About three stages of sintering can roughly be identified which although overlap with and cannot be separated from one another, have their own characteristic features.

6.2 Neck growth

Small particles when packed close together are attracted to one another due to weak atomic forces like van der Waals forces. These cohesive forces create a small bond at the point of contact between two particles which is called the 'neck'. Short range atomic motion occurring mostly at the surface of the particles during this initial stage results in the growth of this neck. The curvatures, namely, convex at the surface of the particles and concave at the neck give rise to a conspicuous saddle point in the middle, a unique feature observed

during sintering of powders. In this stage each neck, a considerable distance apart from its neighboring ones, grows independent of each other giving to rise to grain boundaries in case of crystalline materials. As they enlarge they require progressively increasing amount of material to grow further which results in a gradually slackening rate of neck growth giving way to the next stage.

6.3 Pore rounding

Towards the end of the initial stage, the pores between particles have sharp ends due to the existence of both convex and concave curvatures as mentioned above. The flow of mass makes the pores, residing mostly at the grain edges, rounded as porosity slowly declines. Towards the end of this stage the sintered mass consists of a collection of grains that are bounded by tubular pores that form an open interconnected network.

6.4 Pore closure

The final stage is usually dominated by grain growth driven by a reduction in the grain boundary area and hence energy of the same. This is accompanied by further densification which results in an increase in length and decrease in diameter of the aforementioned tubular pores. Eventually these open tubular pores pinch into closed spherical ones driven by a reduction in surface energy. This is analogous to the breaking up of a long and thin stream of water into discrete smaller droplets. The distribution in size of these spherical pores leads to their coalescence often with simultaneous growth of larger and shrinkage of smaller pores. These are the final stages of densification which is often impeded by gases trapped in these

pores.

6.5 Geometric evolution

As mentioned above, the contact between two particles contains both convex and concave surfaces. Contrary to a flat surface which is considered to be stress free, convex and concave surfaces are associated with tensile and compressive stresses respectively. The curvature and resulting stress gradients provides the driving force for the shrinkage of the convex surface which provides the flow of mass for neck growth. At this stage sintering takes place mostly by surface diffusion as the neck continuously tries to achieve the minimum energy profile.

With further progress in sintering, the driving force for sintering shifts from removal of curvature gradients to reduction of interfacial energy which can be achieved by a decrease in both surface and grain boundary area. The specific energy of free surfaces is considerably higher than grain boundaries which results in their preferential removal followed by grain growth in the later stages which ultimately results in the network of tubular pores along the grain edges.

The size and morphology of grains play an important role in sintering and are crucial in determining final porosity and relevant mechanical properties of the final sintered product. The initial contacts between particles are the origin of the grain boundaries which are high if the number of particles contacting one another (coordination number) is high. Densification is brought about by diffusion along grain boundaries as opposed to grain growth which is due to diffusion across them. Thus a high number of grain boundaries assist in sintering

densification. On the contrary, particles starting with low coordination number result in a large number of pores or cracks in the final sintered product which are derogatory to its mechanical properties.

During the initial stages of sintering, pores are angular in shape which gradually smoothen and become rounded as sintering progresses. Pores that larger in size or are surrounded by a large number of grains tend to grow at the cost of shrinkage of those which are small or are bounded by a smaller number of grains. Thus before the advent of heating it is beneficial to have smaller particles but the agglomeration of these particles deters densification. For theoretical considerations, pores are considered to be high local concentration of vacancies which diffuse to grain boundaries, free surfaces and interfaces due to the high temperatures of sintering and get annihilated resulting in reduction of porosity.

The sum of surface areas of pore and grain boundary is greater than the interfacial area had the pores been attached to the grain boundaries. Thus there is a natural tendency for the pores to bind to the grain boundaries. During grain growth these pores exert a drag on the grain boundaries which result in them getting bowed. However with increasing densification, as the pores shrink and the binding energy decreases the pores start to get detached from the grain boundaries. Since these are then trapped inside the grains further densification is not possible and hence during later stages the rate of densification slows down considerably.

6.6 Mass transport mechanisms

The importance of mass transport in sintering cannot be overemphasized. As encountered numerous times in the preceding treatments, varying driving forces affect one form of mass flow or the other. Mass transport occurring during sintering can be broadly classified into two forms

- Surface transport
- Bulk transport

The critical distinguishing factor between the two is the occurrence of densification which can only be brought about by bulk transport. Surface transport works mostly to achieve neck growth with considerable contribution from bulk transport as well. The reason behind this is that the former only involves flow of mass from one position on the surface to another while the latter results in movement from inside the solid to the surface which thereby provokes the movement of particles closer together resulting in an increase in density and shrinkage of the final sintered product. Surface transport mechanisms usually have lower activation energies thereby requiring lower temperatures for the associated phenomena to begin. Thus initial stages of sintering are usually dominated by surface transport without considerable changes in density while phenomena associated with bulk transport are manifested at a later stage.

Surface transport consists of the following

- Surface diffusion

- Volume diffusion
- Evaporation-Condensation

Bulk transport consists of

- Viscous flow
- Grain boundary diffusion
- Volume diffusion
- Dislocation motion

As seen above, volume diffusion works to enable both surface and bulk transport. Bulk transport by viscous flow is observed only in case of sintering amorphous materials or in systems that involve a liquid phase.

Surface diffusion occurs due to the defective nature of a free surface. A free surface is a collection of numerous atomic imperfections like vacancies, terraces, ledges, kinks and absorbed atoms. Mass flow due to surface transport occurs mostly due to atoms that reposition themselves from one position on the surface to another in order to reduce curvature. The concentration of these defects and the motion of atoms from one to another are both thermally activated but, they do not contribute towards densification. A number of factors dictate the amount of defects on the surface. The primary one among them is curvature. Crystal orientation also affects the concentration of surface defects. However, since particles in the green (un-sintered) product usually have all possible random orientations it is usually

ignored. Foreign atoms absorbed on the surface are usually evaporated at the high temperatures prevalent during sintering and hence their effects are generally overlooked. Surface diffusion phenomena are usually dominant at the embryonic stages of sintering when the temperatures are still increasing.

Volume diffusion can be looked upon as either the flow of atoms or vacancies. Pores can be looked upon as a large accumulation of vacancies from where they are emitted into the solid and are annihilated. The process of emission and annihilation thus involve a pair of source and sink respectively. Free surfaces, grain boundaries and dislocations are good sites for annihilation of vacancies. Stress and curvature at the surfaces, temperature and composition of the system are important factors that affect the concentration and movement of vacancies.

This process takes place only in materials which have high vapor pressure at the temperatures prevalent during sintering. Higher vapor pressures usually accompany higher temperatures resulting in higher flux of atoms.

Viscous flow is applicable to materials without crystal structures i.e. amorphous ones or systems that involve a liquid phase. In fact the first ever model of sintering proposed by Frenkel assumed particles as amorphous spheres and enumerated the rate of neck growth as a function of time during isothermal densification.

Grain boundaries are high energy regions where the bonding between atoms are disrupted and thus provide an easy path for diffusion of atoms and are a good site for annihilation of vacancies. The activation energy for diffusion through grain boundaries is

intermediate between that for volume and surface diffusion. Thus this phenomenon usually peaks during the latter stages of sintering.

Dislocation motion consists of two types of movement. Glide refers to the movement of a dislocation along a specific crystallographic plane called a slip plane and this occurs if the sintering stress is higher than the flow stress at the sintering temperature. A second movement, known as climb occurs when a vacancy gets eliminated at the core of the dislocation which in turn shifts to a parallel slip plane. Early sintering stresses due to curvature or compaction may be adequately high to induce dislocation motion. However, being non-equilibrium defects, dislocations are gradually eradicated from the system at high temperatures and thus have very little effect on densification.

6.7 Macroscopic changes

The collection of microscopic phenomena discussed so far manifests itself in various forms which can be measured in the form of changes of various macroscopic properties.

Foremost among these are the dimensional changes in the green compact brought about by the thermally activated events during sintering. Bulk transport from surface of pores to the neck brings two adjacent particles closer resulting in shrinkage. This is usually measured as the percentage change in the linear dimensions of the sintered body with respect to that of the green one. For the purpose of manufacturing finished product manufacturers thus have to provide for accurate tolerances which takes into account these changes. The shrinkage varies from one system to another and thus careful experimental evidence is necessary to achieve success in manufacturing machine parts with complicated shapes and sharp

corners. While the reduction in dimensions is mostly manifested during sintering, later stages may also bring about expansions. This may be due to any or both of thermal expansion and increase of pressure of gas trapped inside the pores. Systems that undergo reactions or phase transformations are often susceptible to swelling. Reactions between two species or phases may yield gases that may not be released due to the closed nature of pores in the final stages of sintering and thus constitutes an irreversible increase in the dimensions of the sintered body. Phase transformations occurring at high temperatures prevalent during sintering is also a major reason for swelling. Dimensional changes due to shrinkage or swelling can be measured by dilatometry. However, this procedure yields only one dimensional data and is thus not suitable for sintered compacts with complicated shapes. An alternative is direct imaging wherein the changes occurring during sintering are recorded in-situ and thus provide more insight into the anisotropy of the process.

Due to shrinkage and swelling that occur during sintering, the overall density of the sintered compact changes and the success of sintering is often measured by the amount of densification that can be achieved by the sintering cycle. Measurement of density is one of most popular indices for sintering due to ease of measurement and is usually reported as a percentage of the theoretical density of the bulk material to reduce complications due to the wide variety of systems on which sintering can be carried out. One of the primary goals is to identify the temperature and time which would result in the sintered product to acquire more than 95% of the theoretical density. However, in many cases, the difference between the theoretical and sintered density, termed porosity, is kept to a considerable amount. In

these instances having open pores close to the surface of the sintered product is critical to the application of the sintered product as in self-lubricating bearings, capacitors, etc. Density can be measured by a wide variety of experimental techniques ranging from simpler ones like direct measurement of mass and volume, Archimedes principle for complicated shapes to complicated ones like X-ray absorption, small angle neutron scattering, gamma ray absorption, magnetic resonance imaging, ultrasonic attenuation, gas pycnometry and by usage of eddy currents.

The pristine powder particles have very little strength and the mechanical properties of the sintered product is a good way to track the progress of sintering. Increase in density usually results in an increase in the strength of the sintered product. On the other hand pores cannot carry stress and may also result in the formation of cracks thereby being detrimental to the performance of the product. Standard tests for measurement of strength of sintered products include the compression test where a right circular cylinder is compressed between two flat faces till the required deformation. Sintered brittle materials are often subjected to three point bending transverse rupture test. In the Brazilian test, a sintered product in the form of a disc is crushed between two flat platens. Evolution of strength provide a lot of information about the performance of the product in a wide variety of applications.

Thermal and electrical conductivities are important properties of sintered products especially for applications in devices used in electronics and electrical power. A strong sintered compact usually provides better conductivity while it usually decreases with an increase in porosity.

Densification is usually accompanied by a reduction in surface area during sintering. It is an overall average of the surface reductions at the large number of necks formed between pairs of particles and can even be tracked when there is no shrinkage. Changes in surface area are usually measured by gas absorption, permeability of gases and to some extent by quantitative microscopy.

7 Conventional sintering limitations

Conventional sintering of metallic glasses by hot isostatic pressing exhibited that an extremely high amount of applied pressure of about 1.5 GPa is necessary to achieve >90% relative density. Additionally binders are required for the manufacturing of this compact to high density. The temperature required for achieving this density is extremely high. Such high temperatures would inevitably result in the structural transformations of the metallic glass powder such as medium range ordering, glass transition and crystallization. The inability to preserve the amorphous structure results in a deterioration of the superior properties of metallic glasses. The prolonged sintering cycles also leads to the metallic glass being annealed at the high temperatures for prolonged times that poses an additional problem.

A possible strategy to circumvent this problem would be to enable to achieve sintering at comparative lower temperatures and in shorter duration cycles. This would be possible if higher amount of energy can be input into the powder system. As compared to conventional sintering processes that utilize solely temperature and pressure, increased energy can be employed into the system by an input of electric current. Spark plasma sintering provides

the scope of employing pulsed direct current. In case of conducting powder particles the current itself aids in the enhanced compaction of the powder. Even in the case of non-conducting powder the direct current is capable of Joule heating and resultant enhancement in heating rates. This reduces the sintering temperature and cycle times for densification. Hence spark plasma sintering harbors significant potential for achieving high densification of metallic glass powder compacts without detrimental structural transformations.

8 Spark plasma sintering

A typical spark plasma sintering (SPS) machine consists of an electrically conductive vertical unit comprising of a graphite die, punches, spacers and electrodes stationed entirely inside a water cooled low pressure chamber. A low voltage, usually not more than 10 V, is maintained across the electrodes. Electric current controlled by a direct current (DC) pulse generator, that can range from 1 kA to as high as 10 kA, can be passed through the die that houses the powder material meant for sintering. In addition to conduction from the die heated by the electric current passing through it, powders can also be heated directly by the passage of the current if it is itself conductive. In either case, high heating rates from 100 to 1000 $^{\circ}\mathrm{C\,min^{-1}}$ can be employed in spark plasma sintering cycles. A simultaneous uniaxial pressure up to about 150 MPa can be transmitted to the powder through the punches. Higher pressures close to 1 GPa, however, necessitates the use of harder tungsten carbide (WC) punches. Cooling rates are usually around 150 $^{\circ}\mathrm{C\,min^{-1}}$ while those up to 400 $^{\circ}\mathrm{C\,min^{-1}}$ can be brought about by the efficient flow of gases inside the system. Although the limit of the breadth of understanding of the process has led to various nomenclatures floating in the

relevant scope like current activated and pressure assisted densification (CAPAD), electric field assisted sintering (EFAS), field assisted sintering technology (FAST) and pulsed electric current sintering (PECS), this thesis will adhere to the one most prevalent in the sintering literature, namely, spark plasma sintering.

9 Current and heating

A great bulk of phenomena taking place during spark plasma sintering cycles are brought about by the passage of electric current through the die and/or powder and concomitant heating of both of the above. In view of the daunting task of making a clear distinction between the two as being the cause of any such phenomenon since these are dependent on one another, it seems much more reasonable to explore the fundamentals of the interactions of materials with electric and thermal fields. The following presents a progression of such instances relevant to the spark plasma sintering process.

9.1 Atomic mobility and reactivity

The motion of atoms is of critical importance in the mass transport and resulting densification during any sintering process. The presence of a direct current field enhances the interdiffusion and reactivity between two species resulting in increased product formation and decreased incubation time as observed in diffusion couples in both oxide and metallic systems such as Al_2O_3-CaO, Al_2O_3-MgO, Cao-SiO_2 and Al-Au respectively. This is accompanied with a shift, Δ, in the concentration profile of the different diffusing species usually in the direction down the field, that can be expressed as

$$\Delta = \mu_{\text{eff}} E t \tag{I.12}$$

where μ_{eff} is the effective electrical mobility of the diffusing species in the direction of the field, E is the strength of the electric field and t is the time. Such enhancement of reactivity was found to be independent of the polarity of the field which is comprehensible as the rate of formation of intermetallics in the systems as above are limited by the compulsion of maintaining its stoichiometry and structure rather than being determined merely by the kinetics of diffusion. Indeed, in cases where the formation of intermetallics do not occur as in an isomorphous Cu-Ni-Cu diffusion couple, the diffusion profiles vary depending on whether one of the ends of the couple (e.g. Cu) is connected to the positive or negative pole of the field. However, in such instances the activation energy of diffusion as calculated from the resulting concentration profiles were found to be unchanged showing that the field keeps the underlying mechanism of diffusion unchanged.

9.2 Grain boundary mobility

Akin to motion in a crystal, atomic migration across and along grain boundaries plays a major role in sintering and is affected by electrostatic modifications at the grain boundary. For example, in solids containing migrating ionic species, the difference in energy of formation of anion and cation defects leads to the formation of a space charge layer close to the grain boundary resulting in the development of an electrostatic potential in these regions. An external electric field interacts with this layer to alter the activation energy for

migration of the above species across the grain boundaries according to

$$\Delta G_{\mathrm{m}} = \Delta G_{\mathrm{c}} + z_{\mathrm{i}} e s \left[\frac{U_{\mathrm{B}}}{2 l_{\mathrm{d}}}\right] \tag{I.13}$$

where $\Delta \mathrm{G_m}$ is the modification of the activation energy of the migrating species, $\Delta \mathrm{G_c}$ is the modification in the driving force due to difference of curvature of grain, $\mathrm{z_i}$ is the charge of the migration species, e is the elementary charge, s the distance of jump, $\mathrm{U_B}$ the applied bias voltage and $\mathrm{l_D}$ is the width of the space charge layer referred to as the Debye length. As a consequence, it was observed that a double layer of alumina with very small grain size of 4 µm in one layer and much larger 170 µm in the other when annealed in the presence of an electric field of strength $200\,\mathrm{V\,cm^{-1}}$, wherein the side with the smaller grains was positively biased, exhibited markedly higher grain boundary mobility and hence displacement in the smaller grain side.

9.3 Electromigration

The transfer of mass by the migration of metal ions due to an exchange of momentum with conducting electrons in presence of high current densities resulting in formation of voids in integrated circuits is a well-known obstacle in the electronics industry. During spark plasma sintering it affects the reactivity and densification of powders and is becoming increasingly relevant as the dimensions of the starting materials and structures of final products escalate towards the nano-regime. Atomic motion in pure metals, usually controlled by vacancy mediated diffusion, is modified in situations as stated above with the flux of atoms

being governed as per

$$J_a^E = \frac{D_{\mathrm{a}} c}{kT}(Z_{el}^* + Z_{wd}^*)e\Omega j \tag{I.14}$$

where J^*_{el} is the flux of atoms, D_a is the diffusivity of the atomic species, c is the concentration of vacancies, k is the Boltzmann constant, Z^*_{el} is the nominal valence of metal atom that accounts for the direct electric force on it, Z^*_{wd} is the nominal valence of metal atom that applies to the momentum exchange between the ions and other carriers, e the elementary charge, Ω is the resistivity and j the current density. The effect of current densities during electromigration in metallic systems was clearly observed in Al-Au diffusion couples.

Apart from the obvious influence of temperature, electromigration is also strongly dependent on the microstructure of the material. In the absence of defects like pores, inclusions, dislocations and grain boundaries, electromigration is associated with the accrual of material at one electrode and depletion at the other with the amounts usually being equal to each other. However, as with the majority of processed compacts, the existence of grain boundaries alone with conductivities different from that of the bulk leads to a non-zero overall flux of atoms. With the aforementioned amplification of processing nanostructured materials by spark plasma sintering, this effect becomes increasingly pronounced with decreasing grain sizes.

9.4 Heating rate

As mentioned earlier, heating rates as high as $1000\,^{\circ}\mathrm{C\,min^{-1}}$ can be employed in spark plasma sintering cycles. In order to completely appreciate the effects of such high heating rates it should be noted that a typical sintering cycle progresses through a sequence of various mass transport mechanisms some of which involve surface transport without any densification while others involve bulk transport leading to densification. Such a sequence usually begins with mechanisms with lower activation energies like surface diffusion and ends with those with higher ones like volume diffusion. High heating rates bring about two-fold benefits in sintering cycles. Firstly, the amount of time involved in the initial non-densifying process like surface diffusion is drastically reduced. This allows for sintering cycles to be completed much faster typically within minutes. Secondly from a thermodynamic point of view, the above incomplete surface diffusion averts a reduction of driving force for mass transport otherwise brought about by pore rounding and associated reduction of surface area. This 'preserved' driving force enhances following densifying mass transport mechanisms resulting in faster sintering. This is exhibited by a drastic rate of reduction of porosity in aluminum powders with increasing heating rates although the aforesaid rounding of pores is affected to a lesser extent as the initial grain size reduces. Higher heating rates also alter the temperature at which certain reactions or phase transformations take place as per the Kissinger effect

$$ln\left[\frac{Ac}{T^2}\right] = B - \frac{\Delta H_{\mathrm{rxn}}}{k_{\mathrm{B}}T} \tag{I.15}$$

where A and B are material constants, c is the heating rate, T is the temperature, ΔH_{rxn} is the enthalpy of the reaction and k_B is the Boltzmann constant.

10 Pressure

The role of externally applied pressure in sintering can be broadly divided into two categories. The first one involves mechanical effects like particle rearrangement and destruction of agglomerates while the second is related to chemical effects like modification of driving force and chemical potential at the surface of particles. In presence of stress the chemical potential at the interface between particles is

$$\mu = \dot{\mu} - \sigma_n \Omega \tag{I.16}$$

where μ is the modified chemical potential at the interface between particles, $\dot{\mu}$ is the standard chemical potential, σ_n is the normal stress at the interface and Ω is the atomic volume of the diffusing species. As per convention, a compressive stress is deemed to have negative values in the above equation. Thus it can be seen that during typical spark plasma sintering the application of an external uniaxial compressive pressure on the starting powder material leads to an increase in the driving force resulting in a decrease in the temperature necessary for sintering.

Delving deeper into the microscopic regime of the powder compact, the state of stress at the interface between particles can be resolved into hydrostatic and deviatoric components. The hydrostatic component acts to alter the surface energy and hence the stress associated

with the curvature of the surface of the pores given by

$$\frac{dV_{\mathrm{s}}}{dt} = (1 - V_{\mathrm{s}})B\left(g\frac{\gamma_{\mathrm{sv}}}{d_{\mathrm{p}}} + P_{\mathrm{E}}\right) \tag{I.17}$$

where V_s is the fraction of bulk material and (1 - V_s) is the fraction of the pores, B is the factor that accounts for the diffusion of the species, γ_{sv} is the surface energy of the particle, d_p is the diameter of the pore, g is a factor that is related to the geometry of the pore and P_E is the effective pressure. The deviatoric component, on the other hand, mainly provides shear stresses that aid sintering by one or more of particle rearrangement, disintegration of agglomerates, cleansing of surface by elimination of oxides and impurities and plastic flow of material in the closing stages. The above mechanisms working together result in an overall increase in the number of contacts developed adjacent to a powder particle, known as the coordination number given by e deviatoric component, on the other hand, mainly provides shear stresses that aid sintering by one or more of particle rearrangement, disintegration of agglomerates, cleansing of surface by elimination of oxides and impurities and plastic flow of material in the closing stages. The above mechanisms working together result in an overall increase in the number of contacts developed adjacent to a powder particle, known as the coordination number given by

$$N_{\mathrm{c}} = 14 - 10.4(1 - V_{\mathrm{s}})^{0.38} \tag{I.18}$$

where N_c is the coordination number and V_s is the fraction of bulk material.

It is relevant to add that the electric field also influences the mechanical behavior of

the powder during sintering. Strain rates in creep processes may be increased or decreased when the homologous temperature is above about $0.5T_m$ where T_m is the melting point of the powder material especially during the final stages of the sintering cycle. The modulus is also changed by field according to

$$E = \frac{Z^* e\phi}{\alpha i_d s} \tag{I.19}$$

where E is the elastic modulus, Z^* is the effective valence parameter of the diffusing species, e is the elementary charge, ϕ is the strength of the applied electric field, α is a proportionality constant, i_d is the current density and s is the area over which the force acts. Much is unknown about the effect of the electric field on dislocations. However, it can be said that in materials where dislocations are not associated with any charge, as in metals, the field with usual densities below 10^5 A cm^{-2} are not expected to affect their behavior. But in cases where the dislocations are coupled with a charge, as in halides, the field can exert a force on them depending on their orientation given by

$$\tau.\hat{b} = q.Ecos\theta \tag{I.20}$$

where τ is the applied stress, $\hat{b}$ is the Burgers vector, q is the charge per unit length of dislocation, E is the strength of the applied electric field and θ is the angle between the field and the Burgers vector.

11 Spark and plasma

The occurrence of spark discharge and existence of plasma is possibly the most debated issue relevant to the spark plasma sintering process and remains unresolved to this date. Almost all of the early reports on spark plasma sintering attributed the enhancement of densification to the existence of sparks in the contacts between powder particles. Such sparks were also thought to bring about local formation of plasma. It was believed that such discharges aid in sintering by ionization of material that results in an increase in mass transport, cleaning of surface of particles by sputtering and ablation of oxides. High temperatures developed at the interface between adjacent particles during spark discharge was considered to result in local melting and even evaporation. However, such roles played by discharge was only considered responsible without any direct proof of their existence.

Recently, the investigation about the presence of spark discharge has taken off from a much more fundamental point of view. It has been observed that local sparking occurred at the interparticle contacts especially during the advent of sintering. But neck growth ensued at such contacts irrespective of the occurrence of sparks thereby providing no apparent convenience over their absence. It has been argued that the occurrence of discharges could be safely set aside for non-conducting samples. Similarly several authors have argued both in favor of and against the absence of spark and plasma during spark plasma sintering cycles. The reports rely chiefly on observation of the experimental set up and/or neck region in the sintered compacts.

Deeper insights have been obtained as to the conditions prevalent during typical spark

plasma sintering cycles are conducive for the formations and stability of discharges. Among three distinct forms of vacuum discharges namely arc, spark and glow the latter two can be generated and sustained only in presence of very strong electric fields about hundreds or thousands of volts in magnitude. These can be safely negated since, as mentioned before, the electrodes in spark plasma sintering maintain a maximum of 10 V across them. Stable arcs, on the other hand, may theoretically be feasible in metallic materials or in dielectric ones where sufficient polarization can take place. At the same time, it is worth noting that the Debye length or the critical distance for production of discharge is about 10 µm in vacuum, much larger than that between two adjacent particles in a green body use in spark plasma sintering cycles. Additionally, whether the density of charge carriers like ions and free electrons is high enough to maintain continuous discharges is also a reasonable query that still needs to be resolved in this regard.

12 Oxidation

Progress of human civilization has been inextricably associated with the discovery of novel materials that exhibit exceptional properties. One of the recent examples of such a class of materials is metallic glasses [35, 36, 37]. These are solid metallic alloys that exhibit an atomic structure that is fundamentally different from polycrystalline materials [38, 39]. Metallic glasses possess a homogeneous disordered atomic structure that is devoid of conventional crystalline defects such as dislocations and grain boundaries [40, 41]. As a result of this defect-free, disordered atomic structure, metallic glasses manifest mechanical [42, 43], tribological [44, 45] and magnetic properties [46, 47] that are superior to those of their poly-

crystalline counterparts. Among them, iron-based metallic glasses are particularly attractive [48, 49], being comparatively inexpensive in materials costs as compared to palladium and zirconium-based ones. For example, $Fe_{48}Cr_{15}Mo_{14}Y_2C_{15}B_6$ metallic glass exhibits exceptionally high elastic modulus of 200 GPa and compressive fracture strength of 3200 MPa. The hardness of this metallic glass is also high, being about 13 GPa [50, 51, 52, 53]. Metallic glasses in the Fe-Si-B alloy system also possess excellent soft magnetic properties such as high permeability and low core loss. The saturation induction and maximum dc permeability of *Metglas*$^{\mathrm{R}}$ 2605SA1 are 1.56 T and 600 kN A^{-2} respectively [54, 55, 56]. These outstanding properties of metallic glasses harbor the potential to be utilized in a wide spectrum of applications spanning hard dies and tools, wear resistant cutting materials and transformer cores thereby ushering rapid technological and industrial advancement.

12.1 Stability

In order that an extensive commercial utilization of metallic glasses be viable, it is critical to evaluate these materials for their environmental stability at elevated temperatures [57]. It is imperative that metallic glasses exhibit adequate resistance against detrimental oxygen environments to be able to execute satisfactory performance [58]. For example, it is necessary to anneal metallic glass ribbons under a magnetic field to reduce stress and attain the requisite domain structure [59]. In most industrial manufacturing processes an ideal vacuum annealing environment is seldom achievable [60]. The result is an occurrence of oxidation on the surface of metallic glasses that introduces magnetic anisotropy and pinning centers that severely deteriorates soft magnetic properties [60]. This phenomenon of oxida-

tion in metallic glasses is fundamentally different than that in polycrystalline materials and is expected to be more uniform due to the absence of grain boundaries [57]. Additionally, it has been observed that the composition of oxide films naturally formed in air on metallic glasses exerts strong influence on their passivity and corrosion behavior [61, 62]. From a different perspective, thermally induced oxidation is a major chemical approach to synthesize oxide thin films for applications such as sensors, catalysts, insulators and bioimplants [63]. Oxidation of metallic glasses have also been reported to yield a ten times improvement in the wear resistance of these materials [64, 65, 66]. This could be utilized by metallic glass alloys and coatings fabricated by a number of processing techniques such as laser cladding and spark plasma sintering [67, 68, 69]. Thus, the successful manufacturing and applications of metallic glasses mandates a fundamental understanding of their behavior in oxygen-containing atmospheres during thermally activated processes.

The utilization of metallic glass alloy systems during manufacturing as well as applications is most extensive in the temperature regime of the supercooled liquid region (SLR) or, in other words, between the glass transition temperature T_g and the onset crystallization temperature T_x [70]. This temperature regime enables harnessing the drastic decrease in viscosity of metallic glasses [71]. Indeed these materials have been observed to exhibit viscosities varying from $1 \times 10^{12}\,\mathrm{Pa\,s}$ at T_g to $1 \times 10^{5}\,\mathrm{Pa\,s}$ at T_x [72]. Superplastic forming of metallic glasses can thus be achieved to fabricate complex near net components [73]. Additionally, this temperature regime, which is an evidence of the remarkable stability of the metallic glass against crystallization, restricts devitrification and permits preservation of the

amorphous structure of the material and hence its superior properties discussed earlier [74]. Thus investigation of the response of metallic glasses to oxidation in the supercooled liquid region without devitrification of its structure is of paramount importance.

12.2 Material selection

An accurate investigation of the oxidation behavior of metallic glasses in the supercooled liquid region warrants the selection of materials and employment of characterization techniques that enable precise and reliable identification of chemistry and quantification of the volume of oxide species evolved. It is established that oxidation is a slow, diffusion based phenomenon that occurs on the surface of materials. Reported examinations of oxidation are mostly limited to bulk and ribbon forms of metallic glasses [75, 76, 77]. The relatively lower specific surface area of these materials result in the evolution of a minute volumes of oxides [78]. Consequently, reliable quantification of oxidation is significantly impeded. It is thus commonplace to observe that such quantification is generally performed by indirect means such as estimation of weight [79]. This impediment is especially severe during the initial stages of oxidation, which, in fact, provide deeper insight into the reaction and hence arouses further intrigue. Conventional characterization techniques too induce drawbacks in analyzing the oxidation behavior of these materials. Scanning electron microscopy (SEM), for example, can resolve the morphology of films evolved only over a prolonged duration of oxidation [78]. Laboratory scale desktop X-ray diffraction (XRD) instruments while capable of determining the structure of oxides, the intensity of scattering is not representative of the minute volume of oxides formed [57].

12.3 *In-situ* characterization

Circumvention of these problems validates both the utilization of metallic glass in powder form that exhibits higher specific surface area as well as characterization techniques that can directly enumerate the evolution of oxides, particularly at the initial stages. In this regard, synchrotron-based *in-situ* X-ray scattering techniques are particularly attractive [80, 81]. For example, ultra-small angle X-ray scattering (USAXS) is a powerful technique that enables the acquisition of a high intensity of scattering [82, 83] even from a minute volume of structural features in metallic glasses [84]. Recent development of experimental environments have equipped the scientific community to acquire USAXS intensities *in-situ* during thermally-activated phenomena [85]. The USAXS intensity, I(Q) can be acquired over a broad range of the scattering vector, Q [86]. The dimensions of the scattering features are directly correlated to the scattering vector as $2\pi/Q$ [87]. Thus the distribution of USAXS intensity, I(Q) over the scattering vector, Q enables analysis of hierarchical structural features across a wide span of length scales from hundreds of micrometres to a few nanometres. The nature of the USAXS intensity distribution as a function of the scattering vector is also characteristic of the morphology of the scattering features due to the unique form factor each generates. For example, each of spheres, disks and cylinders of the same material will generate characteristic form factors and hence intensity distributions that can be utilized to distinguish between features of different morphologies [88]. The measured intensity distributions can be further fitted by small angle scattering analysis software tools based upon physical models that replicate the evolution of reactions [89, 90]. This in turn can be utilized

to yield quantitative information on the evolution of the scattering features. In summary, while *ex-situ* characterization techniques are suitable for the identification of chemistry and structure of oxides, *in-situ* techniques can enable quantification of time dependent evolution. These strongly complement each other and, utilized in conjunction, provide an excellent procedure of accurately establishing the oxidation behavior of metallic glass powder throughout the initial stages towards conclusion.

13 Crystallization

The critical importance of kinetics in the development and processing of metallic glasses has been established since their inception. For example, the success in the synthesis of the first metallic glass, Au-Si in 1960 was achieved largely due to rapid quenching techniques capable of cooling metallic alloy melts at a very high rate of about 10^6 $\mathrm{K\,s^{-1}}$ [12]. It clearly demonstrated that the formation of thermodynamically stable crystalline phases by nucleation and growth can be completely avoided by tailored kinetics to process metastable amorphous alloys, for example, in Pd-based alloy systems such as Pd-Cu-Si and Pd-Ag-Si [13]. Fundamental investigations on these Pd-based metallic glasses laid the foundations of understanding thermal transformations such as glass transition and crystallization in these materials. This scientific knowledge together with the development of the novel melt spinning processing technique enabled thin amorphous $Fe_{40}Ni_{40}B_{20}$ ribbons known as *MetGlas*$^{\mathrm{R}}$ [91] to be manufactured on an industrial scale for commercial applications in low core loss transformers [55].

13.1 Processing limitation

While the properties of metallic glasses render them commercially attractive, their structure presents a critical processing limitation. The metallic bonding in these materials, being isotropic in nature, mandates extremely high cooling rates for complete amorphization as noted earlier [92]. It is thus necessary to have at least one dimension of the quenched glass extremely small so as to enable rapid extraction of heat across that direction [93]. This restricted the production of metallic glasses to forms such as ribbons, wires and powder where the respective thickness and diameters would be of the order of a few micrometers.

Subsequent research was primarily directed towards scaling up the dimensions of these materials by increasing their glass forming ability (GFA). It was established that a large mismatch in the sizes of atoms [94] and negative heat of mixing between the constituent elements were primary criteria for a highly dense random packing [95]. This is commonly known as the 'confusion effect' [96] wherein upon rapid quenching the atoms of the large number of constituent elements cannot arrange themselves in an ordered lattice due to reduced diffusivity at low temperatures. The required critical cooling rates for this group of materials are significantly lower, about $1\,\mathrm{K\,s^{-1}}$, which can be realized by comparatively simpler casting techniques. Consequently, depending upon the size of the mold, the dimensions of these alloys can reach up to several millimeters, thereby earning the designation 'bulk metallic glasses'. One of the earliest precedents among this novel class of materials is $Zr_{41}Ti_{14}Cu_{12}Ni_{10}Be_{23}$, commercially known as *Vitreloy 1*^{R} [16]. It was eventually followed by numerous others in a wide range of alloy systems such as Pd-Cu-Ni-P , Pt-Co-Ni-Cu-P,

Ti-Ni-Cu-Sn, Ni-Zr-Cr-B and La-Al-Ni-Cu-Co [17, 18, 19, 20, 21].

13.2 Iron based metallic glasses

It can be immediately observed that the constituent elements in these bulk metallic glasses (BMGs) are extremely expensive. The attention thus naturally shifted to the development of comparatively cheaper Fe-based BMGs [22]. Following the first in this group, namely Fe-Al-Ga-P-C-B [23], a large number of alloy systems have been reported to form BMGs by a variety of processing techniques such as copper mold casting, suction casting and injection molding. These are mostly metal-metalloid alloy systems with the typical metallic elements such as Fe, Cr, Mo, Co and Ni constituting about 80% of the alloy composition while typical metalloid elements such as B and Si constitute the rest 20% [24, 26]. For example, one of the alloys of key importance in this group is $Fe_{50}Cr_{15}Mo_{14}C_{15}B_6$ that is often referred to as 'amorphous steel' and its high temperature thermoplastic formability has been investigated for potential structural applications. Considerable research is focused on modifying this alloy by addition of rare earth elements such as Dy, Er, Tm and Y [25, 24] for improving its properties. $Fe_{48}Cr_{15}Mo_{14}Y_2C_{15}B_6$, in particular, exhibits a high elastic modulus of 200 GPa, compressive fracture strength of 3200 MPa, and hardness of about 13 GPa [27, 52]. Its superior wear and corrosion resistance has also been utilized as amorphous coatings processed by a variety of techniques [28, 29]. However, since the amorphous alloy is inherently metastable, exposure to substantially high temperatures during these applications can induce structural transformations that may deteriorate its properties. Thus, in order to harness these attractive prospects, it is critical to understand the thermal behavior of this

$Fe_{48}Cr_{15}Mo_{14}Y_2C_{15}B_6$ metallic glass. Research carried out with this motivation has, however, been mostly limited to an investigation of the GFA and the largest diameter and section thickness of the alloy synthesized by various methods [24]. On the other hand, examination of crystallization has been restricted to experimental reports of characteristic temperatures at scattered heating rates [97, 98] which deter the establishment of the underlying mechanism of solid-state transitions in this alloy.

13.3 Non-conventional characterization

Reported analyses on crystallization in spark plasma sintered iron based bulk metallic glasses, however, suffer from drawbacks of the techniques employed. For example, calorimetric studies on *in-situ* composites [99] only provided limited information on the activation energy of the exothermic reactions that is largely dependent of the analytical model used [100, 101]. Crystal sizes estimated from x-ray diffraction alone, while an approximate indicator of the dimensions of the crystals are subject to the broadening of the instrument itself and that of the pure compound. Additionally it is unexpected that the evolution of crystals in sintered metallic glasses would exhibit a single size [102]. Hence estimates of the volume fraction of these crystals and results derived from rate kinetics are also debatable. It has been proven that the mechanical properties and thermal stability of these metallic glasses are dependent not only on the mean size of the crystals but also on their distribution and volume fraction [103].

In this regard, small angle neutron scattering (SANS) is a powerful technique for an accurate quantitative analysis of crystallization in spark plasma sintered iron based bulk

metallic glasses [104]. It enables the acquisition of a high intensity of scattering from crystals embedded within a bulk metallic glass matrix *in-situ* during annealing and hence the precise determination of the critical temperature of processing and safe service. This intensity can be acquired over a broad range of the scattering vector, Q and hence facilitate the study of the evolution of structure across a wide span of length scales [86], D from the direct relationship between them as $D = 2\pi/Q$ [87]. The small angle scattering analysis tool IRENA [90] complements this with the capability of calculating scattering contrast of any phase as a function of its composition and can be utilized to obtain an accurate estimate of the distribution of size and volume of each crystal. SANS equipped with supporting structural and microscopic techniques can thus be utilized to establish a cogent understanding of the crystallization in metallic glasses. This thesis thus aims to analyze the crystallization behavior in a spark plasma sintered iron based bulk metallic glass during annealing. Development of the microstructure during isothermal annealing is presented. The SANS intensity acquired during annealing is fitted with a size distribution tool to estimate the evolution of the diameter and volume of crystals. These results are utilized to establish the mechanism of crystallization in this material.

14 Motivation

The present thesis aims to establish a fundamental understanding of the multitude of thermal phenomena in $Fe_{48}Cr_{15}Mo_{14}Y_2C_{15}B_6$ metallic glass powder. Particular emphasis is laid upon thermally induced densification, oxidation and crystallization in this material.

The densification of the iron-based metallic glass powder during spark plasma sin-

tering is presented. The stages of densification are identified along with the temperature ranges at which they are prevalent. The mechanism of consolidation is investigated along with a theoretical analysis of the kinetics of mass flow. The effect of externally employed parameters such as heating rate and applied pressure on the modification of the kinetics if established to enable prediction of output properties of metallic glass compacts such as relative density and geometry.

The morphology and structure of oxides on this metallic glass powder is identified. The kinetics of isothermal oxidation are theoretically predicted and compared against experimentally measured ones.

The evolution of structure in iron-based metallic glass powder with temperature is investigated. The phases evolving as a result of isochronal thermal annealing are identified along with an estimation of their corresponding activation energy barrier. The mechanism of crystallization of each of the phases is established and is concluded with the effect of heating rate on the kinetics.

Chapter II

Experimental Procedure

1 Metallic glass powder

An iron-based metallic glass powder of nominal composition $Fe_{48}Cr_{15}Mo_{14}Y_2C_{15}B_6$ (at.%) was employed in this investigation. The powder consisted of particles of average diameter 40 µm and standard deviation of about 10 µm.

2 Spark plasma sintering

Spark plasma sintering (SPS) was performed in a commercial SPS unit (Thermal Technology, SPS 10-3). Graphite dies with internal diameter 15.2 mm and graphite punches of diameter 15 mm were utilized. To reduce friction and aid in the displacement of the punches within the graphite die, a thin graphite foil of thickness 0.1 mm was wrapped around the punches. Temperature was measured using a K-type thermocouple placed inside the wall of the die. The entire setup was placed in a chamber inside the SPS unit and sintering was performed in vacuum (1.33 Pa).

For analysis of viscous flow and heating rate the powder was first prepressed under a uniaxial compressive pressure of 25 MPa. It was then sintered from ambient temperature continuously up to 1000 °C at heating rates of 25, 50, 100 and 150 °C min^{-1} during which the pressure was maintained constant. For the study on pressure controlled deformation assisted sintering, the powder was first prepressed under different applied pressures of 20, 30, 50 and 70 MPa. This was followed by sintering from ambient temperature to 560 °C at a constant heating rate of 25 °C min^{-1} while the pressure was kept constant in each case.

Investigations on crystallization were performed in samples sintered at temperatures of 570, 600, 630, 650, 700, 750 and 800 °C attained at a heating rate of 100 °C min^{-1} along with simultaneous application of uniaxial compressive pressure up to 70 MPa.

Samples in the shape of discs, 15 mm in diameter and about 3 mm in thickness were obtained by these processing conditions.

3 Sample preparation

Surfaces of samples were polished first by silicon carbide papers of increasing grit from 300, 600, 1200, 2400 and 4000. This was followed by polishing with diamond suspension. For superior quality surface finish final polishing was performed with alumina (Al_2O_3) suspension.

4 Density measurement

During all sintering experiments, temperature, pressure and punch position were recorded with time. The punch position was utilized for calculating powder contraction

(reduction in thickness of powder compact), relative density, densification rate and shrinkage of the powder compact.

Density of sintered compacts was also measured according to Archimedes' principle. For samples with relative densities up to 98%, ASTM Standard Designation: B962-17 'Standard Test Methods for Density of Compacted or Sintered Powder Metallurgy (PM) Products Using Archimedes' Principle [105] was followed. For samples with relative density less than 2%, ASTM Standard Designation: B311-17 'Standard Test Method for Density of Powder Metallurgy (PM) Materials Containing Less Than Two Percent Porosity' [106] was employed.

5 Scanning electron microscopy

Morphology of powder particles and sintered compacts were observed in two scanning electron microscopes. Overall low magnification images were acquired using a JEOL, JSM 6360 scanning electron microscope. High resolution scanning electron microscopy was conducted using a FEI, Quanta 600 scanning electron microscope equipped with a field emission gun (FEG).

6 Image analysis

Sizes of particles were measured using a public domain image processing software, ImageJ, available from the National Institute of Health (NIH), USA.

7 X-ray diffraction

Structural analysis of the pristine and annealed powder and sintered samples were carried out in an X-ray diffractometer (Philips Norelco) operating with Cu-Kα radiation (λ=1.541 78 Å) at 45 kV and 40 mA. The diffraction angle was varied from 30 °to 60 °at a step increment of 0.02 °with a count time of 1 s.

8 Hardness

Indentation hardness was measured in a Vicker's microhardness tester (Clark's Instruments, CM-700AT). The instrument was operated at a load of 2.94 N and a holding time of 10 s.

9 Differential scanning calorimetry

Thermal behavior of the powder was evaluated by a simultaneous thermal analyzer (TA Instruments, SDT Q600) under dry high purity argon gas atmosphere at a flow rate of 50 ml min^{-1}. About 100 mg of powder was heated in alumina crucibles, continuously from ambient temperature to 1273 K (1000 °C) at constant heating rates of 0.17, 0.33, 0.50 and 0.67 K s^{-1} (10, 20, 30 and 40 °C min^{-1}).

10 Transmission electron microscopy

Samples for transmission electron microscopy were prepared by a dual beam focused ion beam technique (FEI Nova 200 Nano Lab). High resolution images and selected area

diffraction patterns were acquired in a transmission electron microscope (FEI Technai F20) operated at 200 kV.

11 Isothermal oxidation

Ex-situ isothermal oxidation of the metallic glass powder was carried out in a muffle furnace (Thermo Fisher Scientific, FB1315M) in freely flowing dry air at atmospheric pressure at 580 °C and 650 °C. For each experiment, the furnace was first preheated to the desired temperature. After the temperature stabilized, about 3 g of the powder was placed in an alumina crucible and introduced inside the furnace. Isothermal time dependent experiments were conducted at the lower temperature, 580 °C for 120, 240, 360, 480, 600 and 720 min and at the higher temperature, 650 °C for 60, 120, 180, 240 and 300 min respectively. Temperature was controlled within ± 0.3 °C during all the experiments.

12 Single-particle Raman spectroscopy

Chemical identification of the oxides was conducted by Raman spectroscopy. Spectra were acquired by a micro-Raman spectrometer (WITec, alpha300 R) equipped with a grating of 600 lines mm^{-1}. A laser wavelength of 532 nm was utilized to excite the spectra with an incident laser power of 3 mW. The laser spot size on the samples was 10 µm in diameter. The signal was accumulated for 200 s by employing a 20X objective lens.

13 Ultra-small angle X-ray scattering

In-situ ultra-small angle X-ray scattering experiments were performed during isothermal oxidation of the metallic glass powder. For each experiment, a sample 'sandwich' was prepared using mica sheets and the metallic glass powder as described here. First, a circular sheet of mica with thickness 25 µm and diameter 6 mm was laid out horizontally. Another annular sheet of mica of the same thickness with external diameter of 6 mm and internal aperture of 3 mm was placed on top of and concentric to the first sheet. A thin layer of the metallic glass powder was spread uniformly within the internal aperture of the annular mica sheet. Thus, the annular sheet behaved as a 'washer', thereby securing the powder sample in place. A third sheet of mica, identical to the first one, was placed on top, covering the powder and the annular sheet. A thin sample with the metallic glass powder sandwiched between mica sheets was thus assembled. In this configuration air flowed freely at atmospheric pressure. This assembly was introduced within the sample cell of a temperature controlled stage (Linkam Scientific, TS1500) with a temperature stability of 1 °C. The temperature of the sample cell in the stage was increased from ambient to the desired values of 580 °C and 650 °C at a heating rate of 50 °C min^{-1}. Isothermal time dependent experiments were conducted at the lower temperature, 580 °C for 720 min and at the higher temperature, 650 °C for 300 min.

X-ray scattering intensities were measured as a function of the scattering vector in the range of 0.0005 to 0.2 Å^{-1}, *in-situ* during isothermal oxidation, by the Ultra-Small Angle X-ray Scattering instrument at beamline 9-ID of the Advanced Photon Source, Argonne

National Laboratory [82, 107, 83]. The instrument was operated with an X-ray wavelength of 0.59 Å that corresponds to an X-ray energy of 21 keV, beam size of 0.8 mm × 0.8 mm and X-ray photon flux of approximately $10^{13}\,\mathrm{mm^{-2}\,s^{-1}}$. The exposure time for each measurement was 1 min and the duration between two consecutive measurements was approximately 3 min. Background scattering from the environment, instrument and temperature controlled stage was subtracted from the measured intensities by the USAXS data reduction package, INDRA. The small angle scattering data analysis tool suite IRENA was utilized for modeling the reduced scattering intensities. X-ray scattering length densities and the corresponding X-ray scattering contrasts of the materials were calculated based on their compositions by the scattering contrast calculator support tool, also available in IRENA [90].

14 Thermogravimetric analysis

The gain in mass was measured *in-situ* during isothermal oxidation of the metallic glass powder at 580 °C and 650 °C by a simultaneous thermal analyzer (TA Instruments, SDT Q600). About 100 mg of the powder was placed in an alumina crucible and the temperature of the sample was increased from ambient to the desired values of 580 °C and 650 °C at a heating rate of $50\,^{\circ}\mathrm{C\,min^{-1}}$. The gain in mass was measured continuously during isothermal time dependent experiments at the lower temperature, 580 °C for 720 min and at the higher temperature, 650 °C for 300 min.

15 Extended Q-range Small Angle Neutron Scattering

In-situ neutron scattering experiments were performed during isochronal and isothermal annealing of the sintered samples. For isochronal annealing, the sintered samples were heated from ambient temperature up to 800 °C while for isothermal ones, they were heated up to 700 °C and 725 °C and held at the respective temperatures for 100 min each. Neutron scattering intensities were measured as a function of the scattering vector in the range of 0.01 to 0.4 $Å^{-1}$, *in-situ* during annealing, by the General-Purpose Small-Angle Neutron Scattering Diffractometer at beamline CG-2 of the High Flux Isotope Reactor, Oak Ridge National Laboratory [108, 109]. The measured intensities were corrected for background from the sample holder, sample thickness and transmission. These data were modelled and analyzed by the size distribution tool available in IRENA software [90]. Neutron scattering length densities and the corresponding neutron scattering contrasts of the materials were calculated based on their compositions by the scattering contrast calculator support tool, also available in IRENA.

Chapter III

Sintering Mechanism

1 Introduction

This chapter focuses on the sintering mechanisms in iron-based metallic glass powder. The densification kinetics during isochronal sintering are analyzed to establish the kinetics and activation energy of viscous flow. The effect of heating rate and pressure on the densification kinetics are also presented.

2 Powder morphology

The representative morphology of the Fe-based metallic glass powder is presented in Fig. **??**. The powder is observed to consist of particles, mostly spherical, of various sizes.

The contents of this chapter are reproduced, with permission, from

1. T. Paul *et al.*, Journal of Alloys and Compounds 738 (2018) 10 - 15
2. T. Paul *et al.*, Journal of Physics D: Applied Physics 50 (2017) 1 - 4
3. T. Paul *et al.*, Scripta Materialia 126 (2017) 37 - 40
4. T. Paul *et al.*, Journal of Applied Physics 120 (2016) 134901
5. A. Singh *et al.*, JOM 68 (2016) 1932 - 1937

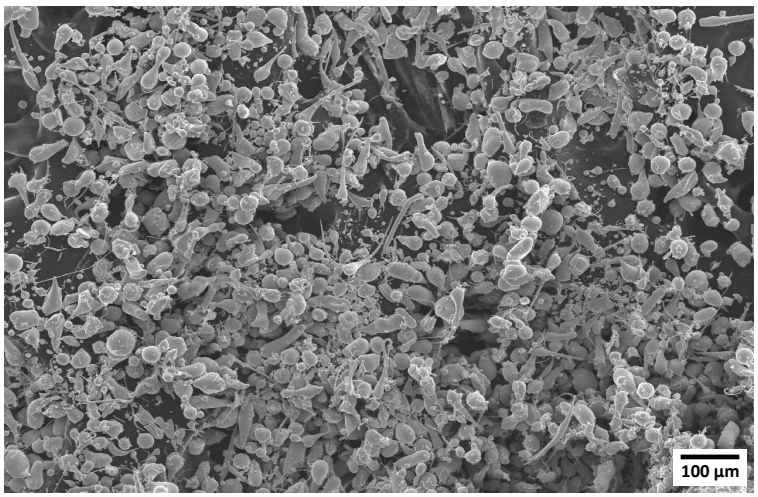

Figure 1: Morphology of $Fe_{48}Cr_{15}Mo_{14}Y_2C_{15}B_6$ metallic glass powder

In order to obtain a quantitative estimate, the sizes of the particles were measured. The sizes were observed to be normally distributed, as shown in Fig. 2a. The relative fraction of the number of particles with sizes within a specific range is plotted in Fig. 2b. More than 95% of the particles can be observed to have sizes ranging from 20 to 60 µm. The mean and standard deviation of the sizes, estimated from an analysis of this normal distribution were about 40 µm and 10 µm respectively.

During the sintering of powder with such a wide range of particle sizes, a continuous network is formed by the relatively larger particles. The smaller particles, on the other hand, saturate the intermediate voids within this network [110]. This can be observed in Fig. 3, a scanning electron microscope (SEM) image of the fractured surface of a sample sintered at 600 °C. Such a distribution of powder particles of various sizes have been observed to result in efficient packing with the closure of a large fraction of pores [111].

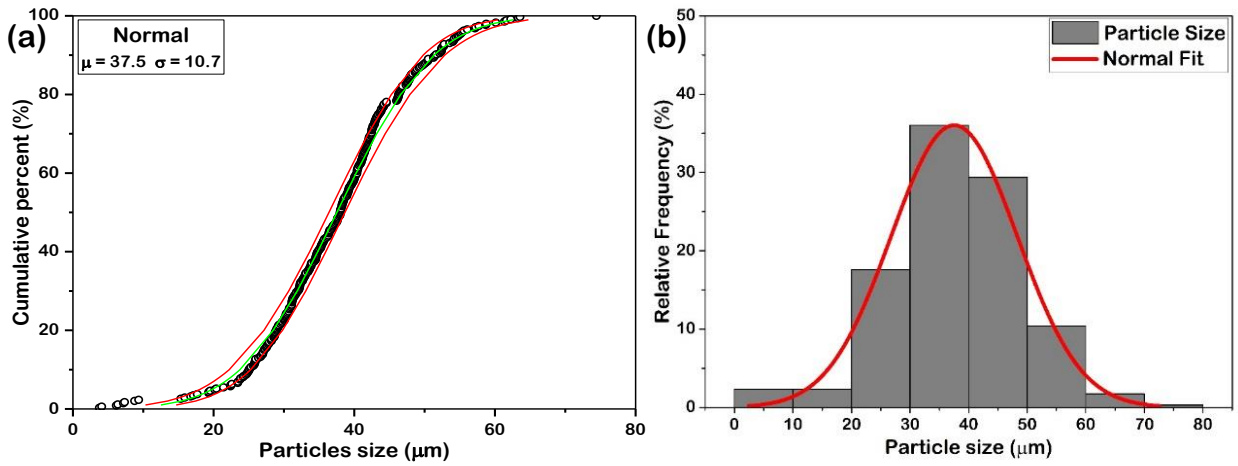

Figure 2: (a) Normal distribution of sizes of $Fe_{48}Cr_{15}Mo_{14}Y_2C_{15}B_6$ metallic glass powder particles (b) Relative fraction of powder particles within specific size ranges

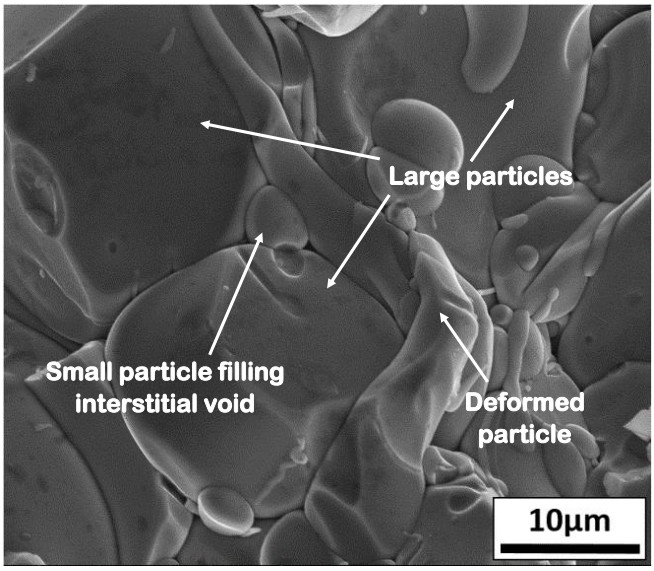

Figure 3: Representative fracture surface of $Fe_{48}Cr_{15}Mo_{14}Y_2C_{15}B_6$ metallic glass powder SP sintered at 600 °C. The larger particles form a continuous network while the smaller ones saturate intermediate voids

3 Densification behavior

The x-ray diffraction (XRD) spectrum of the pristine $Fe_{48}Cr_{15}Mo_{14}Y_2C_{15}B_6$ metallic glass powder is presented in Fig. 4a. It exhibits a diffused peak, characteristic of fully

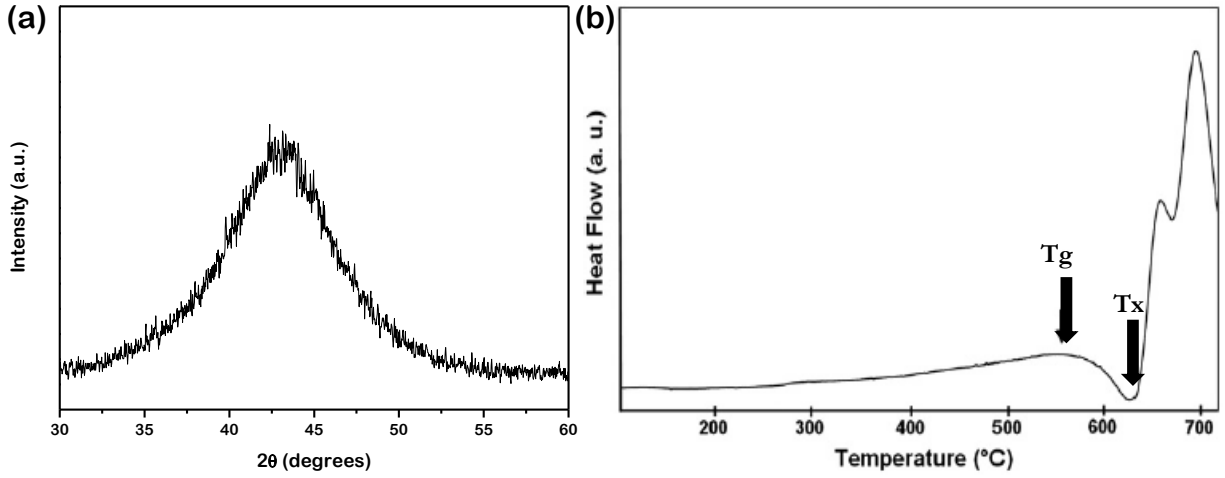

Figure 4: (a) X-ray diffraction spectrum of pristine $Fe_{48}Cr_{15}Mo_{14}Y_2C_{15}B_6$ metallic glass powder confirms the amorphous nature of the material and (b) Differential scanning calorimetric trace at $20\,\mathrm{K\,min^{-1}}$ exhibits a glass transition temperature of 575 °C and a crystallization onset temperature of 653 °C

amorphous materials. No sharp peaks, indicative of crystalline phases, can be observed in the spectrum. Thus it can be concluded that the pristine metallic glass powder is fully amorphous. The differential scanning calorimetry (DSC) curve of the powder, presented in Fig. 4b [112], confirms the amorphous nature, exhibiting a clear glass transition temperature, T_g of about 575 °C and an onset crystallization temperature, T_o of about 653 °C.

The relative density of the samples sintered at various temperatures is presented in Fig. 5. Highly dense samples with relative density greater than 90% could be processed at the investigated sintering temperatures ranging from 570 to 800 °C. In particular, the relative density achieved in the sample sintered at 570 °C was about 92% which increased to about 98% upon sintering at 630 °C. Sintering at 800 °C resulted in fully dense samples. The SEM micrographs of the representative cross sections of the samples, presented in Fig. 6, also agree well with this densification behavior. Very small number of pores can be observed in the sample sintered at 570 °C (Fig. 6a), while the boundaries between adjacent particles can be

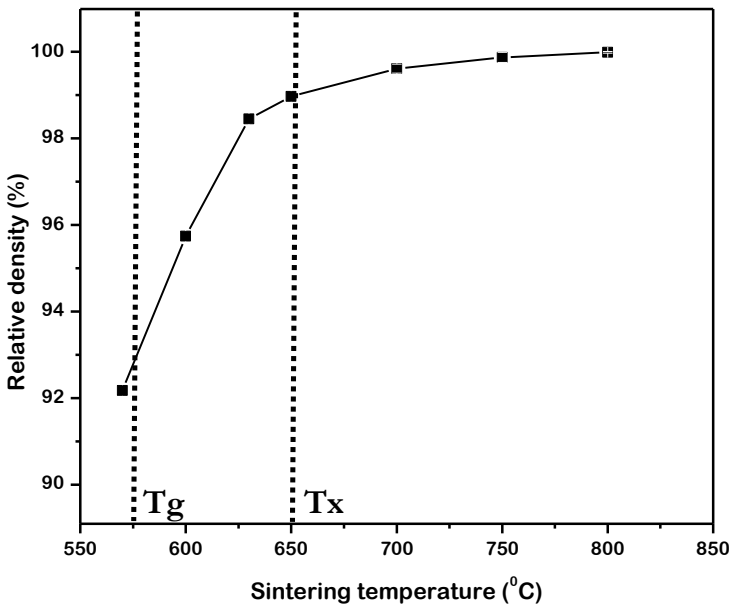

Figure 5: Relative density of $Fe_{48}Cr_{15}Mo_{14}Y_2C_{15}B_6$ metallic glass powder SP sintered at different temperatures. Large densification is observed in the supercooled liquid region while that at higher temperatures is lesser

distinguished. These pores and boundaries are almost completely eliminated in the sample sintered at 630 °C (Fig. 6b.) No pores or boundaries are visible in the SEM micrograph of the sample sintered at 800 °C (Fig. 6c). The increasing trend of relative density with sintering temperature is thus confirmed by the SEM micrographs of the cross sections of the sintered samples.

As observed in Fig. 5, during sintering in the supercooled liquid region (T_g - T_x represented by vertical broken lines), a large increment in relative density of 6.3% occurred with an increase in the sintering temperature from 570 to 630 °C. Further increments in relative density with an increase in sintering temperature were, in contrast, considerably lesser, about 1.5%. Thus it can be concluded that densification was greater up to 630 °C than above this temperature. In order to understand this behavior, XRD analysis was performed

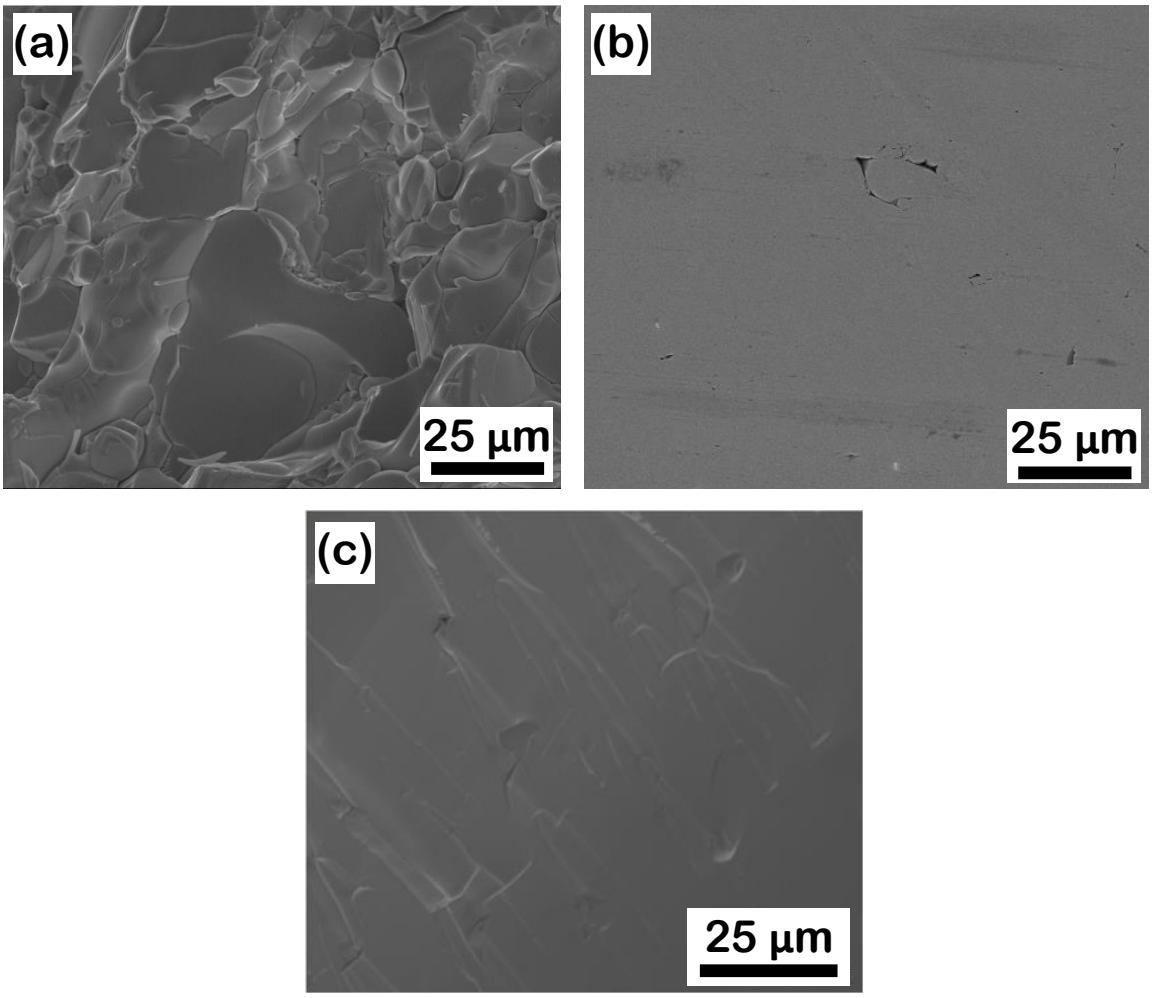

Figure 6: Cross sections of $Fe_{48}Cr_{15}Mo_{14}Y_2C_{15}B_6$ metallic glass powder SP sintered at (a) 575 °C, (b) 600 °C and (c) 800 °C. Pores and interparticle boundaries can be distinguished in (a) and (b) while these are completely eliminated in (c)

on the samples sintered at these temperatures. The resulting spectra are presented in Fig. 7 along with that of the pristine metallic glass powder for comparison.

It can be observed that a broad halo, characteristic of fully amorphous materials, can be observed in the diffraction angle 2θ range of 41 to 46° in the XRD spectrum of the powder. A similar halo is also exhibited by the XRD spectra of the samples sintered at 570 and 600 °C indicating that they were also fully amorphous. Mass flow in amorphous materials occur

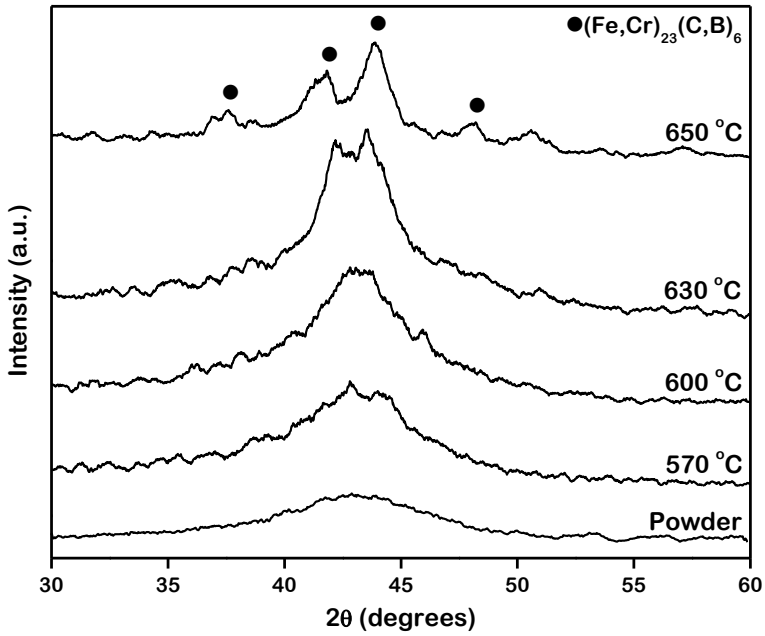

Figure 7: X-ray diffraction spectrum of $Fe_{48}Cr_{15}Mo_{14}Y_2C_{15}B_6$ metallic glass powder SP sintered at different temperatures. Sample is fully amorphous upon sintering at 575 °C and 600 °C

primarily by viscous flow. The extent of sintering can be determined by an estimation of the neck growth and pore closure according to [113]:

$$x^2 = \frac{3a\gamma}{2\eta}t \tag{III.1}$$

$$r_\mathrm{i} - r_\mathrm{f} = \frac{\gamma}{2\eta}t \tag{III.2}$$

where x is the radius of the neck of formed between two particles, r_i and r_f are the radii of the pore before and after sintering for time t, a is the radius of the particles, γ is the surface tension of the material and η is the viscosity of the material. The viscosity of $Fe_{48}Cr_{15}Mo_{14}Y_2C_{15}B_6$ metallic glass exhibits high values of the order of 10^{12} Pa s below the

T_g, 575 °C. In the SLR, however, it undergoes a reduction by almost two orders of magnitude as the temperature increases from T_g to T_x, 653 °C. This drastic reduction in viscosity led to the progress in densification due to increase in the extent of sintering according to Eqs. III.1 and III.2 resulting in large increments in density with increase in sintering temperature up to 630 °C as observed in Fig. 5.

4 Viscous flow

4.1 Shrinkage and densification rate

The role of viscous mass flow mechanism during sintering of $Fe_{48}Cr_{15}Mo_{14}Y_2C_{15}B_6$ metallic glass powder was analyzed by studying the densification behavior. The contraction of the powder compact with increasing temperature during SPS is presented in Fig. 8a. It can observed that the powder undergoes an initial contraction of about 1.2 mm followed by an additional contraction of about 0.2 mm before the curve flattens out at about 1000 °C. To study the densification behavior, the instantaneous relative density of the sample during SPS was estimated according to [1]:

$$\rho = \frac{L_o}{L}\rho_o \tag{III.3}$$

where ρ (%) is the instantaneous relative density at time t (s), L_o (3.60 mm) is the initial height of the compact, ρ_o (59.7%) is the initial relative density and L (mm) is the instantaneous height of the sample. The instantaneous relative density of the compact is plotted against temperature as depicted in Fig. 89b. It can be observed that the densification of

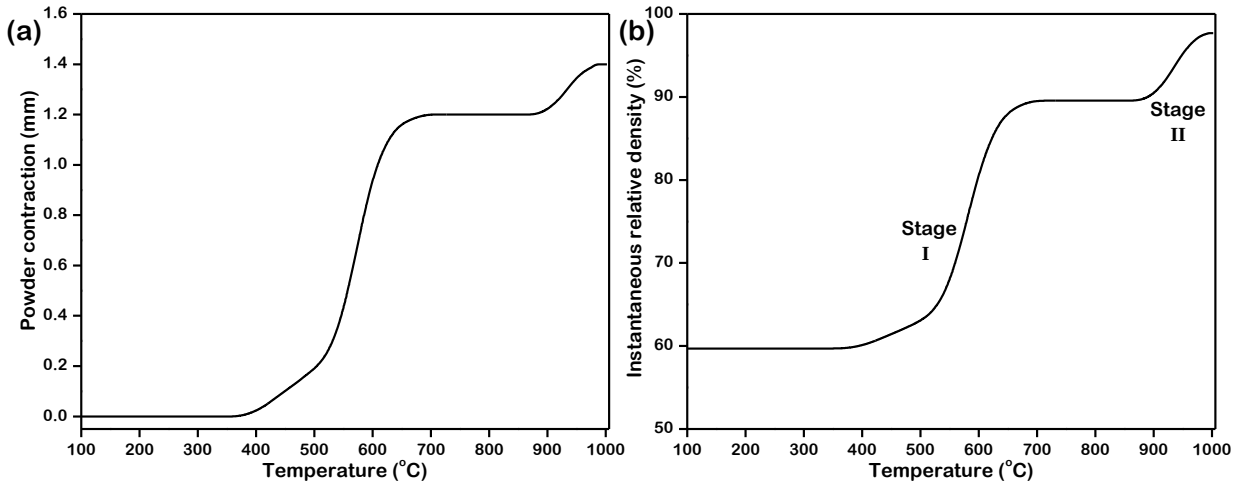

Figure 8: (a) Contraction of $Fe_{48}Cr_{15}Mo_{14}Y_2C_{15}B_6$ metallic glass powder compact during SP sintering up to 1000 °C. (b) Evolution of instantaneous relative density of the samples. Relative density increases from 60% to 90% in Stage I which ceases at 740 °C followed by Stage II where it reaches near full densification

the powder takes place in two clearly distinguishable stages. Stage I is noted to begin form a temperature of about 320 °C, as identified by the onset of densification. this is followed by an increase in the the instantaneous relative density with temperature. At about 740 °C, a cessation of the stage I densification is observed. The relative density increases from 60% to 90% in this range of temperature. Stage II is similarly identified to range from a temperature of about 830 °C to 1000 °C wherein the sample undergoes an additional increase in the relative density to finally reach near full densification.

The increase in the relative density at temperatures higher than 320 °C suggests the occurrence of bulk mass transport in this temperature regime. Further insight into the densification behavior of the $Fe_{48}Cr_{15}Mo_{14}Y_2C_{15}B_6$ metallic glass powder can be obtained upon estimation of the instantaneous densification rate according to [1]:

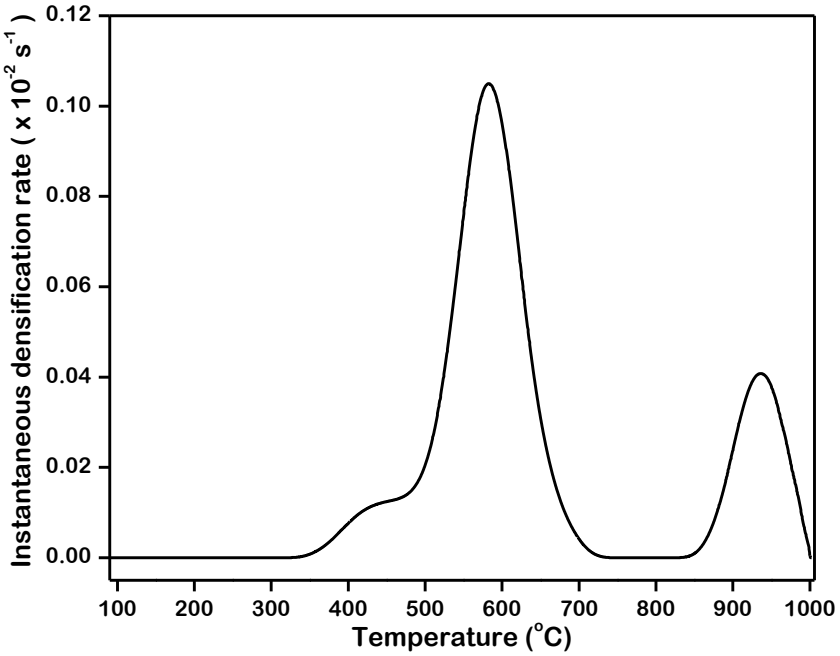

Figure 9: Instantaneous densification rate in $Fe_{48}Cr_{15}Mo_{14}Y_2C_{15}B_6$ metallic glass powder compact during SP sintering

$$\dot{\rho}_n = \frac{d\rho}{dt} = \frac{\rho_{n+1} - \rho_{n-1}}{t_{n+1} - t_{n-1}} \tag{III.4}$$

where $\dot{\rho}_n$ (s^{-1}) is the instantaneous densification rate at time t_n and ρ_{n+1} and ρ_{n-1} are the instantaneous relative densities at times t_{n+1} and t_{n-1}. Here. the time interval (t_{n+1} - t_{n-1}) is 2 s. The variation in the instantaneous densification rate is presented in Fig. 9. It confirms the ranges of temperature for the two stages of densification as observed in Fig. 8b. Additionally it can be seen that the densification during Stage I increases to a much higher rate as compared to that in Stage II.

The densification rate attains a maximum (peak rate) of almost $0.0011\,s^{-1}$ at a temperature of about 585 °C. The corresponding peak rate attained during Stage II at about 935 °C is much lower, about $0.0004\,s^{-1}$. The characteristics of the two stages of densification

Table 2: Characteristics of Stages I and II during SP sintering of $Fe_{48}Cr_{15}Mo_{14}Y_2C_{15}B_6$ metallic glass powder compacts

Stage	Start temperature (°C)	Peak temperature (°C)	Finish temperature (°C)	Peak densification rate (s^{-1})
I	320	585	740	0.0011
II	830	935	1000	0.0004

are summarized in Table 2.

In order to identify the nature of the samples in the two stages, they were separately sintered at various temperatures and analyzed by XRD. In particular, the XRD spectrum of the sample sintered at the temperature at which the maximum densification rate was attained in Stage I, namely, 585 °C, is presented in Fig. 10. The broad halo in the diffraction spectrum indicates that the sample is fully amorphous. This is comprehensible as this temperature is very close to the T_g of the material and hence it remains in its glassy state. In contrast to the above, the XRD spectrum of the sample sintered at 800 °C shows only sharp peaks corresponding to a partially crystalline sample. The phases identified in Fig. 10 are $(Fe,Cr)_{23}(C,B)_6$, Fe_7C_3 and Fe_3C. This temperature is much above the T_x of the material, and thus, samples sintered at this temperature are partially crystalline. Thus, Stage II represents the densification behavior of a partially crystalline compact.

4.2 Activation energy

The amorphohus nature of the sample sintered at 585 °C leads to the conclusion that during SPS in the entire temperature range from 320 °C to 585 °C in Stage I, the power

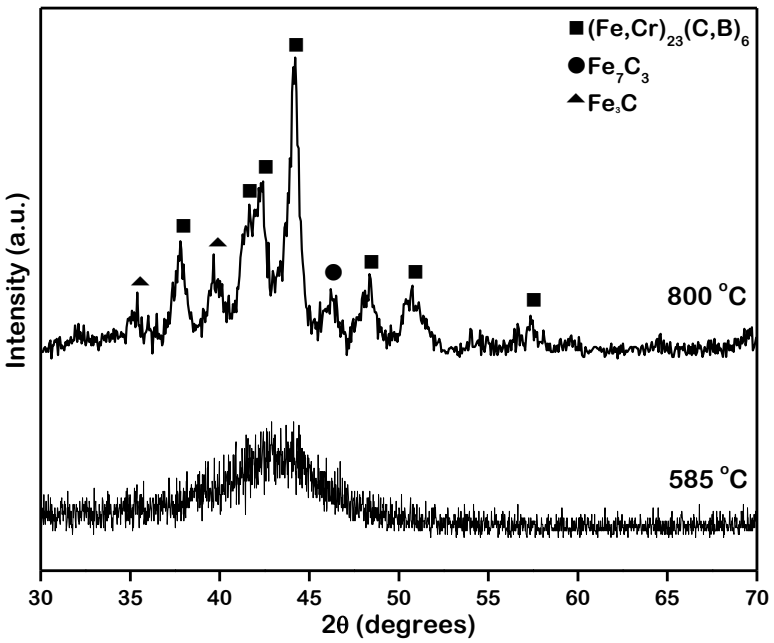

Figure 10: X-ray diffraction spectra of $Fe_{48}Cr_{15}Mo_{14}Y_2C_{15}B_6$ metallic glass powder compacts sintered at the peak temperature and before the onset of Stage II. At peak densification temperature the sample is fully amorphous while before Stage II it is partially crystalline

compact is fully amorphous. Sintering in amorphous materials proceeds by viscous flow [113, 114] where its contribution to the isothermal shrinkage of a compact of powder particles can be expressed as [115]:

$$\frac{\Delta L}{L_o} = \frac{3\gamma}{4D\eta}t \tag{III.5}$$

where $\Delta L/L_o$ is the shrinkage of the powder, γ ($J\,m^{-2}$) is the surface energy, D (m) is the average particle diameter, η (Pa s) is the coefficient of viscosity and t (s) is the time. Over a small range of temperature, the coefficient of viscosity of an amorphous material follows an Arrhenius equation expressed as [1]:

$$\eta = \eta_o \exp\left(\frac{Q}{RT}\right) \tag{III.6}$$

where η_o (Pa s) is the frequency factor, Q ($J\,mol^{-1}$ is the activation energy for viscous flow, R ($8.314\,J\,K^{-1}\,mol^{-1}$) is the universal gas constant and T (K) is the absolute temperature. The linear relationship between the temperature and the time, as in this case, can be expressed as:

$$\frac{dT}{dt} = c \tag{III.7}$$

where c ($0.417\,K\,s^{-1}$)) is the constant rate of heating employed here. The shrinkage rate expressed in Eq. III.5 can be extended to constant rate heating conditions by differentiating this equation with respect to temperature as:

$$\frac{d\left(\frac{\Delta L}{L_o}\right)}{dT} = \frac{3\gamma}{4Dc\eta_o} \exp\left(\frac{-Q}{RT}\right) \tag{III.8}$$

The left hand side of Eq. III.8 involves estimation of the slope of the shrinkage with respect to temperature at different temperatures. This function is extremely sensitive to the measurement of contraction of the powder and the heating rate [116]. The resolution of 0.1 mm in the measurement of the punch position makes the collection of data relevant to Eq. III.8 rather difficult. Minute variations in the heating rate also pose an additional problem to the above. therefore, it is suitable to integrate Eq. III.8 to yield, approximately,

$$\frac{\Delta L}{L_o} \cong \frac{3\gamma R T^2}{4DcQ\eta_o} \exp\left(\frac{-Q}{RT}\right) \qquad \text{(III.9)}$$

It should be noted that both the differential (Eq. III.8) and the integral (Eq. III.9) forms yield identical values for the viscous flow parameters [117]. In obtaining Eq. III.9 it was assumed that γ, η_o and Q are constant. Although the values of these parameters change gradually with temperature, over small temperature intervals, such variation is negligible and can thus be considered to be approximately independent of temperature [116]. Eq. III.9 suggests that the data relevant to $(\Delta L/L_o)/T^2$ when plotted with respect to 1/T in a semi-log plot should show a linear relationship over a limited range of temperature.

The parameter $(\Delta L/L_o)/T^2$ for this investigation was calculated and plotted with respect to 1/T, with the linear part in the temperature range of 525 to 580 °C, as presented in Fig. 11. In light of the approximate form of Eq. III.9 and the limitations discussed previously, this linear relationship confirms the viscous flow to be the mechanism of sintering of the $Fe_{48}Cr_{15}Mo_{14}Y_2C_{15}B_6$ metallic glass powder. The argument regarding constant γ, η_o and Q is also valid and thus enables the estimation of the activation energy for viscous flow over the above range of temperature. This was estimated from the slope according to Eq. III.9 to be 94.0 ± 0.2 kJ mol^{-1}. This order of magnitude of the activation energy is identical to the one obtained by Liu *et al.*, for viscous flow of Ti-based metallic glass powder during SPS [1].

In order to examine the validity of the estimated activation energy for viscous flow, the above results were compared with those pertaining to the nonisothermal shear viscosity of the

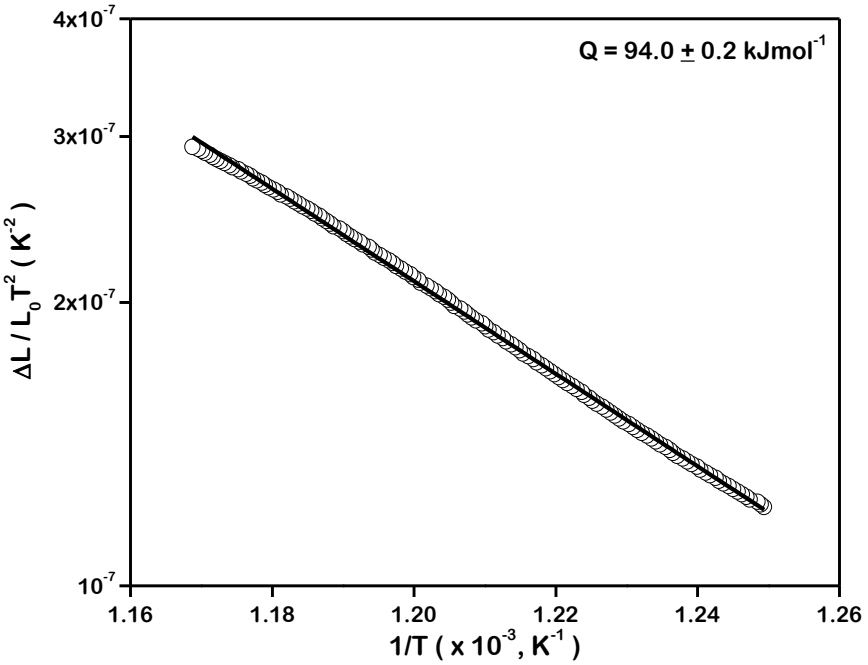

Figure 11: Plot of parameter $(\Delta L/L_o)/T^2$, during SP sintering of $Fe_{48}Cr_{15}Mo_{14}Y_2C_{15}B_6$ metallic glass powder, with 1/T in the temperature interval of 525 °C to 580 °C. The activation energy is estimated in this temperature range to be 94.0 ± 0.2 kJ mol^{-1}

$Fe_{48}Cr_{15}Mo_{14}Y_2C_{15}B_6$ bulk metallic glass as measured by Lu *et al* [118]. The relevant data were plotted according to Eq. III.6, in the same range of temperature as in this investigation and is presented in Fig. 12. The activation energy for viscous flow was estimated to be 298.0 ± 3.0 kJ mol^{-1} from the slope. It is to be noted that the above measurement of the nonisothermal viscosity is based on the deflection of a beam machine from cast metallic glass alloy ingots under the application of a vertical force and its own weight. In contrast, the present analysis is carried out based on the viscous flow of powder particles. The latter occurs due to the driving force of surface tension, due to the presence of the free surface at the interparticle contacts. Viscous flow is easier in the present case, the estimated lower activation energy being a manifestation of the same. Additionally, it has been observed that an increase in the heating rate reduces the activation energy for viscous flow [1]. Thus

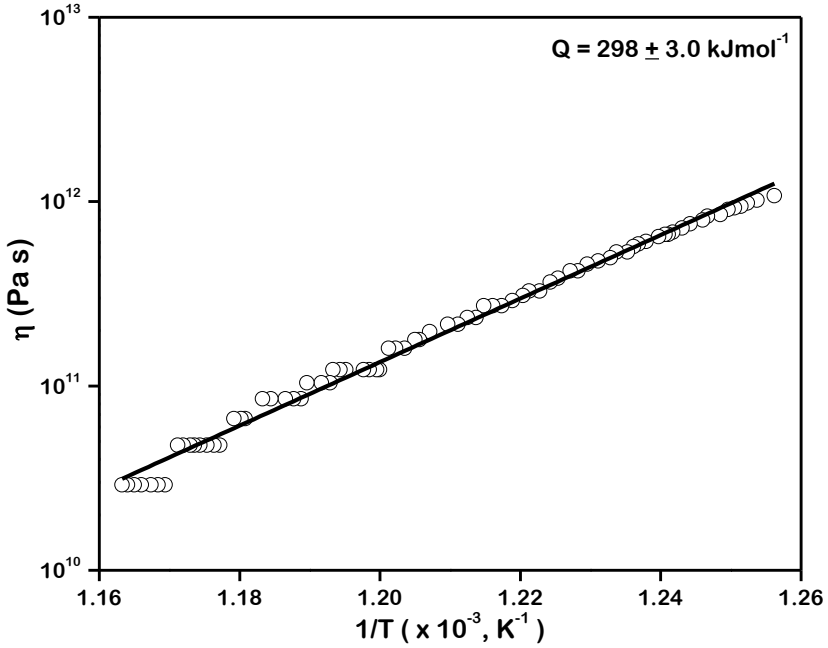

Figure 12: Activation energy of viscous flow of $Fe_{48}Cr_{15}Mo_{14}Y_2C_{15}B_6$ metallic glass, estimated by three point bending. Adapted from [1]

the higher heating rate of 25 °C min^{-1} as compared to 4 °C min^{-1}, as employed in the above work, has resulted in a lower activation energy.

5 Heating rate

5.1 Activation energy adaptation

In order to understand the inherent role of heating rate on the activation energy of viscous flow and hence on the densification kinetics of $Fe_{48}Cr_{15}Mo_{14}Y_2C_{15}B_6$ metallic glass powder, SPS was performed at heating rates of 50, 100 and 150 °C min^{-1}. It can be observed from Fig. 13 the powder compact underwent an initial contraction of 1.2 mm followed by an additional 0.4 mm in two discrete stages of densification during SPS up to SI1000°C at each heating rate. Minute variations existed in the mass of powder poured into the die

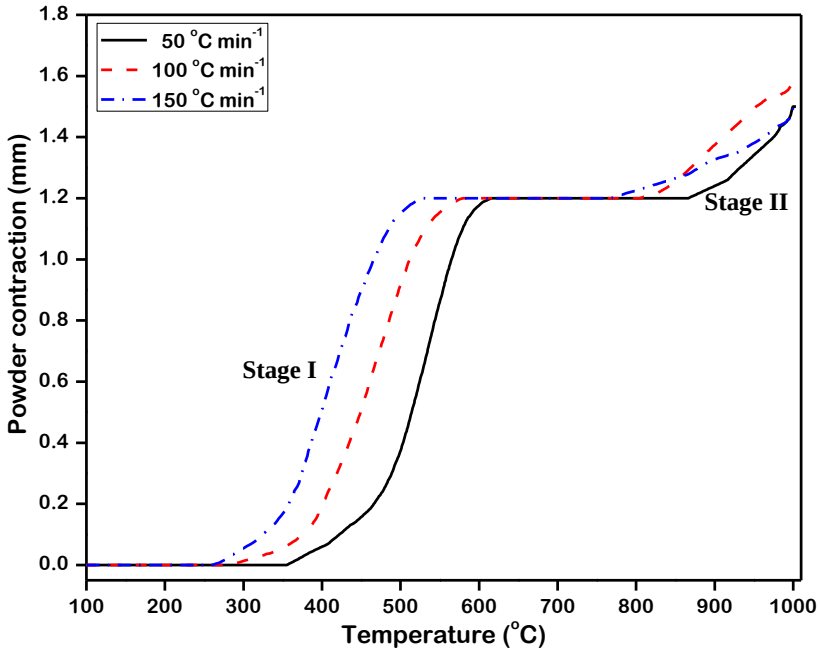

Figure 13: Contraction of $Fe_{48}Cr_{15}Mo_{14}Y_2C_{15}B_6$ metallic glass powder during SP sintering at heating rates of 50 °C min^{-1}, 100 °C min^{-1}and 150 °C min^{-1}

and consequently the values of ρ_o utilized for estimating $\dot{\rho}_n$ during SPS at different heating rates were 54, 59 and 60% at 50, 100 and 150 °C min^{-1} respectively. The instantaneous densification rate was plotted according to Eq. III.4 with the time interval (t_{n+1} - t_{n-1}) as 2 s, at different heating rates and the results are presented in Fig. 14. While a distinct trend in the densification rate is evident upon a systematic increase in the heating rate during Stage I, the same cannot be concluded from about Stage II. The characteristics of the former, such as temperature of onset densification (T_s), peak densification rate (T_p) and end of densification (T_f) occurred are observed to shift to lower values while there is a steady increase in the peak densification rate ($\dot{\rho}_p$) as the heating rate increased. These observations are summarized in Table 3.

The increase in densification rate during Stage I with the rate of heating rate was sub-

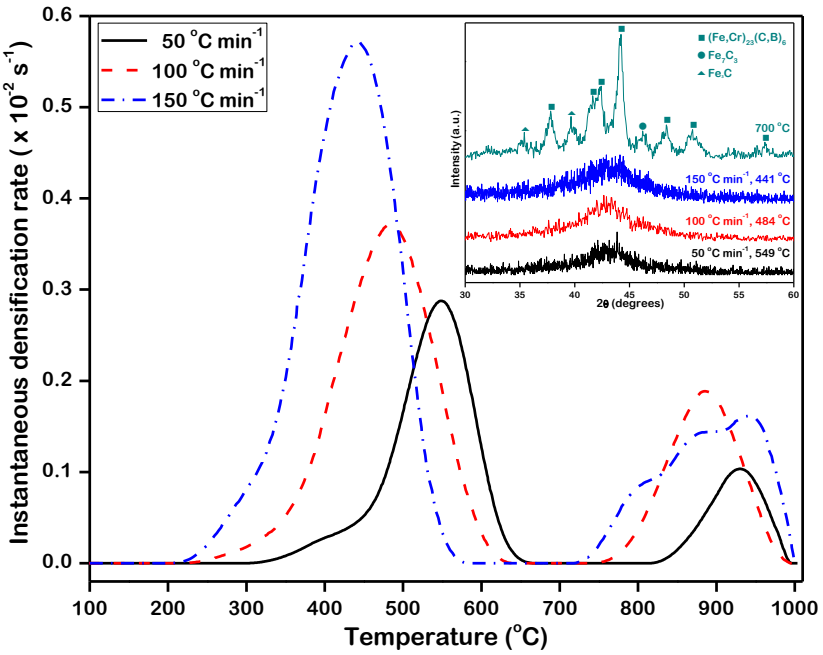

Figure 14: Instantaneous densification rates in $Fe_{48}Cr_{15}Mo_{14}Y_2C_{15}B_6$ metallic glass powder during SP sintering at heating rates of 50 °C min^{-1}, 100 °C min^{-1}and 150 °C min^{-1}. *Inset* represents the X-ray diffraction spectra of samples sintered at peak densification temperatures corresponding to different heating rates and a representative temperature before onset of Stage II

Table 3: Characteristics of Stage I during SP sintering of $Fe_{48}Cr_{15}Mo_{14}Y_2C_{15}B_6$ metallic glass powder at heating rates of 50 °C min^{-1}, 100 °C min^{-1}and 150 °C min^{-1}

c (°C min^{-1})	T_s (°C)	T_p (°C)	T_f (°C)	$\dot{\rho}_p$ (s^{-1})
50	300	549	667	0.0029
100	221	484	641	0.0037
150	205	441	582	0.0057

jected to further investigation. The glass transition temperature, T_g of this alloy measured at a heating rate of 20 °C min^{-1} is 575 °C [119] which is expected to increase at higher heating rates as as investigated here [120, 3]. The maximum densification rate during SPS at 50. 100 and 150 °C min^{-1} was attained at 549, 484 and 441 °C respectively, all of which are below the

T_g where the material remains in its glassy state. Indeed the X-ray diffraction analysis of the samples sintered at these temperatures with respective heatnig rates exhibiteed a diffused halo (inset, Fig. 14) characteristic of fully amorphous materials. Thus during SPS at each heating rate, in the entire range from respective start to peak temperature in Stage I, the samples is fully amorphous suggesting the occurrence of viscous flow. In contrast, during SPS at 700 °C and above in Stage II at all heating rates, the samples are fully crystalline as shown by one representative XRD spectrum (inset, Fig. 14). The parameter, $(\Delta L/L_o)/T^2$ plotted with respect to 1/T shows a linear behavior in the temperature ranges of 447 to 549, 345 to 484 and 323 to 441 °C at the heating rates of 50, 100 and 150 °C min^{-1} respectively as shown. In view of the limitations of measurement noted previously and the approximate form of Eq. III.9, this confirms the mechanism of mass transport to be viscous flow. The activation energy for viscous flow is estimated from the slopes according to Eq. III.9, in these temperature intervals, to be 76.2 ± 0.4 kJ mol^{-1}, 64.0 ± 0.9 kJ mol^{-1} and 55.2 ± 1.0 kJ mol^{-1} at heating rates of 50, 100 and 150 °C min^{-1}, respectively.

Although the T_g of a metallic glass alloy increases with heating rate, the viscosity below the T_g reduced due to irreversible structural relaxation. This is quantitatively explained by the directional structural relaxation (DSR) model [121], where the the viscosity of a metallic glass at a given temperature velow the T_g, is inversely proportional to the heating rate [122]. Assuming η_o to be independent of the heating rate, the activation energy evaluated at a given temperature should decrease logarithmically as the heating rates are increased. Since the variation of activation energy over small intervals of temperature is neg-

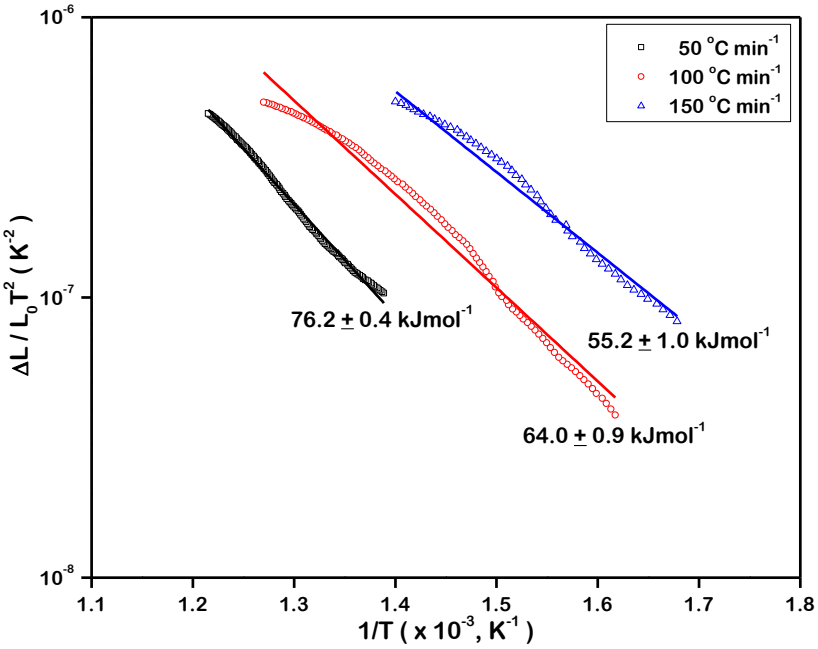

Figure 15: Plot of parameter $(\Delta L/L_o)/T^2$, during SP sintering of $Fe_{48}Cr_{15}Mo_{14}Y_2C_{15}B_6$ metallic glass powder at different heating rates, with 1/T in the corresponding temperature intervals. The activation energies are estimated in these temperature intervals to be 76.2 ± 0.4, 64.0 ± 0.9 and 55.2 ± 1.0 kJ mol^{-1} respectively

ligible, the gradual reduction in the activation energy for viscous flow with increasing heating rate indicates considerable agreement with the DSR model. This inherent relationship between the activation energy for viscous flow and the employed heating rate is discussed in the following section.

6 Directional structural relaxation

6.1 Unification of models

In order to investigate the observed reduction in activation energy for viscous flow with increasing heating rates of isochronal SPS, the theoretical framework of the directional structural relaxation (DSR) model was utilized. This model helps delineate the strong depen-

dence of viscosity of amorphous alloys below their T_g on the heating rate. Such dependence is a direct result of structural relaxation phenomena occurring in amorphous alloys. These constitute a set of irreversible elementary atomic rearrangements that ensue at specific sites or relaxation centers within the amorphous alloy. Hence the kinetics of this structural relaxation is determined by the volume density of relaxation centers operating at at a particular temperature. Pertaining to the analysis relevant to the present investigation, the viscosity of amorphous alloys below the t_g is found to be inversely proportional to the heating rate and this relationship is quantitatively expressed as [123]:

$$\ln \eta = -\ln c + B \tag{III.10}$$

where η (Pa s) is the coefficient of viscosity, c ($K\,s^{-1}$ is the constant rate of heating and B is a parameter related to the energy of atomic rearrangements at the relaxation centers that is governed solely by temperature.

Over a small range of temperature, the viscosity of an amorphous alloy can also approximately described by the Arrhenius equation expressed as Eq. III.6. A comparison of Eqs. III.10 and III.6 yields, upon rearrangement of th terms,

$$Q = -RT \ln c + RT(B - \ln \eta_o) \tag{III.11}$$

The observed reduction in activation energy for viscous flow with the heating rate during isochronal SPS of $Fe_{48}Cr_{15}Mo_{14}Y_2C_{15}B_6$ metallic glass powder is predicted by Eq. III.11.

In order to establish an explicit relationship, the variation in the activation energy

with the heating rate must be investigated independent of or, in other words, at a constant temperature. However, the temperature ranges where viscous flow could be analyzed at the employed heating rates were distinct from one another. Nevertheless Eq. III.6 is based upon the assumption that the fluctuation in Q over a limited interval of temperature is minimal. Hence this permits extrapolation of the straight lines that were fitted to the shrinkage data for estimation of activation energies. The results of this operation performed on the data corresponding to 0.42 and 2.50 $\mathrm{K\,s^{-1}}$ (50 and 150 $\mathrm{^{\circ}C\,min^{-1}}$) are presented in Fig. 16. This operation leads to a specific temperature, about 773 K (500 °C), applicable to all heating rates to be obtained. According to Eq. III.6 η_o is the value of η attained as T tends to infinity or, in other words, the viscosity of the amorphous alloy at extremely high temperatures. This limiting value of η, expressed as [124]:

$$\ln \eta_o = \frac{N_A h}{V_m} \tag{III.12}$$

where N_A ($6.023 \times 10^{23}\,\mathrm{mol^{-1}}$) is the Avogadro's constant and h ($6.6263 \times 10^{-34}\,\mathrm{J\,s}$) is the Planck constant, depends solely on the molar volume V_m ($6.65 \times 10^{-6}\ \mathrm{m^3}$) [125], a material property of the $Fe_{48}Cr_{15}Mo_{14}Y_2C_{15}B_6$ metallic glass. This yields a value of $6.0 \times 10^{-5}\,\mathrm{Pa\,s}$, agreeing well with that estimated by Na *et al.* [98] to be $5.9 \times 10^{-5}\,\mathrm{Pa\,s}$ for the $Fe_{48}Cr_{15}Mo_{14}Y_2C_{15}B_6$ metallic glass employed in this investigation. Finally the parameter B, determined solely by temperature as discussed earlier, is constant at the specific temperature. Hence rather than monitoring B separately, the entire term RT(B - $\ln\eta_o$) could be obtained by examining the variation of Q with c. Thus it can be concluded that at the aforesaid specific temperature,

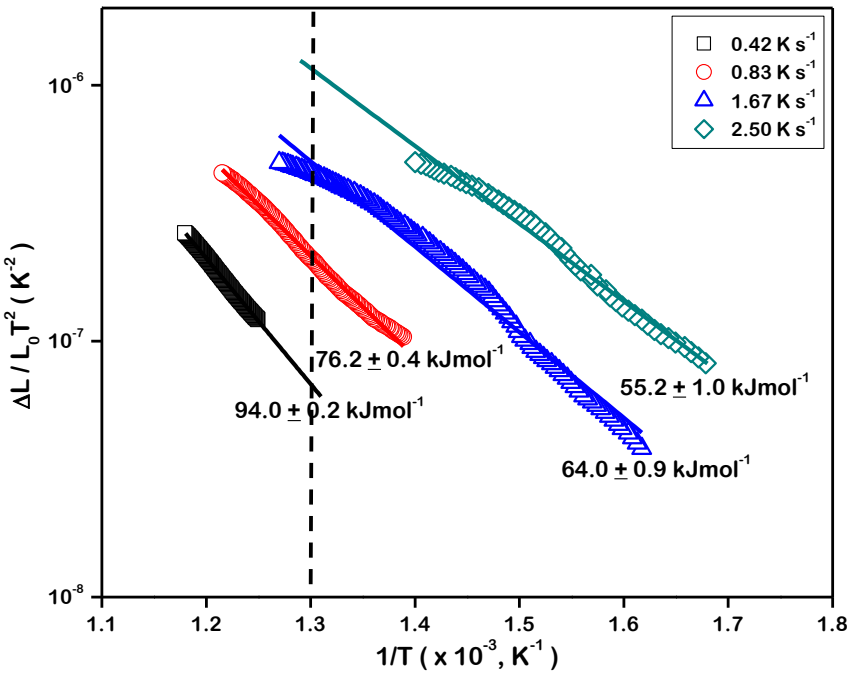

Figure 16: Extrapolation of parameter parameter $(\Delta L/L_o)/T^2$, during SP sintering of $Fe_{48}Cr_{15}Mo_{14}Y_2C_{15}B_6$ metallic glass powder at different heating rates. The specific temperature of analysis, applicable to all heating rates obtained to be 773 K is represented by a *dashed line*

the terms RT and RT(B - $\ln\eta_o$) in Eq. III.11 are constants.

6.2 Theoretical relationship

In light of this discussion, Q varies linearly with respect to lnc. However, in order to visualize the actual values of c as opposed to observing their logarithm, the application of this mathematical operator has been refrained from. Instead, the X-axis in the plot, presented in Fig. 17, has been converted to log-scale (base2) while keeping c unaltered. The result leads to the derivation of the following relationship:

$$Q = (-22.8 \pm 0.4)\ln c + 73.7 \qquad \text{(III.13)}$$

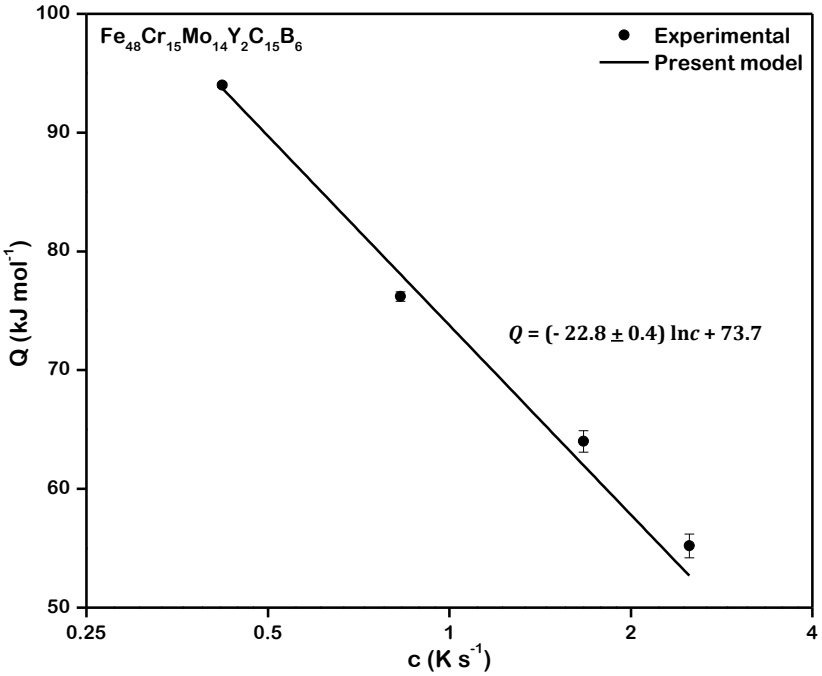

Figure 17: Activation energy of viscous flow in $Fe_{48}Cr_{15}Mo_{14}Y_2C_{15}B_6$ metallic glass powder as a function of heating rate during SP sintering

The activation energy for viscous flow during isochronal SPS of $Fe_{48}Cr_{15}Mo_{14}Y_2C_{15}B_6$ metallic glass powder below its T_g can thus be predicted at any heating rate.

In order to examine the general applicability of such a linear relationship, results obtained by Liu *et al.* [126] on the activation energy of viscous flow during isochronal SPS of Ti-based metallic glass powder of composition $Ti_{40.6}Zr_{9.4}Cu_{37.5}Ni_{9.4}Al_{3.1}$ (at.%) were subjected to an identical analysis. An increase in the heating rate from 0.33 through 1.33 too 2.33 $K\,s^{-1}$ led to a continuous reduction in the activation energy from 83.1 through 68.9 to 57.5 ($kJ\,mol^{-1}$). The specific constant temperature, applicable to all heating rates obtained in this case was 606 K (333 °C), below the T_g, 631 K (358 °C) of this metallic glass alloy. At this temperature similar treatment, as above was carried out that resulted in the establishment of the relationship as presented in Fig. 18:

$$Q = (-12.6 \pm 2.1) \ln c + 70.0 \quad \text{(III.14)}$$

Eqs. III.13 and III.14 thus confirm the validity of a linear relationship to predict the activation energy for viscous flow of metallic glass powders during isochronal SPS below their T_g [127].

6.3 Limitations

In implementing Eqs. III.13 and III.14, the following assumptions, made during its deduction, must be considered. The foremost was the applicability of the Arrhenius equation with constant Q in describing the viscosity of the metallic glass over small ranges of temperature. Hence confirmation of a linear relationship between the shrinkage of the power and 1/T leading to the estimation of a unique value of Q is fundamental to the validity of the same. Likewise, the DSR model is valid below the T_g of the alloy, thereby restricting the application of the obtained equations only to such temperatures. Moreover, it is not bereft of a few, although comprehensible, limitations. For example, Eq. III.11 suggests that a plot of Q with respect to lnc should exhibit a slope of -RT. However, the estimated slopes in Eqs. III.13 and III.14 are considerably different from the values of the above parameter at th corresponding temperatures of discussion. This disparity stems from the fact that the Arrhenius and DSR models delineate the viscous flow as a function of temperature alone. In contrast, during SPS the viscous flow driven by surface tension at the interparticle contacts is governed by additional variables of which current is of key importance. The

application of an electric field exhibited pronounced effects on mass transport processes such as electromigration and interdiffusion [128]. The kinetics of these processes are dependent on the properties of the material such as defect mobility and diffusivity. This explains the fact that while Eqs. III.13 and III.14 both validate a linear relationship for predicting the activation energy, they are characteristic to the composition of the metallic glass alloy. Furthermore, Joule heating renders the isolation of the intrinsic effects of the pulsed direct current from those of the resulting temperature even more convoluted. These effects may this change the kinetics of sintering without modifying the mechanism therein. Indeed viscous flow was manifested during both SPS and creep [118] of the $Fe_{48}Cr_{15}Mo_{14}Y_2C_{15}B_6$ metallic glass. However, while the activation energy for the latter was estimated to be 298.0 ± 3.0 $kJ\,mol^{-1}$ at a heating rate of $0.07\,K\,s^{-1}$, the corresponding value predicted by the present relationship (Eq. III.13) is lesser, $135.4\,kJ\,mol^{-1}$. This emphasizes the effect of phenomena unique to the SPS process on this parameter A similar discussion holds for the estimated intercepts as well.

7 Applied pressure

7.1 Densification

In order to understand the effect of applied pressure on the densification of Fe - based bulk amorphous alloy during spark plasma sintering, the increase in the fractional density, ρ, of the compacts with temperature under 20, 30, 50 and 70 MPa was investigated. With an increase in the applied pressure the thickness of the green compacts decreased

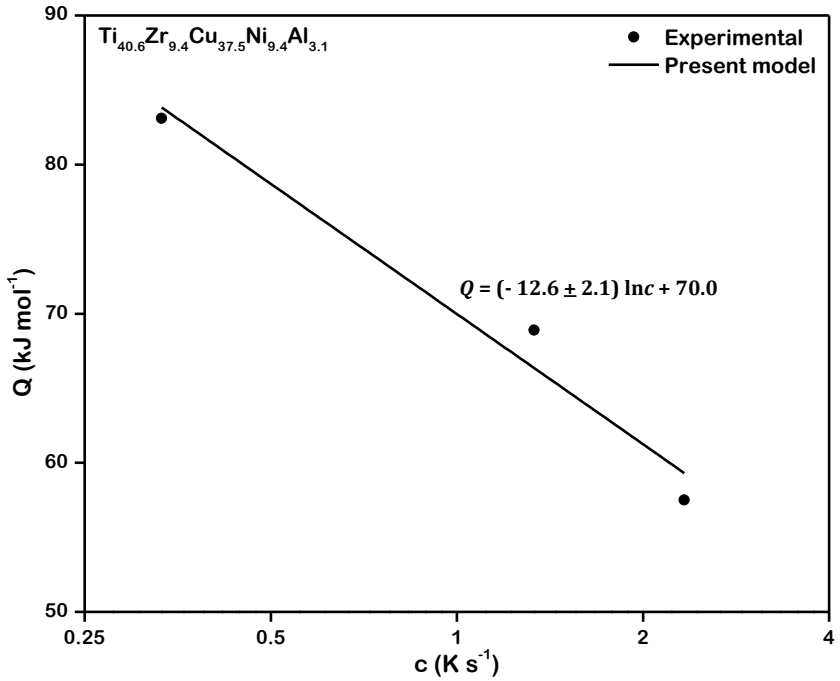

Figure 18: Validation of the linear relationship between activation energy of viscous flow as a function of heating rate in $Ti_{40.6}Zr_{9.4}Cu_{37.5}Ni_{9.4}Al_{3.1}$ metallic glass powder during SP sintering

progressively and were measured to be 6.9, 6.6, 6.5 and 6.1 mm under 20, 30, 50 and 70 MPa, respectively. The corresponding values of ρ_o used for estimating ρ were 0.63, 0.65, 0.66 and 0.67. The estimated fractional densities are presented in Fig. 19. It can be clearly observed that under all applied pressures the fractional density increased with temperature during sintering. In general, with an increase in the applied pressure from 20 to 70 MPa the fractional density attained higher values at the same temperature of sintering. Some aberrations from this general trend were observed around 540 °C for 30 and 50 MPa, possibly due to minute variations in the mass of powder that occurred during pouring into the die for sintering as well as the resolution in the measurement of punch displacement. However, the overall trend of an increase in fractional density with applied pressure was valid. Indeed, under the highest applied pressure of 70 MPa in this study, the compact underwent the

largest densification attaining the highest fractional density of almost 0.98 at the end of the sintering cycle. On the other hand, the final fractional density attained by the compact sintered under an applied pressure of 20 MPa was, in contrast, only 0.80.

7.2 Contact pressure

The enhancement of densification with the increase in applied pressure was further investigated in order to identify its inherent effect. During pressure - assisted sintering there exists a considerable difference between the macroscopic applied pressure and the microscopic contact pressure at the individual interparticle contacts. In particular, during the intermediate stages of sintering when the density of the compact is low, the adjacent particles just touch each other and the area of contact between them is extremely small as compared to the size of the particles [129]. In these conditions, the applied pressure employed by the punches can be significantly intensified to a much higher local contact pressure conveyed at these interparticle contacts. With the progress of sintering, the area of contact between adjacent particles increases and the contact pressure decreases continuously as the density of the compact approaches theoretical density [130]. Thus in order to understand the amplification of the macroscopic applied pressure, the variation in the diameter of the area of contact with the progress of sintering must be estimated first.

The relationship between the diameter of the area of interparticle contact and the fractional density can be obtained according to Coble's analysis of the evolution of structural geometry in a compact during sintering [131]. This is based on the model of packed tetrakaidecahedra, that fills space most efficiently and hence is in excellent accord with the

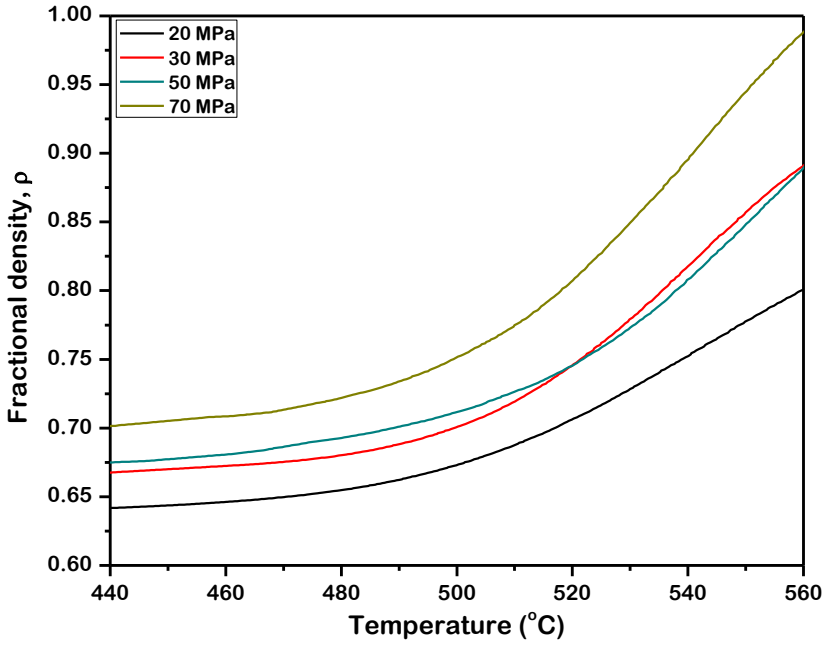

Figure 19: Fractional density of $Fe_{48}Cr_{15}Mo_{14}Y_2C_{15}B_6$ metallic glass powder compacts during SP sintering at microscopic applied pressures of 20 MPa, 30 MPa, 50 MPa and 70 MPa. Green and final densities of compacts increased with applied pressure

high densities observed in this investigation. An example of a particle with such a polyhedral structure within the compact is presented in Fig. 20. In this model the tetrakaidecahedral particles enclose, between them, cylindrical pores which are coaxial with and dispersed along the polyhedron edges. The length of the edges are utilized to calculate the surface area and volume of the polyhedra. These thereby yield the diameter of the area of contact D_c (µm). The radius of the cylinders, along with their length, is employed to calculate the volume of the pores. The two volumes, namely those of the pores and the polyhedra yield the fractional density, ρ as a function of D_c expressed as [132]:

$$\left(\frac{D_c}{D_p}\right)^2 = 1 - \left(\frac{\pi}{3\sqrt{2}\rho}\right)^{\frac{2}{3}} \tag{III.15}$$

where D_p (40 µm) is the diameter of the particle. Eq. III.15 is valid for high fractional densities (ρ >0.74) and the following analysis is also focused in these density regimes. It is utilized to estimate the contact pressure, P_c (Pa) as [133]:

$$P_c = \frac{4}{\pi} P_a \left(\frac{D_p}{D_c} \right)^2 \quad \text{(III.16)}$$

where P_a (20, 30, 50 and 70 MPa) is the applied pressure. The estimated contact pressures are presented in Fig. 21 as a function of the fractional density of the compacts under different applied pressures from 20 to 70 MPa. It can be observed that when the density is low the contact pressure is significantly higher than the applied pressure. Under all applied pressures, the contact pressures are larger by almost two orders of magnitude. With the progress of sintering, as the density of the compacts increased the contact pressure decreased rapidly under all applied pressures. Additionally, the contact pressure increased with the applied pressure as indicated by Eq. III.16.

7.3 Micro-viscous flow deformation

The occurrence of high compressive pressures, as observed in Fig. 21 at the local microscopic interparticle contacts suggests the possibility of significant deformation of the particles of the powder during the progress of sintering. Deformation of powder has been observed to contribute to [134] and even dominate the densification of compacts during spark plasma sintering [132]. This consideration is also in accord with the observed enhancement of densification with the increase in applied pressure. This mandates the investigation of

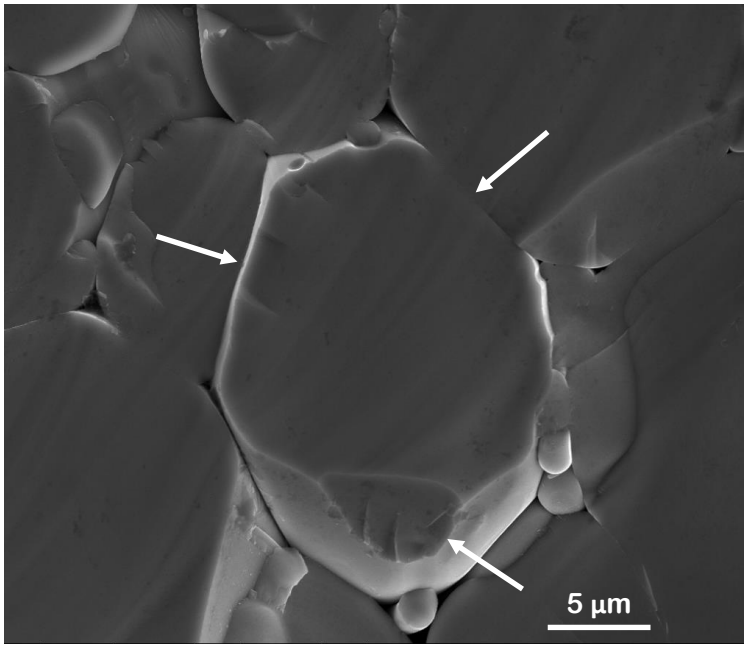

Figure 20: Representative polyhedral particle of $Fe_{48}Cr_{15}Mo_{14}Y_2C_{15}B_6$ metallic glass powder during SP sintering. *Arrows* represent flat facets

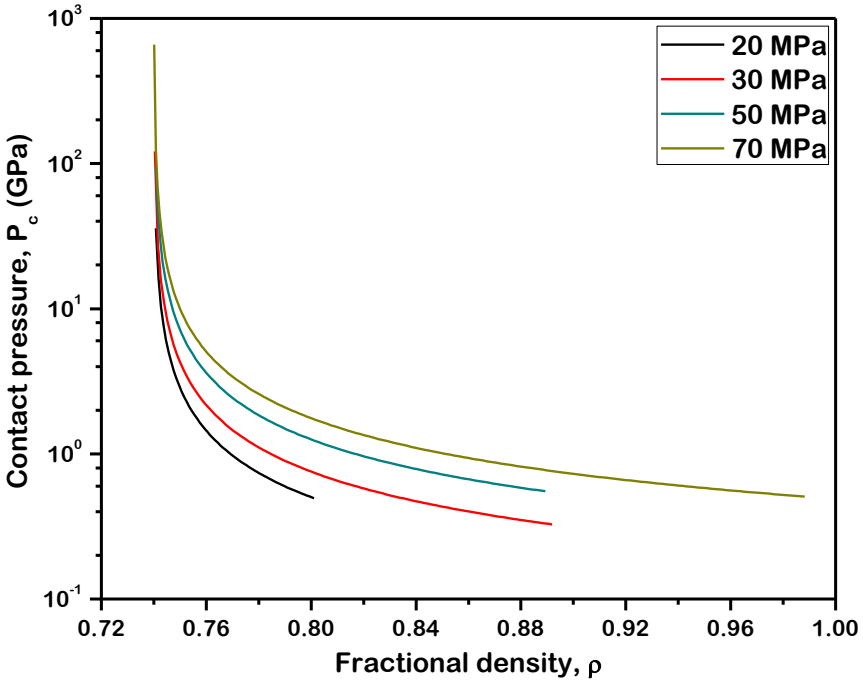

Figure 21: Evolution of microscopic interparticle contact pressure during SP sintering of $Fe_{48}Cr_{15}Mo_{14}Y_2C_{15}B_6$ metallic glass powder

the effect of contact pressure on the compressive deformation of particles and its resulting contribution to sintering. However, the present conditions do not conform to the conventional compression of metallic materials at elevated temperatures carried out according to ASTM E209 standard [135]. The powder particles employed in this study are mostly spherical with a diameter of about 40 µm whereas samples designated in the ASTM standard are cylindrical with a much larger diameter of about 25 mm. The system was also not maintained at a constant elevated temperature. Hence estimation of deformation by conventional stress - strain measurements are not applicable in the present case. On the other hand, viscous flow deformation has been reported in single Fe - based metallic glass alloy particles [136, 137] in contrast to dislocation mediated plastic deformation in metals. During sintering, the applied pressure is conveyed to the spherical particles by its adjacent neighbors. The contact pressure deforms the spheres to a configuration of a tetrakaidecahedron with flat facets [131, 138]. Thus all individual particles undergo viscous deformation between a number of pairs of flat surfaces. This is analogous to the model of deformation of a single sphere between two flat plates under compressive loading [139, 140], presented with the help of a schematic in Fig. 33. In the following paragraphs the viscous flow deformation of an individual sphere of Fe - based glassy alloy under compressive loading between two flat facets is estimated as a representative of all the particles in the bulk amorphous alloy compact.

The viscous deformation of a single sphere between two flat plates under compressive load can be expressed in differential form as [136]:

$$\frac{dh}{dt} = \frac{F}{16\eta D_{\mathrm{c}}} \tag{III.17}$$

where dh (µm) is half the incremental displacement of one plate with respect to another and dt (s) is the time. dh/dt ($\mu m\,s^{-1}$) is thus referred to as the compressive speed. F (N) is the compressive load and η (Pa s) is the viscosity of the $Fe_{48}Cr_{15}Mo_{14}Y_2C_{15}B_6$ metallic glass powder during pressure - assisted SPS. The compressive force, F can be expressed in terms of the contact pressure, P_c and the diameter of the area of contact, D_c as:

$$F = P_{\mathrm{c}}\left(\frac{\pi}{4}D_c^2\right) \tag{III.18}$$

Application of Eq. III.16 for P_c and rearrangement of terms yield:

$$\frac{dh}{dt} = \left(\frac{P_{\mathrm{a}}D_p^2}{16}\right)\frac{1}{\eta D_{\mathrm{c}}} \tag{III.19}$$

The relationship between temperature and time in the present constant heating rate experiments can be expressed as:

$$\frac{dT}{dt} = c \tag{III.20}$$

where T (K) is the temperature and c ($0.417\,K\,s^{-1}$) is the constant rate of heating. Replacement of dt in Eq. III.19 results in:

$$\frac{dh}{dT} = \left(\frac{P_{\mathrm{a}}D_p^2}{16c}\right)\frac{1}{\eta D_{\mathrm{c}}} \tag{III.21}$$

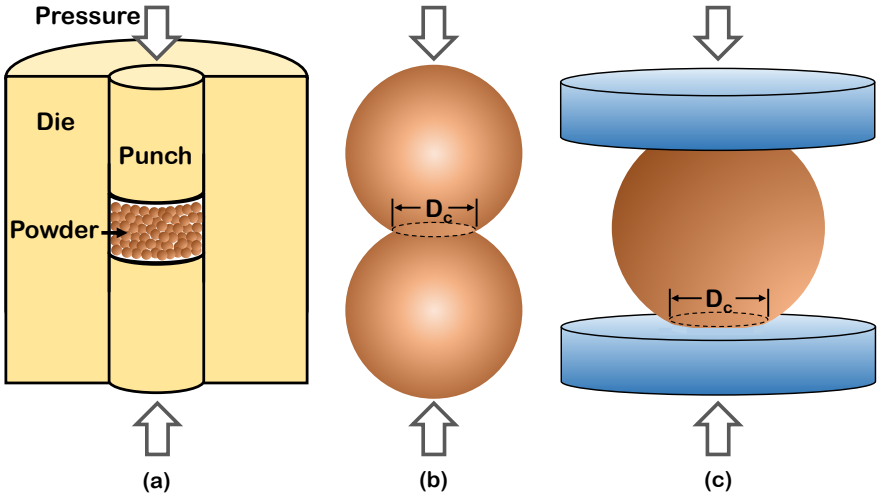

Figure 22: Schematic representing analogy between (a) SPS, (b) deformation between adjacent particles and (c) deformation of a single sphere between two flat plates during compressive loading

It is noteworthy, that in Eq. III.21 all the parameters within the parenthesis are constant in a particular experiment while those outside vary with T. The variation of the viscosity, η with temperature during pressure - assisted SPS can be estimated as [130]:

$$\eta = \frac{3P_{\mathrm{a}}\left(1-\rho_{\mathrm{o}}\right)\left(1-\rho\right)}{4\rho^{2}\left(\rho-\rho_{\mathrm{o}}\right)\left(\frac{d\rho}{dt}\right)} \tag{III.22}$$

and is utilized for estimating dh/dt. This is further integrated to obtain Δh (µm), the total viscous flow deformation of an individual particle during the sintering cycle.

7.4 Theoretically calculated density

The total deformation, Δh is plotted with respect to temperature under different pressures from 20 to 70 MPa and the results are presented in Fig. 23. It clearly exhibits

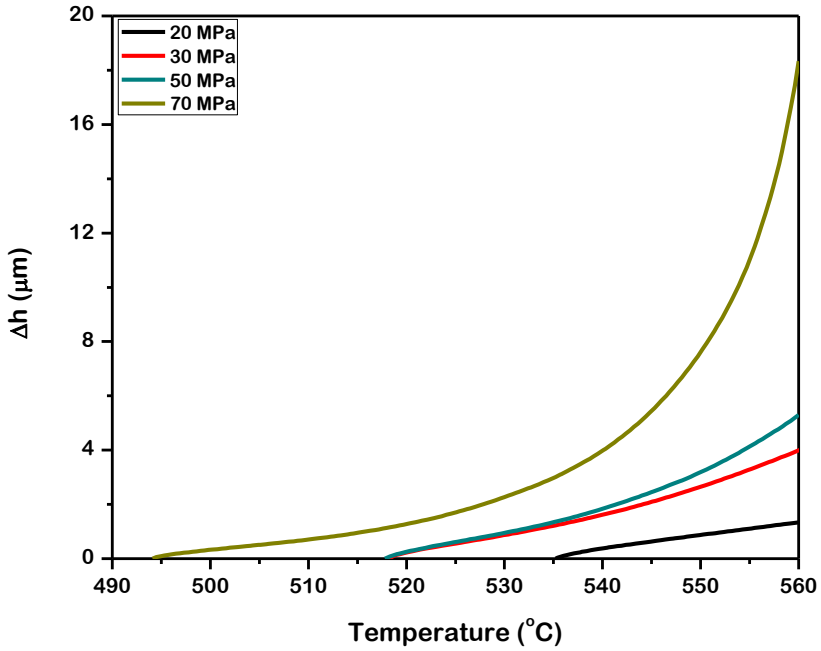

Figure 23: Total viscous flow deformation of an individual representative sphere of $Fe_{48}Cr_{15}Mo_{14}Y_2C_{15}B_6$ metallic glass powder during SP sintering at different macroscopic applied pressures

the inherent effect of pressure and its resulting contribution to the spark plasma sintering of Fe - based bulk amorphous alloy. An increase in applied pressure from 20 to 70 MPa brought about an increase in compressive viscous flow deformation of the particles of the powder from 1.3 to 18.3 μm. The particles that underwent higher deformation thereby filled space or pores in the compact more efficiently during the progress of sintering. This led to enhanced densification with the observed highest density being attained under the largest applied pressure.

The total deformation, Δh was utilized to theoretically calculate the fractional density, ρ_{theo}, of the compacts and compare them with ρ, the experimentally observed ones. In accordance with the high densities observed in this investigation, the compacts were assumed to constitute of a number of layers of close - packed spheres stacked upon one another.

The number of layers, n can be obtained from the simple relationship depicting the vertical distance between the center of the spheres as a function of their diameter as:

$$n = \sqrt{\frac{3}{2}} \frac{L_o}{D_p} + 1 \tag{III.23}$$

The number of layers times the deformation of an individual particle yields the reduction in height of the compact which leads to the estimation of ρ_{theo}. The results are presented in Fig. 24 which are in clear agreement with the observed trend of increase in fractional density with applied pressure. Hence the present model is suitable to analyze the contribution of viscous flow deformation to the densification of amorphous alloy powder during pressure - assisted SPS.

7.5 Limitations

Certain limitations of the same must also be considered. A comparison of Figs. 19 and 24 shows that the theoretical calculations result in an underestimation of the experimentally observed fractional density attained under a pressure of 20 MPa. This is possibly due to the fact that the present analysis only accounts for the particle deformation as means of densification of the compact which initiates at around 535 °C while completely ignoring surface tension driven mass flow at the interparticle contacts occurring at lower temperatures. On the other hand, there is a considerable overestimation under a pressure of 70 MPa, since, according to this model, the deformation of particles can progress unrestricted with an increase in applied pressure. For example, under this pressure, the calculated value of Δh

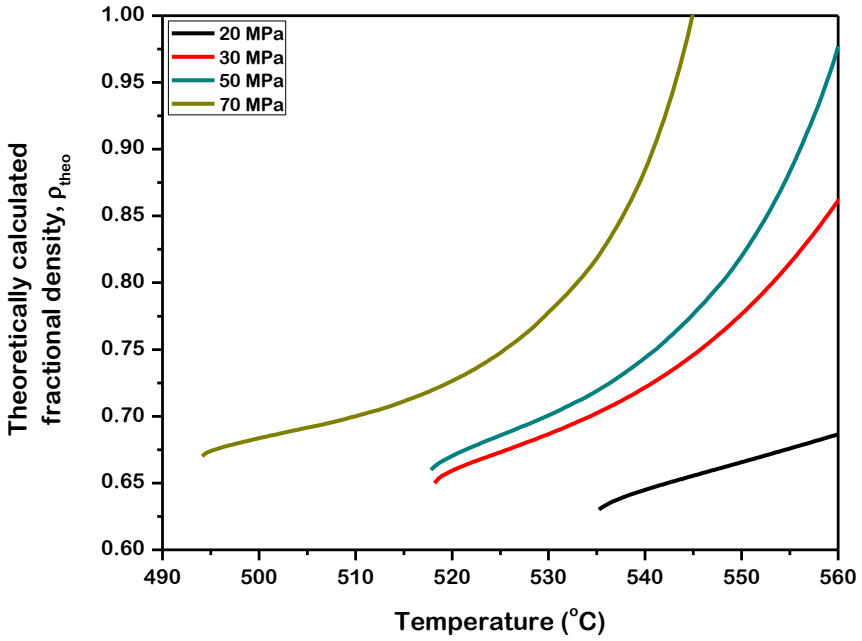

Figure 24: Theoretically calculated fractional densities of $Fe_{48}Cr_{15}Mo_{14}Y_2C_{15}B_6$ metallic glass powder compacts during SP sintering at different applied macroscopic pressures

(16 µm) is expected to yield almost flattened particles, the occurrence of which was not detected. From this, it can be inferred that above a certain pressure the densely packed particles that fill up space and the die walls significantly impede continued deformation resulting in lesser densification than theoretically calculated. Thus a further analysis of the relative contributions of surface tension driven mass flow and pressure controlled viscous flow deformation towards consolidation of amorphous alloy powder during SPS is necessary to accurately predict fractional densities finally attained in the process.

In spite of these limitations, the novelty of the present analysis resides in the quantification of the effect of pressure on densification of amorphous alloy powder during SPS. In fact, the employed heating rate is reasonably low that justifies the broader applicability of this model to a wide range of powder consolidation techniques beyond SPS where high

densities (>0.74) are achieved. Yet, the dominant manifestation of the effect of pressure in achieving such high densities due to internal Joule heating mechanism, characteristic to SPS, cannot be overlooked.

8 Summary

To summarize, the dominant mechanism of densification in metallic glass powder is viscous flow. The kinetics of densification increases due to heating rate as a result of reduction of activation energy while the increase due to applied pressure is due to increase in effective pressure from the deformation of particles.

Chapter IV

Oxidation Behavior

1 Introduction

This chapter focuses on the morphology and structure of oxide growing on metallic glass powder. A combination of *ex-situ* and *in-situ* characterization techniques are integrated to predict the kinetics of isothermal oxidation in this powder. This is compared with experimental techqniues to establish the mechanism.

2 Powder morphology and structure

The morphology of the pristine $Fe_{48}Cr_{15}Mo_{14}Y_2C_{15}B_6$ metallic glass powder consists of particles of various shapes with the majority of them being spherical. The sizes of the particles were measured from several such SEM micrographs. More than 90% of the particles exhibit a diameter ranging from 20 µm to 60 µm with the mean diameter, D being 40 µm

The contents of this chapter are reproduced, with permission, from
1. T. Paul *et al.*, Scientific Reports, accepted (2018)

[141].

This chapter is aimed at investigating the oxidation behavior of this metallic glass powder within the supercooled liquid region of the material, without the occurrence of crystallization. Thus, in order to determine the temperatures of isothermal time dependent oxidation experiments, the thermal behavior of the material was examined first. The isochronal DSC trace of the metallic glass powder, measured at a heating rate of $50\,^{\circ}\mathrm{C\,min^{-1}}$, is presented in Fig. 25(a). It can be observed to exhibit a glass transition temperature T_g of about 570 °C and a crystallization onset temperature T_x of about 660 °C at this heating rate. Based on this thermogram, the temperatures of isothermal oxidation were determined to be 580 °C and 650 °C, completely within the glass transition and onset crystallization temperatures. Two more isochronal annealing experiments were conducted at the same heating rate, with the powder being heated up to 580 °C and 650 °C. The XRD spectra acquired from the powder in both pristine and annealed conditions are presented in Fig. 25(b). The absence of crystallization in all of these conditions is confirmed by the diffused peak in each spectra, characteristic of fully amorphous materials.

3 Oxide chemistry

The iron-rich section of the iron-oxygen phase diagram [2] is presented in Fig. 26. The temperatures of isothermal oxidation experiments employed in this investigation, 580 °C and 650 °C, are identified by red lines. At these temperatures, the oxides that are thermodynamically stable are FeO, Fe_2O_3 and Fe_3O_4. It is thus expected that the oxidation of this metallic glass powder would yield oxides among the aforementioned ones. The surface

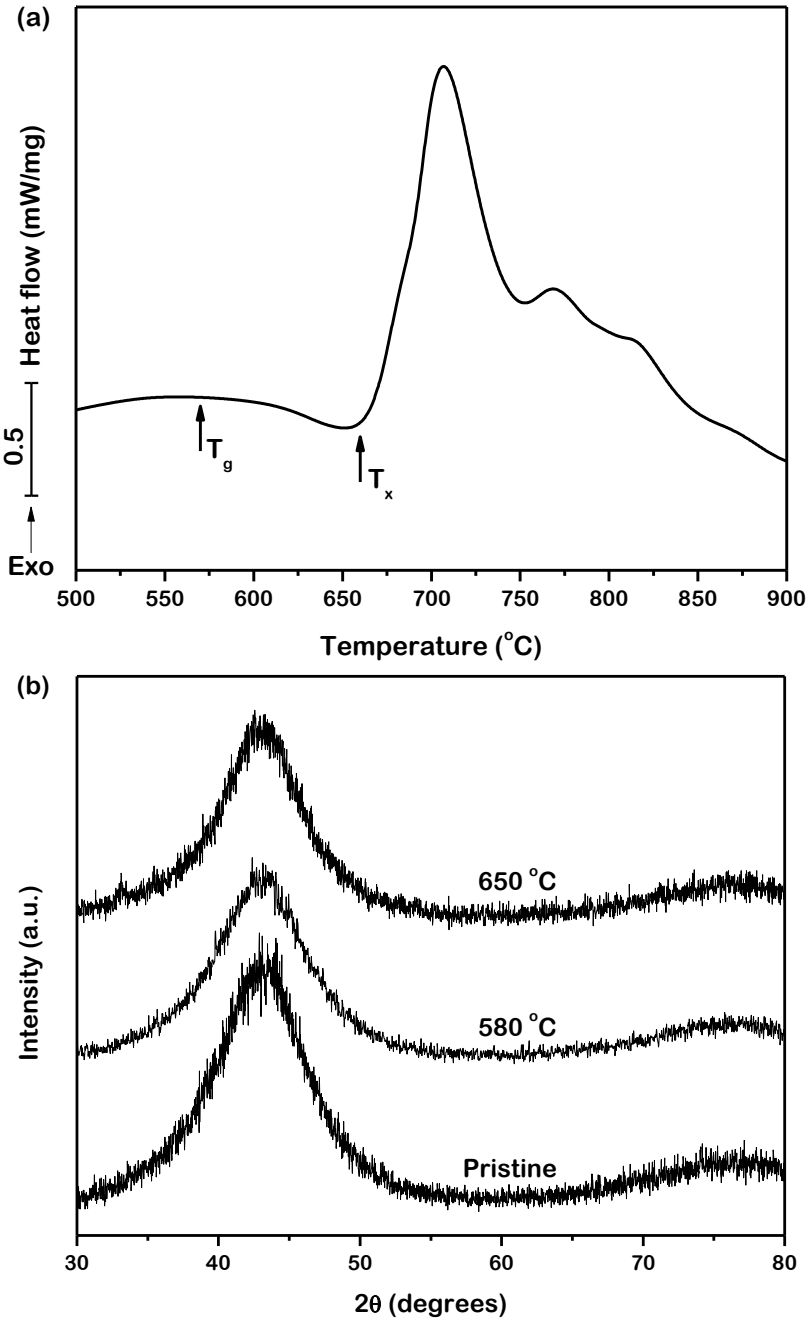

Figure 25: (a) Isochronal DSC trace of $Fe_{48}Cr_{15}Mo_{14}Y_2C_{15}B_6$ metallic glass powder measured at $50\,^{\circ}\mathrm{C\,min^{-1}}$. The glass transition and onset crystallization temperatures are 570 °C and 660 °C respectively. (b) XRD spectra of powder in pristine condition and annealed up to 580 °C and 650 °C confirms the amorphous structure

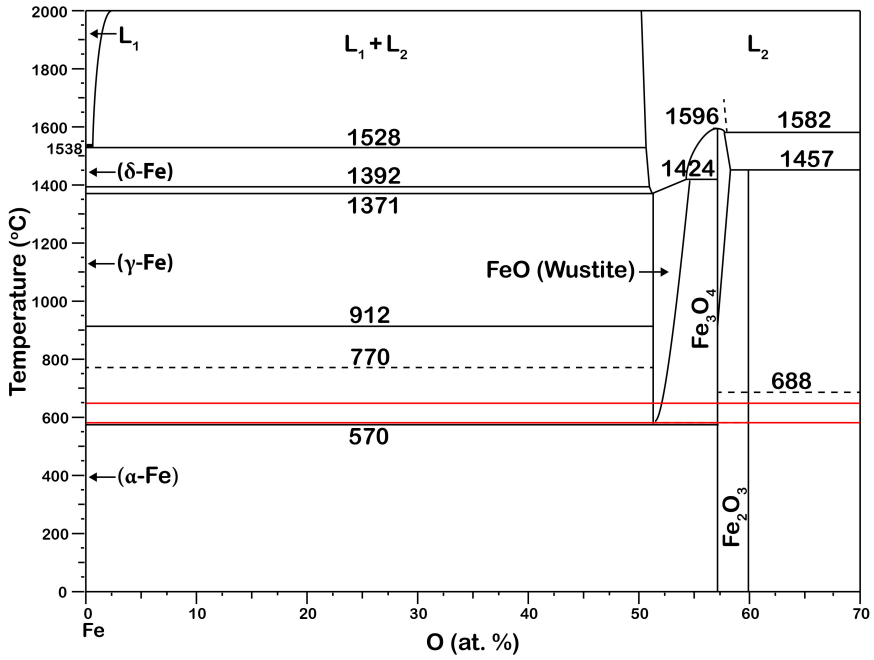

Figure 26: Section of iron-oxygen phase diagram (adapted from [2]). Growth of oxides is consistent with temperatures of isothermal oxidation, represented by red lines

of the pristine and oxidized metallic glass powder particles was examined by Raman spectroscopy. Spectra were acquired from multiple spots on individual particles among which, one, representative of the entire powder, is presented for each sample in Fig. 27. No Raman features are observed in the spectrum acquired from the pristine powder. This confirms that the surface of the pristine metallic glass powder is clean, devoid of any detectable oxides or other compounds on the metal surface. The spectra acquired from the surface of the powder oxidized at 580 °C and 650 °C for 120 min, each exhibit peaks that have been identified by their frequencies. The peaks at 226, 241, 295, 409, 501, 613 and 1317 cm^{-1} all correspond to Fe_2O_3 oxide [142, 143]. Only the peak at 663 cm^{-1} is assigned to Fe_3O_4 oxide [144]. A low intensity peak at 804 cm^{-1} is observed only for the sample oxidized at 650 °C for 120 min which is attributed to the formation of B_2O_3. This observation agrees with the literature that

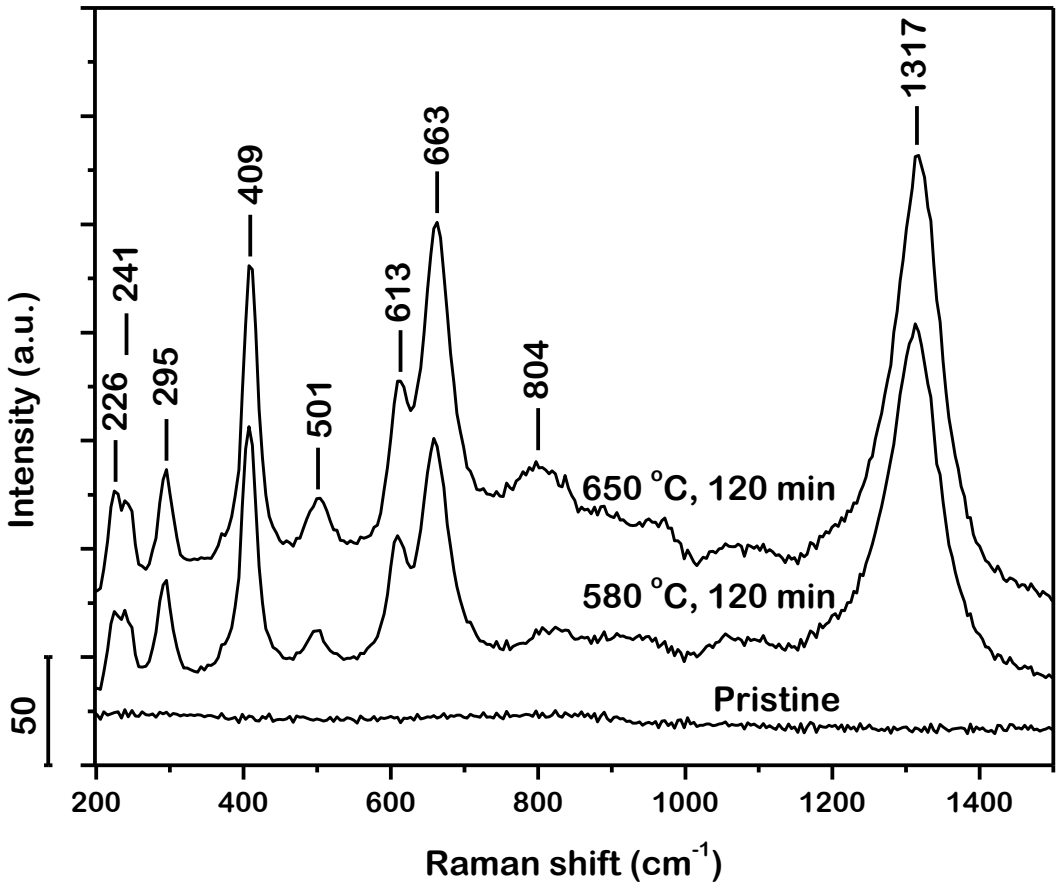

Figure 27: Representative Raman spectra acquired from surface of pristine and oxidized metallic glass powder particles. Surface of pristine powder particles is clean, devoid of detectable oxides. Oxidation at 580 °C and 650 °C results primarily in formation of Fe_2O_3 which grows as a uniform shell over the surface of the particles

boron is oxidized at a temperature higher than 600 °C [145]. B_2O_3 has also been observed upon oxidation of Fe-based metallic glasses containing boron [78, 77, 146, 147]. Thus it can be concluded that the oxide phases grow as a shell over the entire surface of the metallic glass powder particles. This is reasonable as the powder possesses a homogeneous amorphous structure and all sites on the surface are equally preferred for the growth of oxides. Additionally, according to the Raman spectra (Fig. 27), the major constituent of the oxide shell is Fe_2O_3.

Raman spectra acquired from the surface of the metallic glass powder isothermally oxidized for systematically increasing duration of time at 580 °C for 120, 240, 360, 480, 600 and 720 min and at 650 °C for 60, 120, 180, 240 and 300 min are presented in Fig. 28. The oxides are consistently observed to grow during the entire duration of isothermal oxidation at both temperatures. No noticeable peak shift is detected which suggests the uniformity of oxide growth with time, over the entire surface of the metallic glass powder particles.

With increasing time of isothermal oxidation, the volume of oxide shell growing on the surface of the powder is expected to increase, thereby resulting in an increase in intensity of the characteristic peaks in the Raman spectra. However, as presented in Fig. 28, the trend in intensity of the peaks are observed to be irregular at both temperatures. This irregularity in intensity of the peaks can possibly be an outcome of optical interference caused by multiple reflections of the incident laser in the oxide shell. The constructive or destructive interference, based on the thickness of the oxide shell regulates the intensity of the Raman-scattered radiation emitted to the far field. Indeed, oscillation of the intensities of the peaks in the Raman spectrum with thickness of oxide has been reported previously [148, 149]. Variation in the particle color was also observed, that is suggestive of the same.

Heating of sample due to interaction with laser is frequently encountered in Raman spectroscopy [150]. It may result in artifacts, such as oxidation of sample and temperature-induced peak shifts. In the present investigation, the absence of Raman peaks in the spectrum acquired from the surface of the pristine metallic glass powder particles suggests that no oxides are formed during excitation where the laser power is optimized to 3 mW for high-

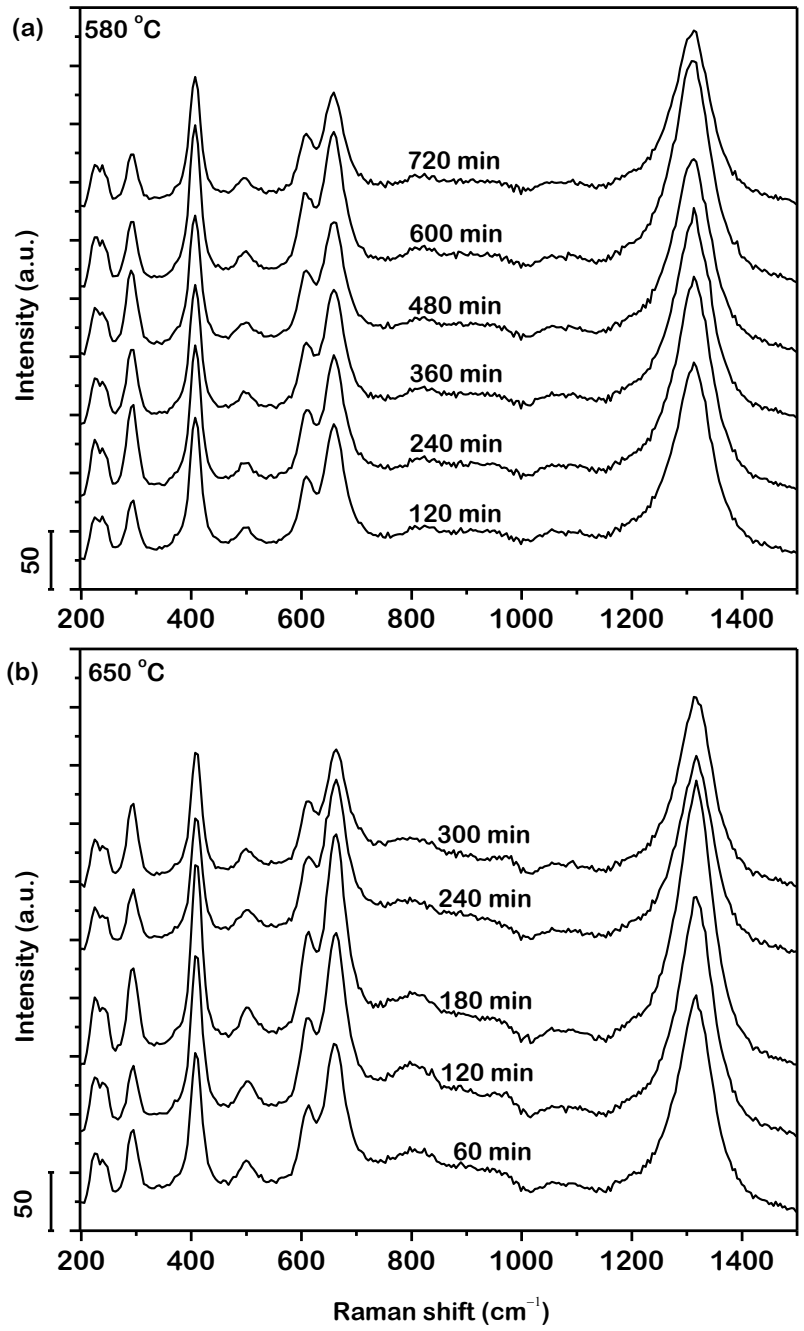

Figure 28: Raman spectra acquired from the surface of the metallic glass powder isothermally oxidized at (a) 580 °C for 720 min and (b) 650 °C for 300 min. Oxide grows as a uniform shell consistently over the surface of the powder particles. Irregularity in intensity of peaks with increasing time of isothermal oxidation is a possible outcome of optical interference due to multiple reflections of incident laser in oxide shell

est signal counts without artifacts. On the other hand, oxidation of the powder was clearly observed when the laser power was increased to 4 mW (not shown here). Hence the presence of laser heating during the acquisition of Raman spectra was anticipated, although it was not high enough to drive oxidation. To this end, the laser-induced rise in temperature of the sample was estimated from the anti-Stokes-to-Stokes intensity ratio, I_{aS}/I_S, which is approximately the Boltzmann factor [151, 152]. Fig. 29 presents the Raman spectrum acquired from the surface of the powder oxidized at 580 °C for 720 min with an incident laser power of 3 mW. The most intense anti-Stokes peak, being at $-409\,cm^{-1}$, was used for calculation of temperature. I_{aS}/I_S is found to be 0.342 after background subtraction (inset, Fig. 29). Hence, the temperature is estimated to be 278 °C, which is too low to induce oxidation. Similarly, the temperature is estimated to be 152 °C for an incident laser power of 1 mW where the corresponding Raman mode was observed at $410.5\,cm^{-1}$. Accordingly, by linear extrapolation, the peak is estimated to be at $412\,cm^{-1}$ at room temperature. Therefore, the acquisitions of Raman spectra in this investigation were not subject to significant spectral shifts due to laser heating and the assignments of the peaks are thus accurate.

4 Oxide structure

In order to further analyze the oxidation behavior of the metallic glass powder particles, the structure of the oxides was investigated by X-ray diffraction. The XRD spectra acquired from the metallic glass powder isothermally oxidized at 580 °C for 720 min and at 650 °C for 300 min are presented in Fig. 47. In addition to the diffused peak as in the pristine powder, these spectra exhibit sharper peaks, superimposed on the amorphous background.

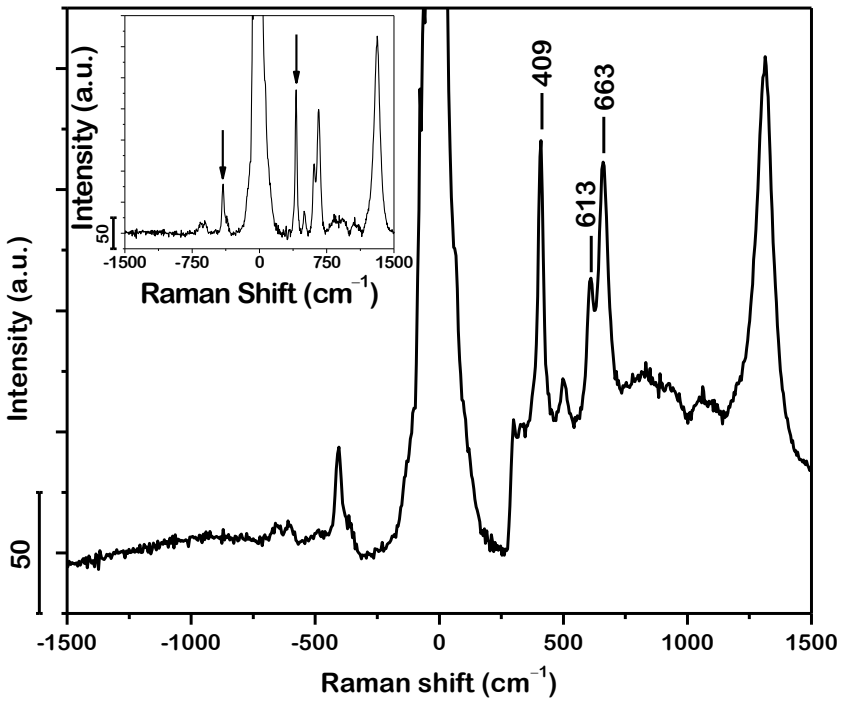

Figure 29: Estimation of laser-induced rise in temperature of sample from anti-Stokes-to-Stokes intensity ratio of peak at 409 cm^{-1} in Raman spectrum acquired from surface of powder oxidized at 580 °C for 720 min. *Inset* represents same spectrum after background subtraction. Temperature rise with incident laser power of 3 mW is computed to be 278 °C, too low to induce oxidation

These peaks are identified to be Fe_2O_3 and Fe_3O_4 oxides. No peaks corresponding to B_2O_3 were observed in the XRD spectra owing to the minor amount formed as exhibited by the Raman spectra. The XRD spectra thus confirm the results obtained from Raman spectroscopy. During isothermal oxidation at the lower temperature of 580 °C for shorter duration of time up to 240 min the volume of the oxide shell is possibly too low to be detectable in the XRD spectra. This is also observed during isothermal oxidation at 650 °C for the shortest duration of time of 60 min. With an increase in duration of time of isothermal oxidation at both temperatures, the intensity of the characteristic peaks gradually increase, that suggests an increase in the volume of the oxide shell growing on the surface of the powder.

Hence from the Raman and XRD spectra it can be concluded that the growth of oxides on the surface of the metallic glass powder has a hierarchical structure. First, the growth occurs as a shell over the entire surface of the powder. Second, this oxide shell is polycrystalline, or in other words, constitutes of multiple oxide grains. However, both Raman and XRD spectra are incapable of providing quantitative information on the trend in volume of oxides formed as a function of time during isothermal oxidation.

5 USAXS interpretation of hierarchical oxide structure

In order to enumerate the isothermal evolution of oxide in this metallic glass powder, *in-situ* ultra-small angle X-ray scattering (USAXS) was employed. The number of particles subjected to exposure in the beam is of the order of thousand and hence is representative of the entire sample of powder. The USAXS intensity, I(Q) acquired from the pristine metallic glass powder at ambient temperature over a scattering vector, Q-range of $0.0005\,\text{Å}^{-1}$ to

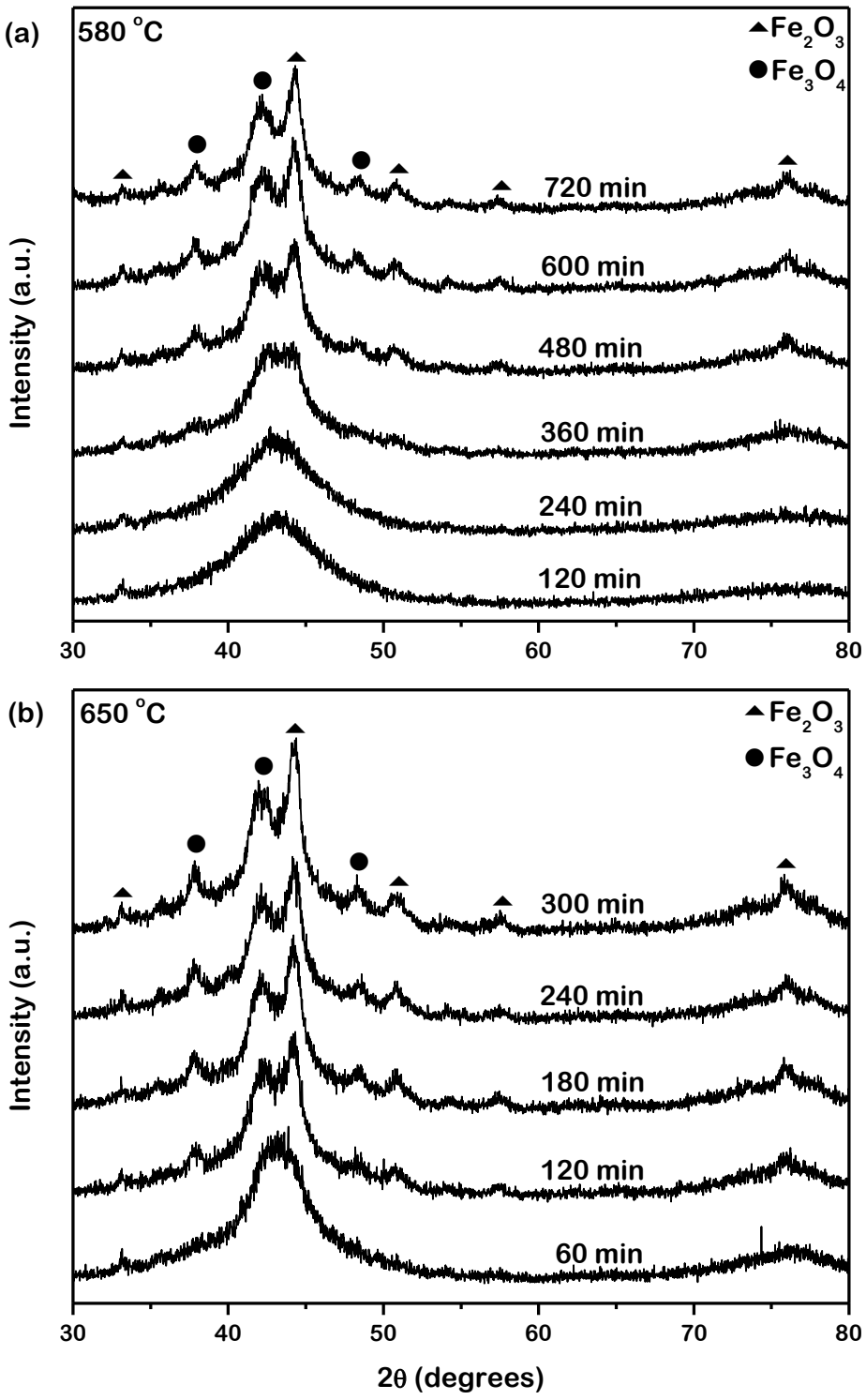

Figure 30: XRD spectra acquired from metallic glass powder isothermally oxidized at (a) 580 °C for 720 min and (b) 650 °C for 300 min. Oxide shell is confirmed to be polycrystalline, consisting of multiple grains

$0.2\,\text{Å}^{-1}$ is presented in a log-log plot in Fig. 31. This powder consists of non-interacting, mostly spherical particles with an average diameter, D of about 40 µm which yields D^{-1} of $0.000\,002\,5\,\text{Å}^{-1}$. In accord with the expected Q-dependence for a dilute solution of identical uniform spheres at $Q \gg D^{-1}$, the scattering intensity can be observed to decay following a power-law as Q^{-4} [153]. This confirms that the powder consists of particles with a smooth surface devoid of any structural features as shown by the Raman and XRD spectra. Over the Q-range above $0.1\,\text{Å}^{-1}$, a constant, low-intensity background arising from the detector and environment is observed, which is independent of Q and not related to the morphology and structure of the powder particles and the oxides formed on their surface.

The evolution of oxides during *in-situ* isothermal time dependent experiments is manifested by the USAXS intensity distributions acquired at 580 °C for 720 min and 650 °C for 300 min as presented in Fig. 32. The intensities are calibrated on relative scale as the motivation of the present investigation is to enumerate the average volume of oxide shell formed on the particles [154]. Based on the intensity, I(Q) measured as a function of the scattering vector, Q, the characteristics of scattering, corresponding interpretation as representative of the hierarchical structure of the oxide over decreasing length scales and their evolution with increase in time during isothermal oxidation are discussed across four discrete Q-ranges as follows.

First, over the Q-range from $0.0005\,\text{Å}^{-1}$ to $0.002\,\text{Å}^{-1}$, scattering results from the oxidized particles. The average diameter of the particles, 40 µm is at a length scale larger than that resolved in the present USAXS measurements. It is clearly observed that with

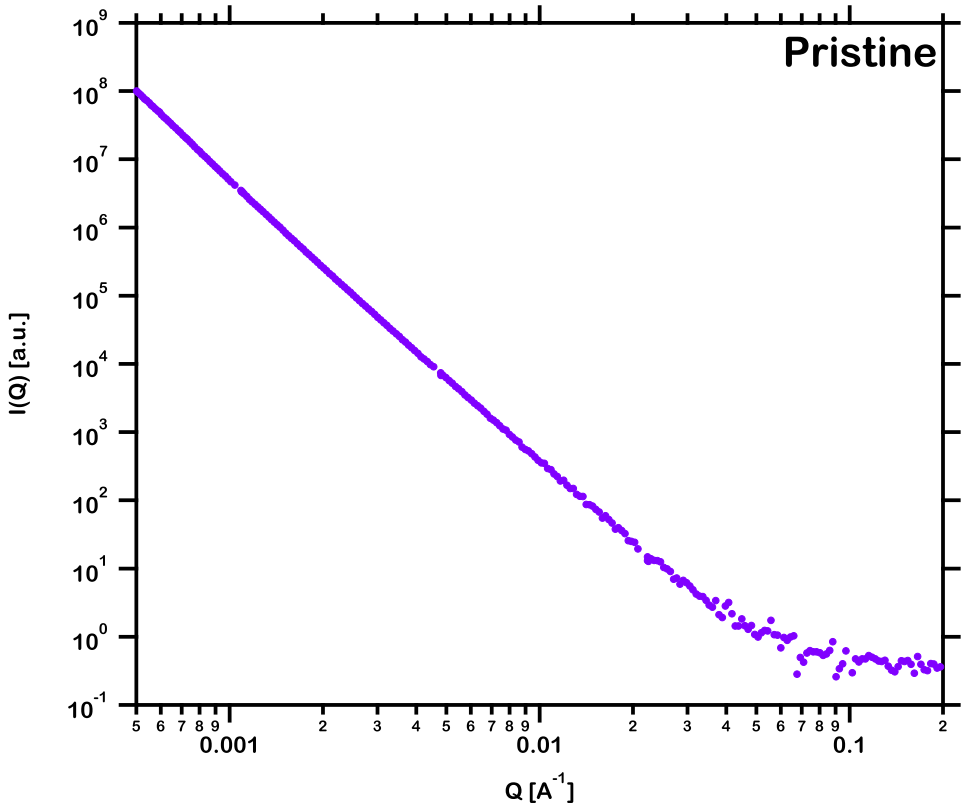

Figure 31: Log-log plot of USAXS intensity, I(Q) acquired from the pristine metallic glass powder at ambient temperature, over a scattering vector, Q-range of 0.0005 Å^{-1} to 0.2 Å^{-1}. Scattering intensity decays following a power-law as Q^{-4} in accordance with that for a dilute solution of identical spheres of mean diameter D at $Q \gg D^{-1}$

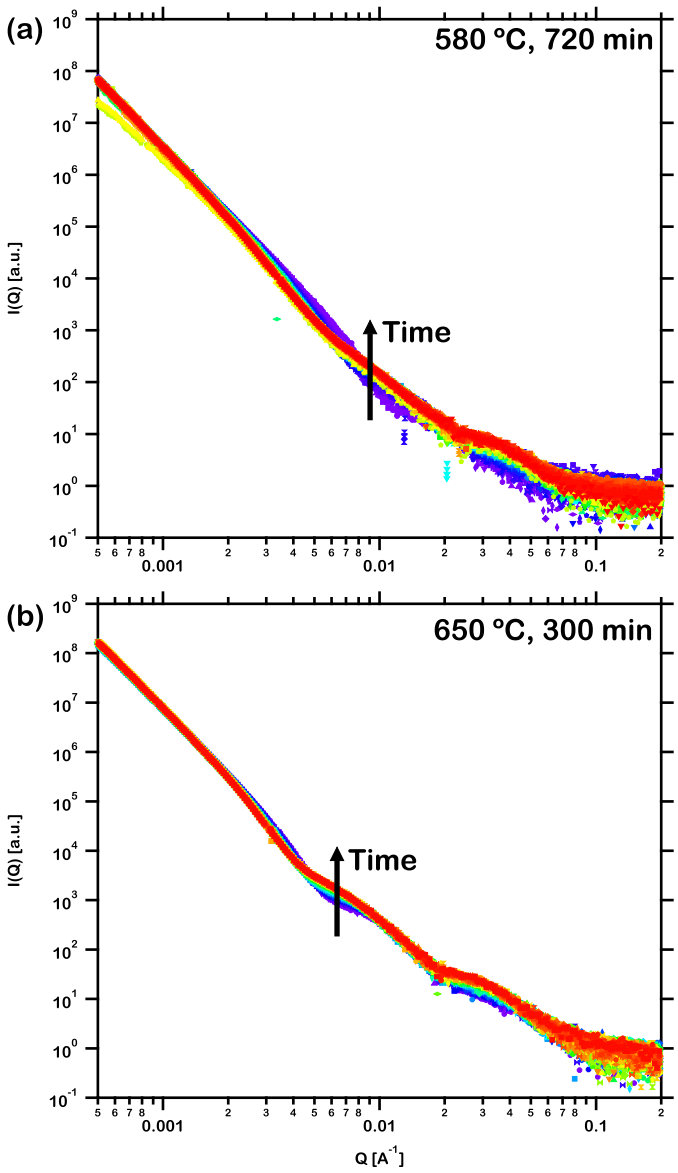

Figure 32: USAXS intensity distributions acquired *in-situ* from powder during isothermal oxidation at (a) 580 °C for 720 min and (b) 650 °C for 300 min. Duration between two consecutive measurements is approximately 3 min

increase in time of *in-situ* isothermal experiments, the size of the particles themselves do not change appreciably, as evidenced by the intensity distributions at both temperatures. As a result, I(Q) continues to decay following the power-law as Q^{-4}, identical to that presented for the particles at room temperature (Fig. 31).

Second, over the Q-range from $0.002\,\text{Å}^{-1}$ to $0.02\,\text{Å}^{-1}$, scattering results from the Fe_2O_3 oxide that grows as a uniform shell over the entire surface of the metallic glass powder particles. The length scale of the oxide shell can be estimated from this Q-range to be approximately between few tens to few hundreds of nanometres. As a result, the oxidized metallic glass powder exhibits a core-shell structure with the powder particle behaving as the core and the oxide behaving as the shell. A form factor is produced due to the difference in X-ray scattering contrasts of the core and the shell. In such a form factor the characteristic Fourier-Bessel oscillations [155], as observed in the intensity distributions, convey quantitative information on the thickness of the oxide shell. During *in-situ* isothermal oxidation at both temperatures, with increase in time these oscillations shift towards lower Q, suggesting a corresponding increase in thickness of the oxide shell.

Third, over the Q-range from $0.02\,\text{Å}^{-1}$ to $0.1\,\text{Å}^{-1}$, scattering occurs due to the multiple grains in the polycrystalline oxide shell. The length scale of the oxide grains can be computed from this Q-range to be approximately between few to few tens of nanometres. The intensity distributions in this Q-range exhibit the well-recognized Guinier 'knee' that is characteristic of the radius of gyration of the grains [156] followed by the Porod power-law slope. With increase in time during isothermal oxidation, small nuclei of oxides are formed while pre-

existing grains grow into larger ones. Thus the evolution of sizes of the grains has an irregular trend and consequently the variation in intensity distribution is less conspicuous.

Finally, over the Q-range from $0.1\,\text{Å}^{-1}$ to $0.2\,\text{Å}^{-1}$, a constant background scattering is manifested. This originates from the instrument and environment, without any dependence on Q. This is confirmed by the fact that the measured intensities are significantly lower at this Q-range and does not evolve with time of isothermal oxidation at both temperatures.

In summary, the evolution of the hierarchical structure of the metallic glass powder with time during isothermal oxidation at both 580 °C and 650 °C across decreasing length scales is based on a powder core over which an oxide grows as a uniform shell which further consists of multiple grains. This hierarchical structure is utilized to construct a physical model under the aegis of which the fitting of parameters enables the quantitative analysis of oxidation in this material as described in the following section.

6 USAXS quantitative modelling

The physical model representing the hierarchical structure is depicted by a schematic in Fig. 33. At large length scale (small Q), scattering is representative of the ensemble of a large number of non-interacting oxidized particles (Fig. 33a). With further decrease in length scale (medium Q) individual oxidized particles with distinct powder core and oxide shell can be distinguished (Fig. 33b). A section is made to clarify the internal structure. At small length scale (large Q), the scatterers are the multiple grains in the oxide shell (Fig. 33c).

In order to achieve consistency with the physical characteristics three components are

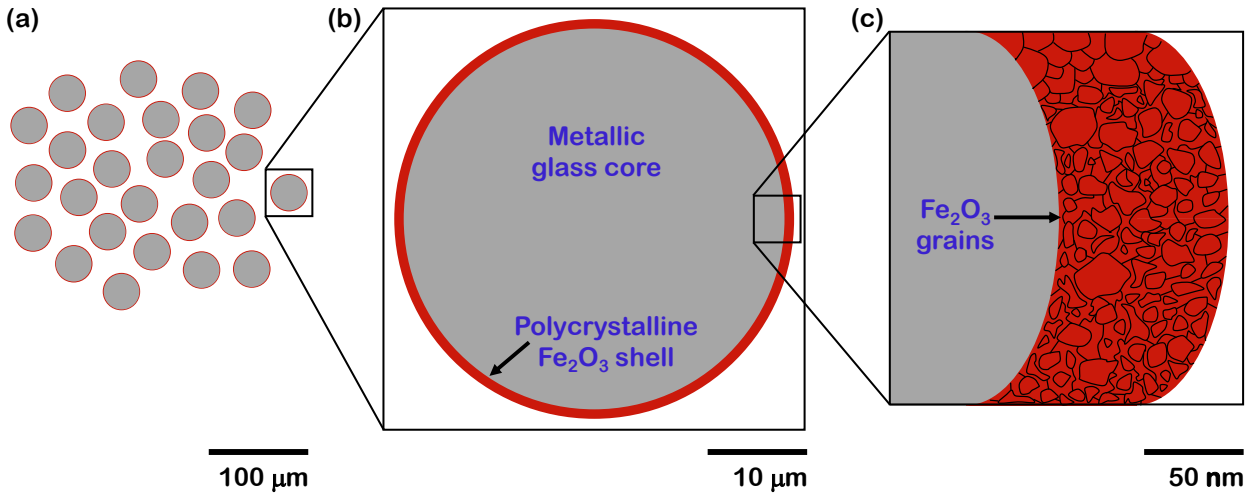

Figure 33: Schematic physical model representing hierarchical structure over decreasing length scales used for USAXS quantitative modelling. It consists of cross sections of (a) ensemble of non-interacting oxidized particles, (b) individual particles with powder core and oxide shell, and (c) multiple grains within the oxide shell

utilized to construct the scattering model. In the first component, the mean diameter was fixed at 40 µm. The standard deviation was obtained from fitting the scattering intensity acquired from the pristine powder at room temperature. This was kept constant thereafter. The X-ray scattering length densities of the $Fe_{48}Cr_{15}Mo_{14}Y_2C_{15}B_6$ core and Fe_2O_3 shell were computed to be $60.24 \times 10^{10}\,cm^{-2}$ and $42.32 \times 10^{10}\,cm^{-2}$ respectively while that of air as solvent was kept zero. It is to be noted here that while the major constituent of the oxide shell is Fe_2O_3, both Raman and XRD spectra detected the presence of Fe_3O_4 as well. However, the X-ray scattering length density of Fe_3O_4, $41.68 \times 10^{10}\,cm^{-2}$, is almost equal to that of Fe_2O_3. Hence, in relevance to USAXS, these oxides are similar and thus the thickness estimated from the intensity distributions are also accurate. In the second component, the Porod power-law slope was fixed at -4 and the radius of gyration was fitted.

The third component accounted for the background which was set to a constant value at the beginning of the fitting routine. Fig. 50 presents the result of a representative fitting routine performed on the USAXS intensity acquired from the metallic glass powder oxidized at 650 °C for 300 min. The model can be observed to be in good agreement with the measured USAXS intensity. The small misfit results from the fact that the present model is utilized to estimate a single value of the thickness of the oxide shell growing over all the particles. In practice, however, in a distribution of diameters of the powder cores with a mean and standard deviation, the thickness of the oxide shell is not constant and is dependent on the diameter of the individual particles. Thus, although the model underestimates the thickness of the oxide shell and hence the USAXS intensity near the Q-range of the misfit, the overall concurrence yields a good estimate of the oxide shell thickness. This fitting routine is employed to all the USAXS intensity distributions measured during isothermal oxidation at 580 °C for 720 min and 650 °C for 300 min. The evolution of thickness of the oxide shell over time during isothermal oxidation is presented in Fig. 35. It is observed that at both temperatures the increase in oxide shell thickness is rapid at the initial stage and gradually slows down.

7 Quantitative validation of oxide evolution

In order to examine the accuracy of the quantitative analysis by USAXS, the gain in mass of the powder due to isothermal oxidation, per unit mass of powder was theoretically estimated. Three assumptions were made for this theoretical computation. First, all the particles of this metallic glass powder can be represented by solid spheres of identical diam-

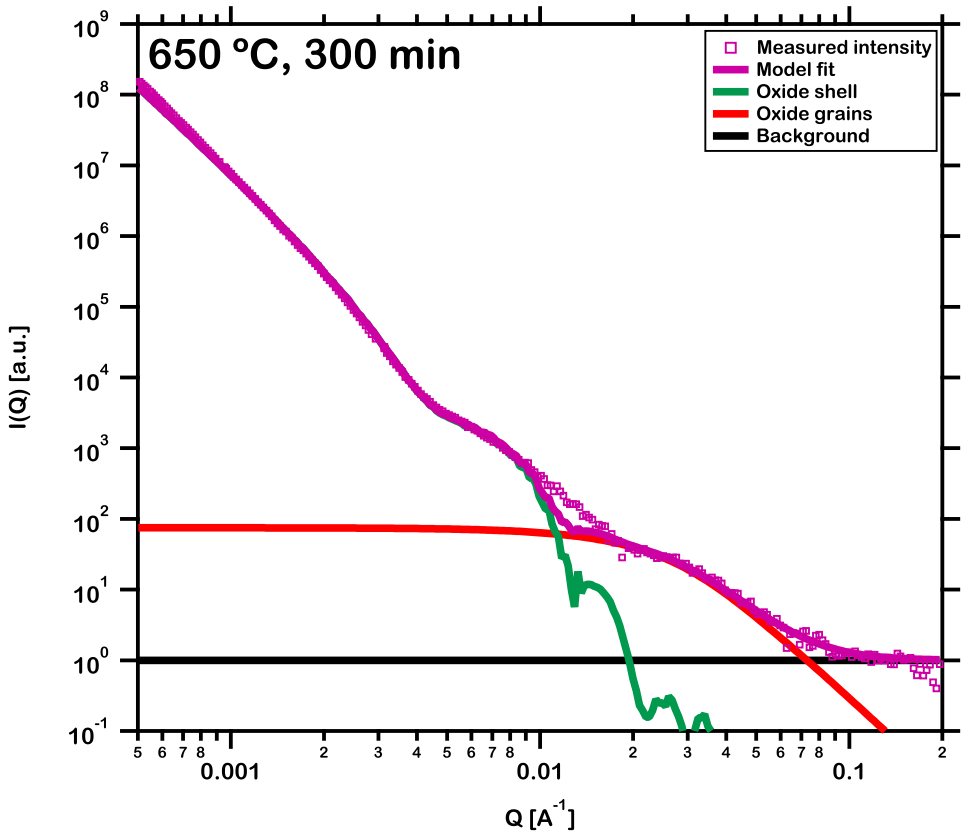

Figure 34: Illustration of representative fitting routine performed on the USAXS intensity acquired from the powder oxidized at 650 °C for 300 min utilizing the three components of the scattering model, the oxide shell, grains in the shell and a constant background. Small misfit results from the distribution in the diameter of the particles and hence of the thickness of the oxide shell

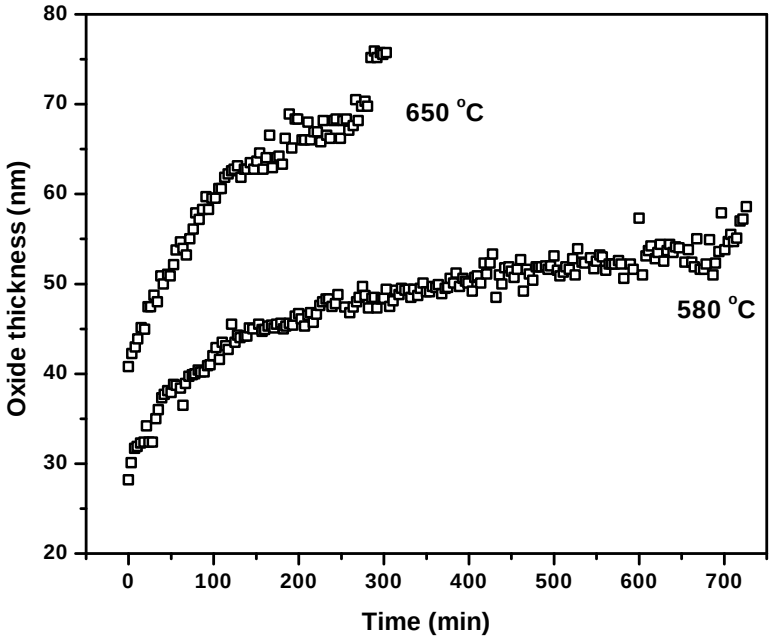

Figure 35: Evolution of thickness of oxide shell over time estimated from USAXS intensity distributions acquired *in-situ* during isothermal oxidation of powder at 580 °C for 720 min and 650 min

eter equal to 40 µm. Second, oxidation of the particles result in the formation of only one oxide, Fe_2O_3. Third, the thickness of oxide formed on each particle is equal. Based on these assumptions, the initial mass of a single powder particle was calculated from its diameter and density ($7500\,kg\,m^{-3}$) [51]. The mass of oxide was calculated from its thickness and density ($5240\,kg\,m^{-3}$). The percentage gain in mass was estimated by dividing the mass of oxide formed on a single particle by the mass of that particle. The results from this theoretical estimation was compared with the gain in mass measured *in-situ* during isothermal oxidation by a thermogravimetric analyzer. This is presented in Fig. 36 for the temperatures 580 °C and 650 °C. It is observed that the theoretically estimated gain in mass continuously underestimates that actually measured in practice. This can be explained on the basis of the assumptions and the mechanism of oxidation. The isothermal oxidation investigated here is controlled by diffusion at the surface with the rate being dependent on the surface area of the powder particles. For a given volume, the surface area is least for a sphere. This theoretical calculation performed assuming all particles hence estimates a lower gain in mass. In practice, non-spherical particles oxidize to yield a higher gain in mass that is measured by the thermogravimetric analyzer as observed in Fig. 36.

8 Summary

In summary, upon oxidation, iron-based metallic glass powder grows a layer of Fe_2O_3 which is crystalline. USAXS estimation comparatively underestimates the experimentally measured kinetics of isothermal oxidation due to the variation of particle size.

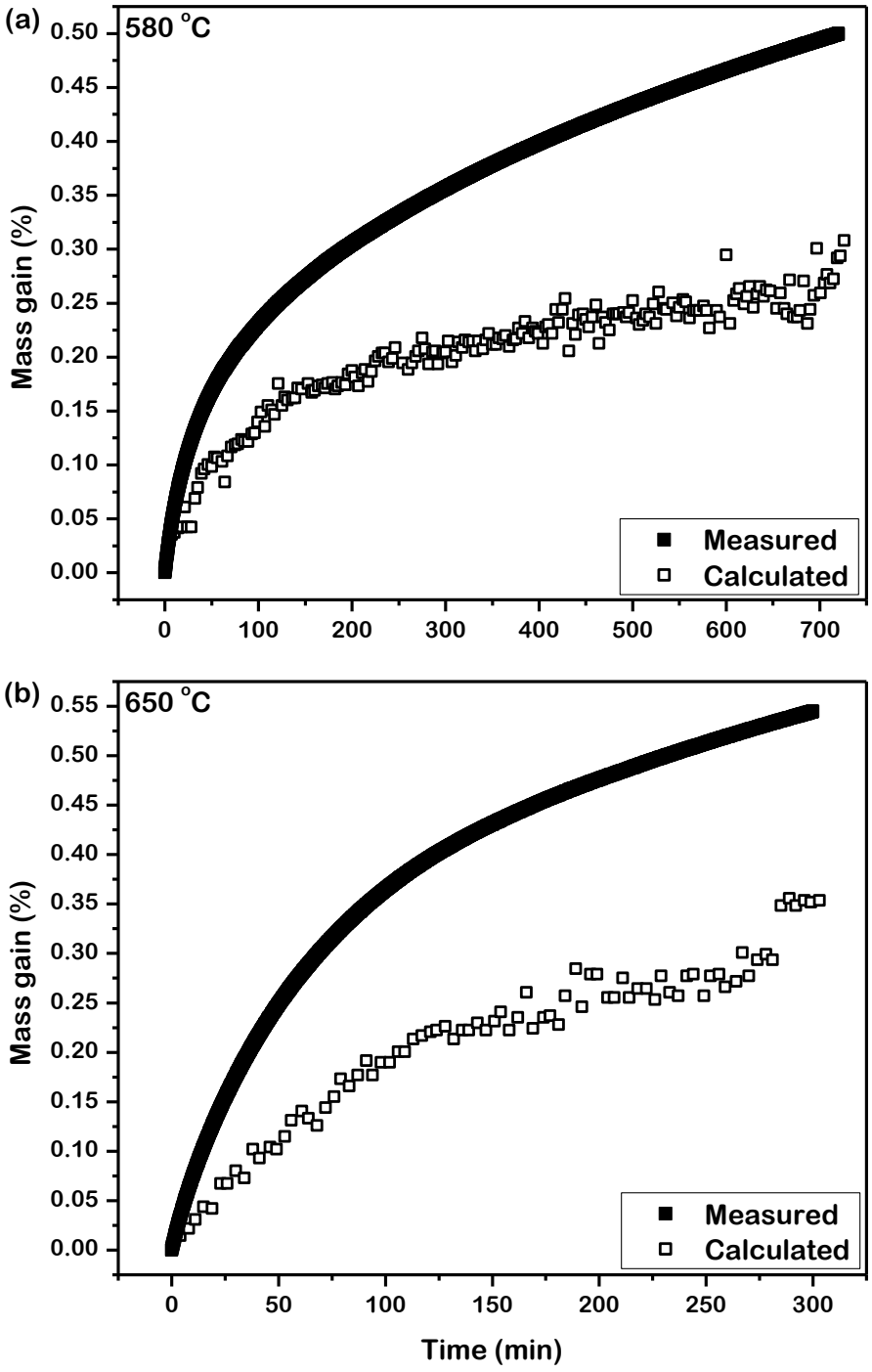

Figure 36: Comparison of the theoretically estimated gain in mass with that measured in practice during isothermal oxidation of powder at (a) 580 °C for 720 min and (b) 650 °C for 300 min. In practice, non-spherical particles oxidize to yield higher gain in mass than that computed from the scattering model

Chapter V

Crystallization Kinetics

1 Introduction

This chapter focuses on the mechanism and kinetics of crystallization in this iron-based metallic glass powder. The crystalline phases resulting from thermal transformations are identified along with their kinetics of evolution upon isochronal annealing.

2 Nanocrystallization in $Fe_{48}Cr_{15}Mo_{14}Y_2C_{15}B_6$ metallic glass

Transmission electron microscope images of $Fe_{48}Cr_{15}Mo_{14}Y_2C_{15}B_6$ metallic glass powder sintered at 630 °C is presented in Fig. 37. The regions of darker contrast suggest that the nanocrystals are distributed throughout the sintered sample. In order to obtain a more clarified micrograph of a single nanocrystal, the TEM image was acquired at higher mag-

The contents of this chapter are written based on results published in
1. T. Paul *et al.*, Journal of Alloys and Compounds 753 (2018) 679 - 687
2. T. Paul *et al.*, Advanced Engineering Materials 19 (2017) 1700224
3. T. Paul *et al.*, Journal of Alloys and Compounds, submitted (2019)

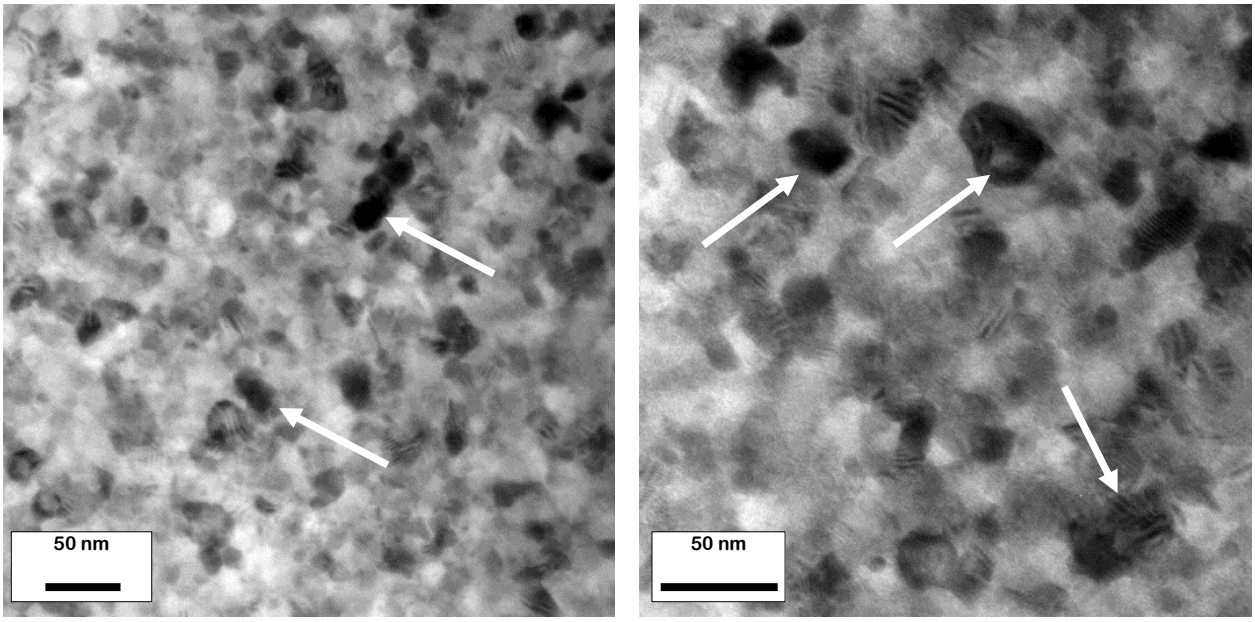

Figure 37: Representative transmission electron micrographs of $Fe_{48}Cr_{15}Mo_{14}Y_2C_{15}B_6$ metallic glass powder SP sintered at 630 °C. Regions of darker contrast shows that nanocrystals are distributed throughout the sample

nification for a nanocrystal evolved in sample sintered at a higher temperature of 800 °C as presented in Fig. 38. It can be observed that the volume fraction and size distribution of the crystals are dependent on the temperature of sintering. In order to understand the effect to processing parameters on the crystallization of sintered compacts, it is necessary to understand the mechanism of crystallization in pristine $Fe_{48}Cr_{15}Mo_{14}Y_2C_{15}B_6$ metallic glass powder.

3 Crystallization in pristine $Fe_{48}Cr_{15}Mo_{14}Y_2C_{15}B_6$ metallic glass powder

3.1 Thermal analysis

The isochronal DSC traces of the Fe-based amorphous alloy measured at the heating rates, c, of 0.17, 0.33, 0.50 and 0.67 $K\,s^{-1}$ are presented in Fig. 39. The exothermic heat

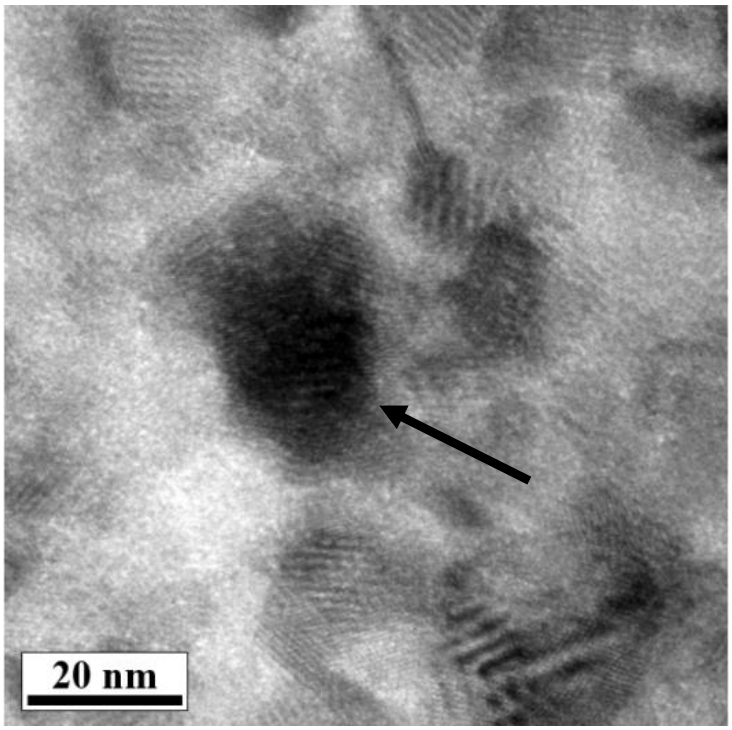

Figure 38: Representative transmission electron micrograph of $Fe_{48}Cr_{15}Mo_{14}Y_2C_{15}B_6$ metallic glass powder SP sintered at 800 °C

flow below 900 K is associated with structural relaxation and glass transition widely observed in Fe-based amorphous alloys including the one employed in this study [157, 112]. This, however, is beyond the scope of the present investigation on the isochronal crystallization behavior and is not discussed. The crystallization process can be observed to extend over a temperature range of about 200 K. Additionally, with an increase in heating rate, the onset of crystallization shifts progressively to higher temperatures. The increase in the onset crystallization temperature, T_o (K) identified in the present work, are consistent with those reported at various heating rates as presented in Table 4.

The crystallization process in this amorphous alloy can be observed to comprise of multiple exothermic transformations at all heating rates (Fig. 39). The overlapping exother-

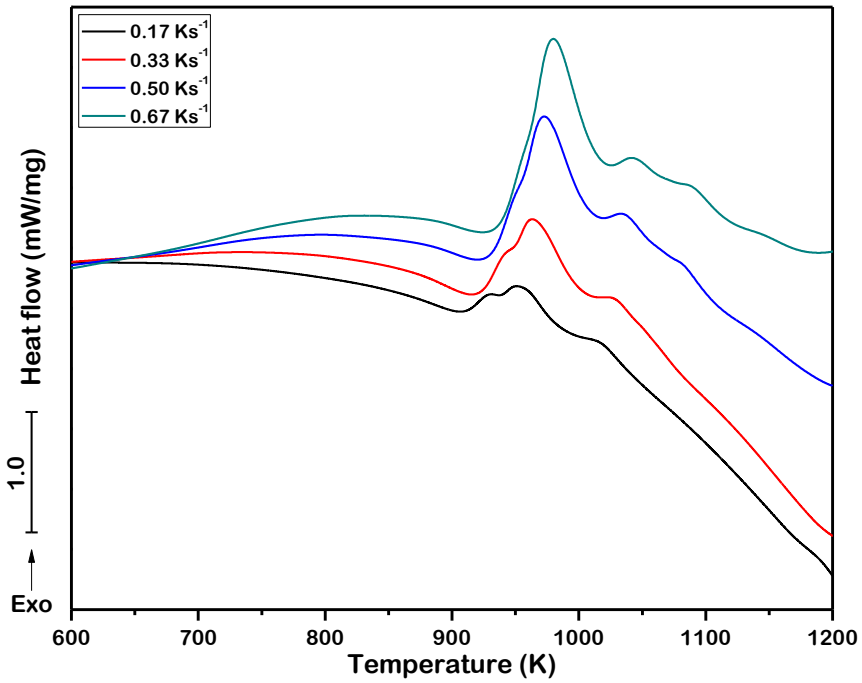

Figure 39: Isochronal differential scanning calorimetric traces of $Fe_{48}Cr_{15}Mo_{14}Y_2C_{15}B_6$ metallic glass powder at different heating rates

mic peaks indicate that a crystalline transformation initiated before the conclusion of the preceding one. The peaks also exhibited a strong kinetic effect as evidenced by the continuous escalation of heat flow with increasing heating rate from 0.17 to 0.67 $\mathrm{K\,s^{-1}}$, thereby justifying the analysis of the thermal characteristics of the constituent peaks. However, the observed overlap significantly impedes the identification of the characteristic temperatures of the exothermic transformations. In order to circumvent this problem, deconvolution was performed to distinctly separate the overlapping peaks. It has been reported [158] that Gaussian regression is the appropriate method of deconvolution of overlapping peaks in DSC traces of amorphous alloys and was thus applied to study the individual transformations in the present study.

The deconvolution of the DSC traces at all heating rates is presented in Fig. 40 which

Table 4: Onset crystallization temperature of $Fe_{48}Cr_{15}Mo_{14}Y_2C_{15}B_6$ metallic glass at different heating rates

c ($K\,s^{-1}$)	$\mathbf{T_o}$ (K)	**Ref.**
0.13	900	[159]
0.17	895	[160]
	904	[97]
	907	Present work
0.33	886	[52]
	926	[161]
	916	Present work
0.50	920	Present work
0.67	920	[125]
	924	Present work

exhibits an excellent agreement between the measured heat flow and the fitted curves. The overall crystallization process can be observed to comprise of 4 distinct exothermic transformations which are henceforth designated as Exo 1, Exo 2, Exo 3 and Exo 4. This enables a convenient identification of the characteristic peak crystallization temperature, T_p (K) of the transformations at the employed heating rates and the results are presented in Table 5. Subsequent to deconvolution it was observed that the enthalpy of the exothermic transformations varied with the heating rate. In particular, the enthalpy of Exo 4 at $0.17\,K\,s^{-1}$ was extremely low so as to be indistinguishable as compared to the others and the corresponding T_p is thus not reported here. Due to the possibility of error in estimation of parameters resulting from absence of data points, Exo 4 was not conducive for further analysis and is not discussed hereafter. The progressive increment in T_p for Exo 1, Exo 2 and Exo 3 with

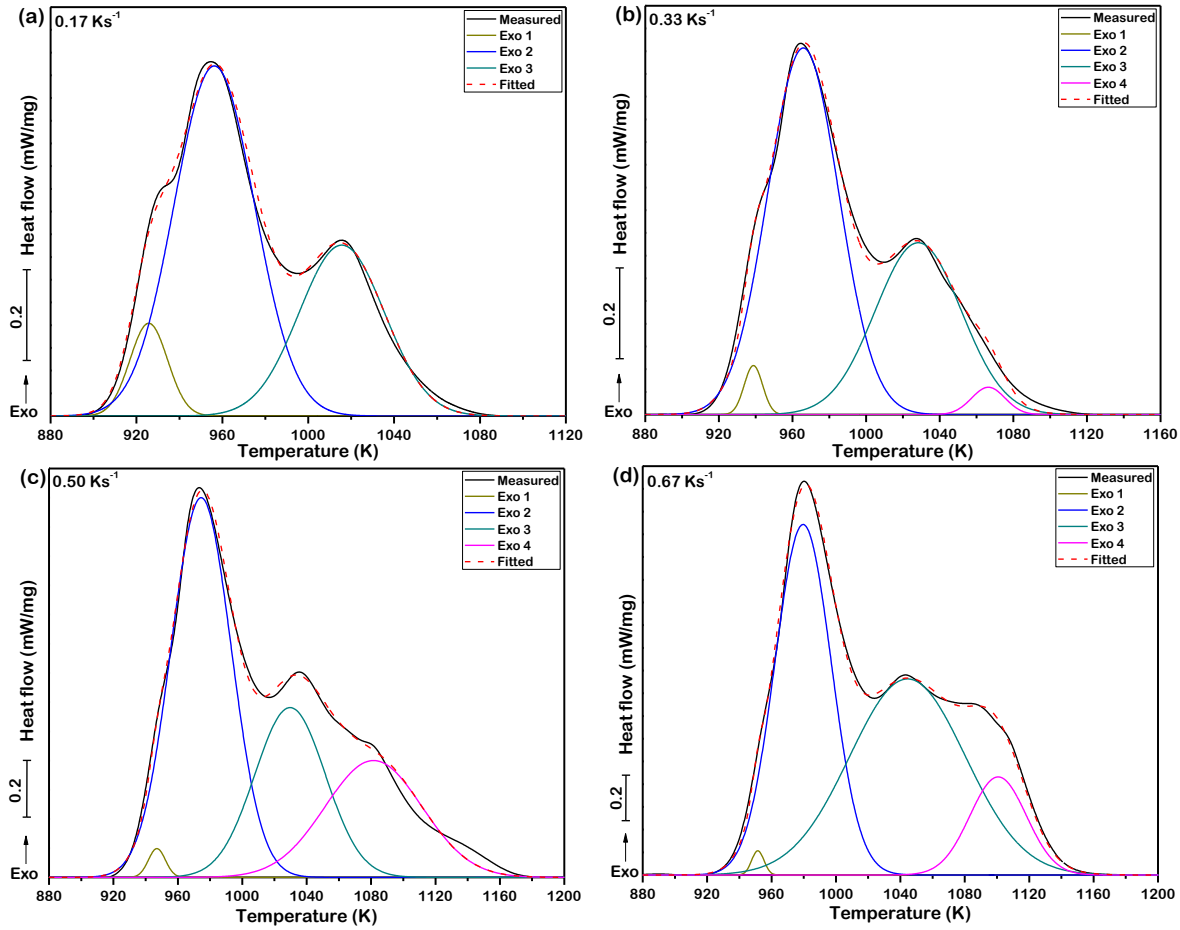

Figure 40: Deconvolution of overlapping peaks in isochronal differential scanning calorimetric traces of $Fe_{48}Cr_{15}Mo_{14}Y_2C_{15}B_6$ metallic glass powder at (a) $0.17\,K\,s^{-1}$, (b) $0.33\,K\,s^{-1}$, (c) $0.50\,K\,s^{-1}$ and (d) $0.67\,K\,s^{-1}$

increasing heating rate, as observed in Table 5, confirms the kinetic effect noted earlier and was investigated by an estimation of the activation energy of crystallization.

3.2 Kinetics of crystallization

The kinetic effect was analyzed following an estimation of the apparent activation energy of crystallization, E_p ($J\,mol^{-1}$) according to the Kissinger equation, expressed as [162, 163]:

Table 5: Peak crystallization temperatures of $Fe_{48}Cr_{15}Mo_{14}Y_2C_{15}B_6$ metallic glass at different heating rates (values in parenthesis indicate indetermination from the utilization of Gaussian function)

c ($K\,s^{-1}$)	**T_p** (K)			
	Exo 1	**Exo 2**	**Exo 3**	**Exo 4**
0.17	925.72(8.57)	956.29(1.65)	1015.64(0.26)	-
0.33	938.82(8.57)	965.88(1.48)	1022.28(5.00)	1066.39(5.11)
0.50	947.05(5.63)	974.38(1.23)	1029.72(5.98)	1081.54(5.18)
0.67	951.40(9.33)	979.57(0.66)	1044.36(0.98)	1100.73(15.35)

$$\ln\left(\frac{T_p^2}{c}\right) = \frac{E_p}{RT_p} + constant \tag{V.1}$$

where R ($8.314\,J\,K^{-1}\,mol^{-1}$) is the universal gas constant. The parameter $\ln(T_p^2/c)$ plotted with respect to $1/T_p$ exhibits a linear relationship as presented in Fig. 41. The apparent activation energy of crystallization E_{p1}, E_{p2} and E_{p3} were estimated from the slopes according to Eq. V.1 to be 369 ± 14, 437 ± 23 and 406 ± 101 $kJ\,mol^{-1}$, respectively. Thus among these three transformations the energy barrier is lowest for Exo 1 while it is highest for Exo 2, or in other words, the occurrence of Exo 1 crystallization is easiest while that of Exo 2 is the most difficult. In order to extend this qualitative analysis to a fundamental quantitative understanding of the mechanism of crystallization, the crystallized fraction during the transformations were studied as described in the following sections.

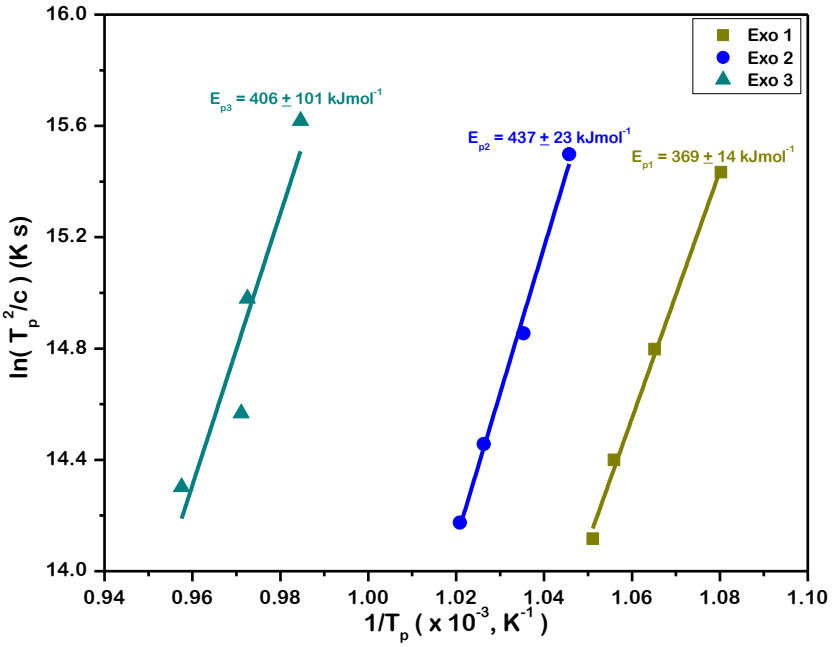

Figure 41: Kissinger plots for calculation of activation energy of crystallization in $Fe_{48}Cr_{15}Mo_{14}Y_2C_{15}B_6$ metallic glass powder

3.3 Crystallized fraction

The thermal evolution of the crystallized fraction, α(T) was estimated from the deconvoluted isochronal DSC traces for each of Exo 1, Exo 2 and Exo 3 at all the heating rates according to [164, 3]:

$$\alpha(T) = \frac{\int_{T_o}^{T} (dH/dT)dT}{\int_{T_o}^{T\infty} (dH/dT)dT} = \frac{A_T}{A} \tag{V.2}$$

where T_∞ (K) is the end crystallization temperature, dH/dT ($J\,K^{-1}$) is the heat capacity at constant pressure. A_T and A are the areas under the isochronal DSC traces between T_o and T and between T_o and T_∞ respectively. The results are presented in Fig. 42 where all the plots exhibit a sigmoidal (S-shaped) response upon increase in temperature at all

heating rates. The sigmoidal pattern indicates that the crystallization in this amorphous alloy occurs through the process of nucleation and growth which can be approximately divided into 3 overlapping stages [165]. The first one is dominated by the formation of nuclei throughout the alloy while the rate of transformation remains low as observed for $0 < \alpha < 0.1$. In the following stage, the reduction in volume free energy due to the formation of stable crystallites dominates the increase in surface free energy due to the interfaces created between the crystallites and the amorphous matrix. The formation of stable crystallites alters the composition of the residual amorphous matrix resulting in the formation of concentration gradients thereby reducing its stability. This leads to subsequent non-random nucleation and preferential crystallization near existing ones [104] culminating in a steady increase in the crystallized fraction for $0.1 < \alpha < 0.9$. In the final stage, interaction between multiple concentration gradients, designated as soft impingement [166], results in the reduction and eventual cessation of crystallization as observed for $0.9 < \alpha < 1.0$.

3.4 Mechanism of crystallization

In order to understand the continuous variation in the rate of crystallization throughout the process, observed in Fig. 42, the nucleation and growth mechanism was analyzed following the estimation of the local Avrami exponent, n(α) under the theoretical framework of the Johnson-Mehl-Avrami-Kolmogorov (JMAK) model.

In isothermal annealing experiments, the crystallization kinetics of amorphous alloys can be expressed by the JMAK equation as [167, 168]:

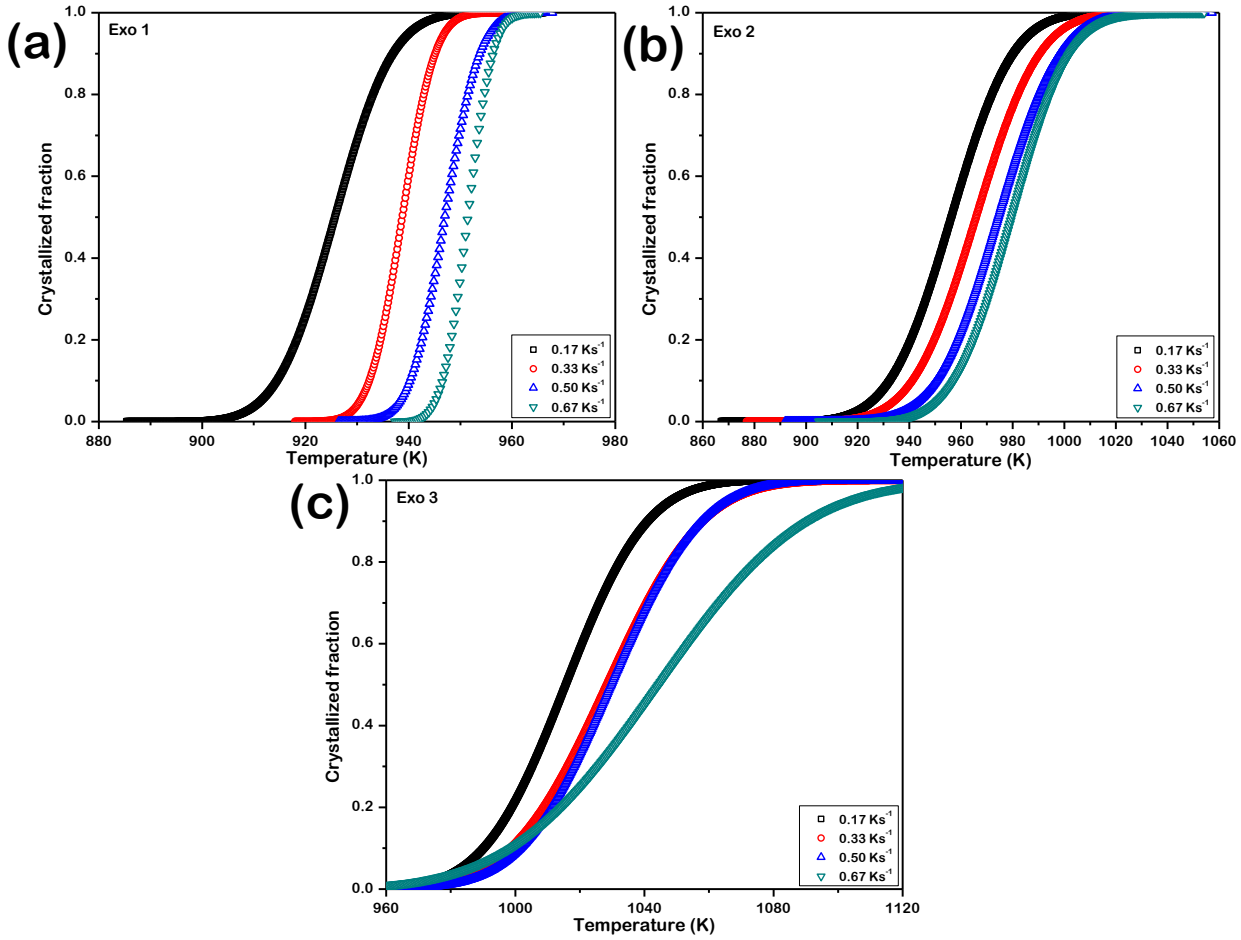

Figure 42: Thermal evolution of crystallized fraction of (a) Exo 1, (b) Exo 2 and (c) Exo 3 in $Fe_{48}Cr_{15}Mo_{14}Y_2C_{15}B_6$ metallic glass powder at different heating rates

$$\alpha(t) = 1 - \exp[-\{k(t-\tau)\}^n] \tag{V.3}$$

where k (s^{-1}) is a kinetic coefficient which is a function of temperature, t (s) is the time and τ (s) is the incubation time. With a constant value of k under isothermal conditions, the JMAK equation can be rescripted as:

$$\ln[-\ln(1-\alpha)] = n\ln(t-\tau) + constant \tag{V.4}$$

to deduce n(α) by differentiation as:

$$n(\alpha) = \frac{d\ln[-\ln(1-\alpha)]}{d\ln(t-\tau)} \tag{V.5}$$

A generalization of the JMAK equation, applicable to non-isothermal transformations, can be expressed as [169, 170]:

$$\alpha(t) = 1 - \exp\left[-\left\{\int_{\tau}^{t} k(T)dt\right\}^{n}\right] \tag{V.6}$$

under the isokinetic approximation whereby it is assumed that the transformation is independent of the thermal history of the alloy. It is noted here that for isothermal annealing experiments Eq. V.6 reduces to the JMAK equation since k(T) is a constant. For isochronal transformations, as in the present investigation, the relationship between temperature and time can be expressed as:

$$\frac{dT}{dt} = c \tag{V.7}$$

and utilized to modify Eq. V.6 as [170]:

$$\alpha(T) = 1 - \exp\left[-\left\{\frac{1}{c}\int_{T_{\mathrm{o}}}^{T} k(T)dT\right\}^{n}\right] \tag{V.8}$$

A new kinetic coefficient, k'(T) (s^{-1}), defined as a function of temperature as [163]:

$$k'(T) = k'_o exp\left(\frac{E_\mathrm{p}}{RT}\right) \tag{V.9}$$

where k'_o(T) (s^{-1}) is the constant frequency factor, is used to replace k(T) following [170]:

$$\int_{T_\mathrm{o}}^{T} k(T)dT = k'(T - T_\mathrm{o}) \tag{V.10}$$

Eq. V.8 thus reduces to [168]:

$$\alpha(T) = 1 - \exp\left[-\left\{\frac{k'}{c}(T - T_\mathrm{o})\right\}^n\right] \tag{V.11}$$

A solution of Eqs. V.8, V.9 and V.11 together can be used to deduce n(α) for a non-isothermal transformation as [3]:

$$n(\alpha) = \frac{1}{1 + \frac{E_\mathrm{p}}{RT}\left(1 - \frac{T_\mathrm{o}}{T}\right)} \frac{d[\ln\{-\ln(1-\alpha)\}]}{d[\ln(\frac{T-T_\mathrm{o}}{c})]} \tag{V.12}$$

The plots of ln[-ln(1-α)] with respect to ln[(T - T_o)/c] are presented in Fig. 43. The slopes of the plots indicate that the nucleation and growth behavior varies gradually during the crystallization process.

3.5 Nucleation and growth

The variation in the nucleation and growth behavior is represented by the local Avrami exponent, n which is related to a, the nucleation index, b, the dimensionality of growth and p, the growth index as [4, 5]:

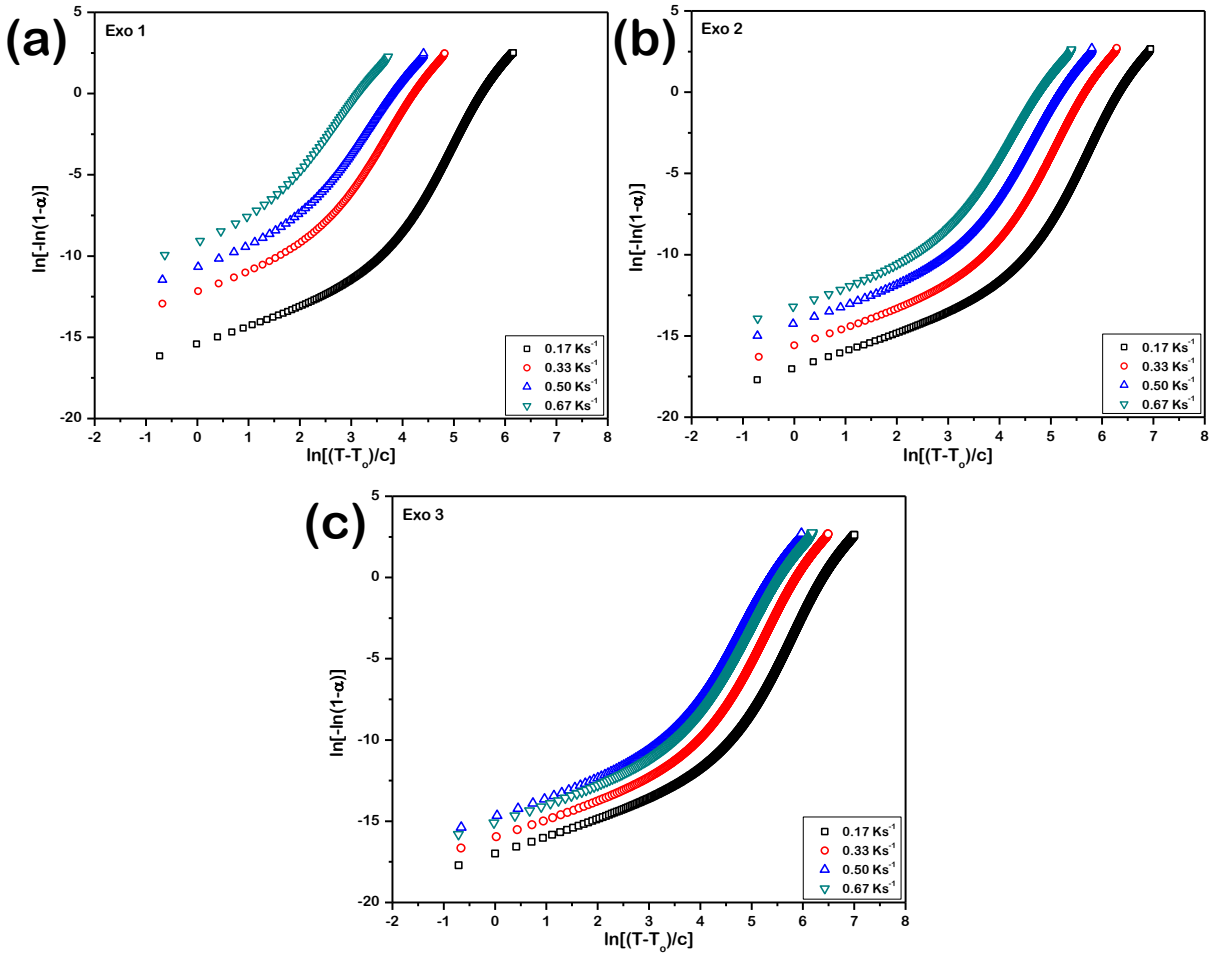

Figure 43: Plots of ln[-ln(1-α)] versus ln[(T - T_o)/c] of (a) Exo 1, (b) Exo 2 and (c) Exo 3 in $Fe_{48}Cr_{15}Mo_{14}Y_2C_{15}B_6$ metallic glass powder at different heating rates

$$n = a + bp \tag{V.13}$$

Different values of a, b, p and thus n reflect the various mechanisms of nucleation and growth prevalent during the progress of the crystallization process which are summarized in Table 6 [3].

Table 6: Values of nucleation and growth parameters as a reflection of crystallization mechanism in $Fe_{48}Cr_{15}Mo_{14}Y_2C_{15}B_6$ metallic glass [3, 4, 5]

Parameter	Value	Interpretation
a	0	Zero nucleation rate
	$\in (0\ ,\ 1)$	Decreasing nucleation rate
	1	Constant nucleation rate
	>1	Increasing nucleation rate
b	1	One dimensional growth
	2	Two dimensional growth
	3	Three dimensional growth
p	0.5	Diffusion controlled growth
	1	Interface controlled growth
n	<1.5	Growth of pre-existing nuclei
	1.5	Growth with zero nucleation rate
	$\in (1.5\ ,\ 2.5)$	Growth with decreasing nucleation rate
	2.5	Growth with constant nucleation rate
	>2.5	Growth with increasing nucleation rate

3.6 Local Avrami exponent

The variation of the local Avrami exponent was estimated as a function of the crystallized fraction following Eq. V.12 and the results are plotted in Fig. 44. It can be observed that for Exo 1 (Fig. 44a), n rapidly increases to about 3.1 at the beginning of the transformation at all heating rates. At $0.17\,\mathrm{K\,s^{-1}}$, n gradually reduces to attain values in the range of 2.5 to 1.5 for $0.1 < \alpha < 0.8$ while for $\alpha > 0.8$ it is lesser than 1.5. At all other heating rates, 0.33, 0.50 and 0.67 $\mathrm{K\,s^{-1}}$, n attains values in the range of 2.5 to 1.5 for the

entire transformation. Spanning the entire transformation, an increase in heating rate beyond $0.17\,\mathrm{K\,s^{-1}}$ generally results in an increase in n. In contrast, for Exo 2 (Fig. 44b), n is almost independent of the heating rate, increasing rapidly to about 1.8 at the beginning of the transformation before reducing to values less than 1.5 for the entire transformation. The trend is reversed in case of Exo 3 (Fig. 44c) where, spanning the entire transformation, an increase in heating rate beyond $0.50\,\mathrm{K\,s^{-1}}$ results in a decrease in n. At heating rates from 0.17 to $0.50\,\mathrm{K\,s^{-1}}$ n attains a value of about 1.8 at the beginning of the transformation before gradually reducing below 1.5 from $\alpha = 0.1$ onwards. An increase in the heating rate to $0.67\,\mathrm{K\,s^{-1}}$ keeps the value of n below 1.5 for the entire transformation.

The process of crystallization in Fe-based amorphous alloys [171, 172] including the one employed in this investigation [104] as well as that without Y-modification [6] has been extensively reported to occur by diffusion controlled processes whereby p = 0.5 (Table 6). Thus from the values of n observed in Fig. 44, it can be concluded that the Exo 1 transformation begins with diffusion controlled three-dimensional growth with increasing nucleation rate. It proceeds with a decreasing nucleation rate before concluding with the growth of these crystallites. Both of Exo 2 and Exo 3 begin with a growth of precipitates with decreasing nucleation rate while most of the transformations occur with a growth of these crystallites without further nucleation. The overall characteristic of decreasing nucleation rates throughout the progress of all the transformations indicate that the crystallization process in this amorphous alloy is mostly growth controlled. This is comprehensible as slow conventional heating rates were employed in this investigation.

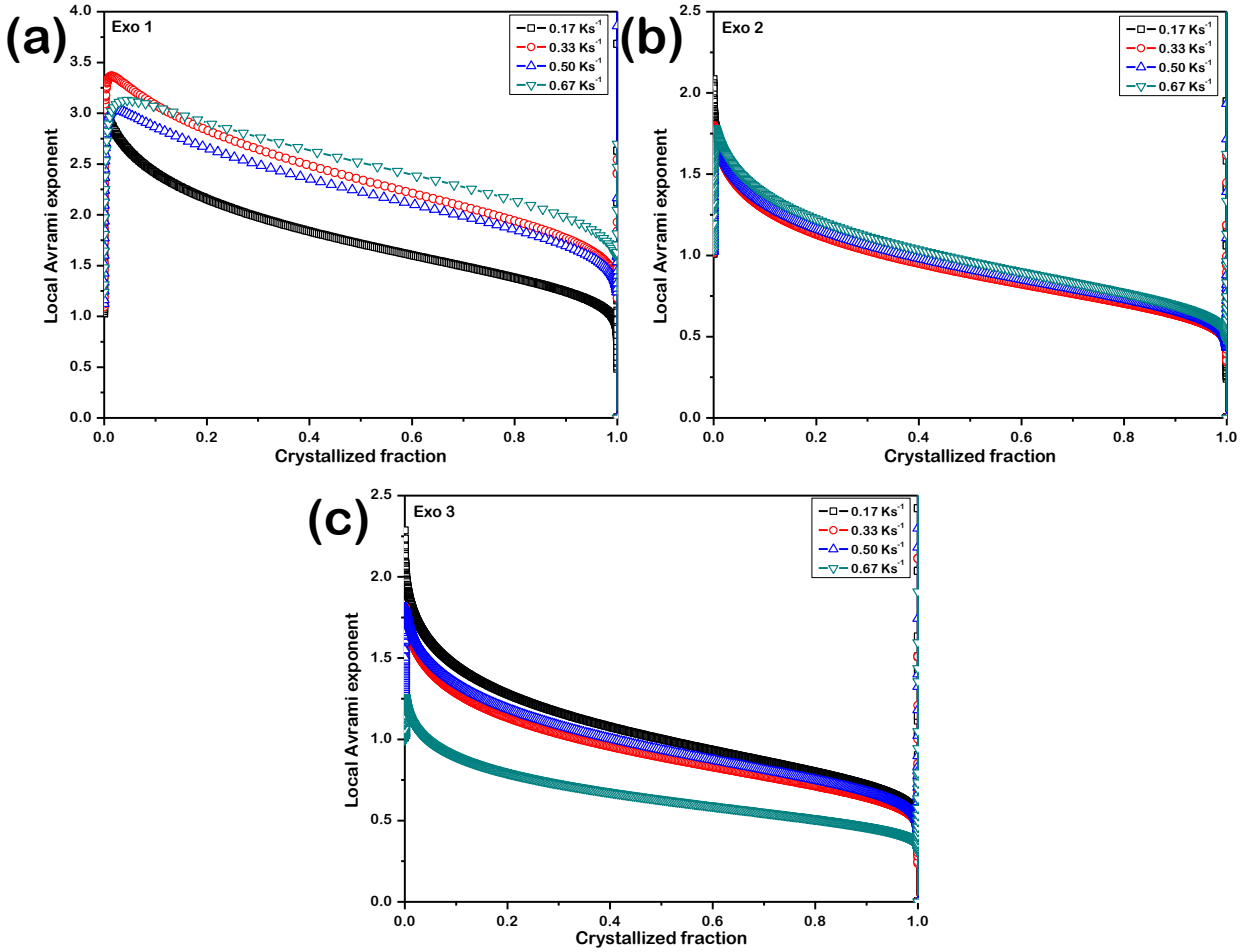

Figure 44: Local Avrami exponent as a function of crystallized fraction of (a) Exo 1, (b) Exo 2 and (c) Exo 3 in $Fe_{48}Cr_{15}Mo_{14}Y_2C_{15}B_6$ metallic glass powder at different heating rates

3.7 Dependence on analytical method

The local Avrami exponent may possibly be affected by the assumption of a Gaussian shape for the exothermic peaks of crystallization. On the other hand, the Gao-Wang method, [100], using only the peak values of onset crystallization temperature will not be strongly dependent on this assumption while yielding an average value of the local Avrami exponent for the entire transformation. The average Avrami exponent, n_{avg} can be estimated as:

Table 7: Average Avrami exponent in $Fe_{48}Cr_{15}Mo_{14}Y_2C_{15}B_6$ metallic glass powder estimated by the Gao-Wang method

c ($K\,s^{-1}$)	**Exo 1**	**Exo 2**	**Exo 3**
0.17	2.37	1.01	1.15
0.33	4.29	1.04	1.00
0.50	4.13	1.04	1.07
0.67	5.75	1.12	0.67

$$\frac{dx_{\mathrm{p}}}{dt_{\mathrm{p}}} = 0.37 n_{\mathrm{avg}} \left(\frac{cE_{\mathrm{p}}}{RT_p^2} \right) \tag{V.14}$$

The estimated values of n are tabulated in Table 7.

The following observations are identical to the estimated values of both the local Avrami exponent and the average Avrami exponent.

- Both n and n_{avg} for Exo 1 transformation increases with an increase in heating rate
- Both n and n_{avg} for Exo 2 transformation is almost independent of the heating rate
- Both n and n_{avg} for Exo 3 transformation decreases for an increase in heating rate beyond $0.50\,K\,s^{-1}$

It can be observed that overall, this single value presented in Table 7 belongs to the estimated range of local Avrami exponent as presented in Fig. 44. Moreover, it is to be noted that the conclusions on the mechanism of crystallization according to Table 6, derived from the local Avrami exponent as well as the average Avrami exponent are identical.

Additionally, the value of T_o has been reported to be optimized to $T_p/2$ [101]. This

affects the value of the local Avrami exponent, in particular, at low crystallized fractions. In order to investigate this, the local Avrami exponent as a function of the transformed fraction, according to the optimized value of T_o can be expressed as:

$$n(\alpha) = \frac{1}{1 + \frac{E_p}{RT}\left(1 - \frac{T_p}{2T}\right)} \frac{d[\ln\{-\ln(1-\alpha)\}]}{d[\ln(\frac{T - \frac{T_p}{2}}{c})]} \tag{V.15}$$

The values of n are estimated and the results are presented in Fig. 45. The observations identical to the local Avrami exponent estimated both with T_o as the onset crystallization temperature and as equal to $T_p/2$ are

- For Exo 1 n increases with increase in c
- For Exo 2 n is almost independent of c
- For Exo 3 n decreases for an increase in c beyond $0.50\,\mathrm{K\,s^{-1}}$

Close agreement between the values of n estimated by the two different approaches can be observed, even at low transformed fractions. Only for Exo 1, at low transformed fractions, the value of n is higher in the present method. In spite of this, the values, according to Table 6, yield identical conclusions on the mechanism of crystallization in the alloy. Therefore it can be concluded that the inference on the mechanism of crystallization derived from the values of local Avrami exponent estimated according to T_o equal to crystallization onset temperature and $T_p/2$ are identical.

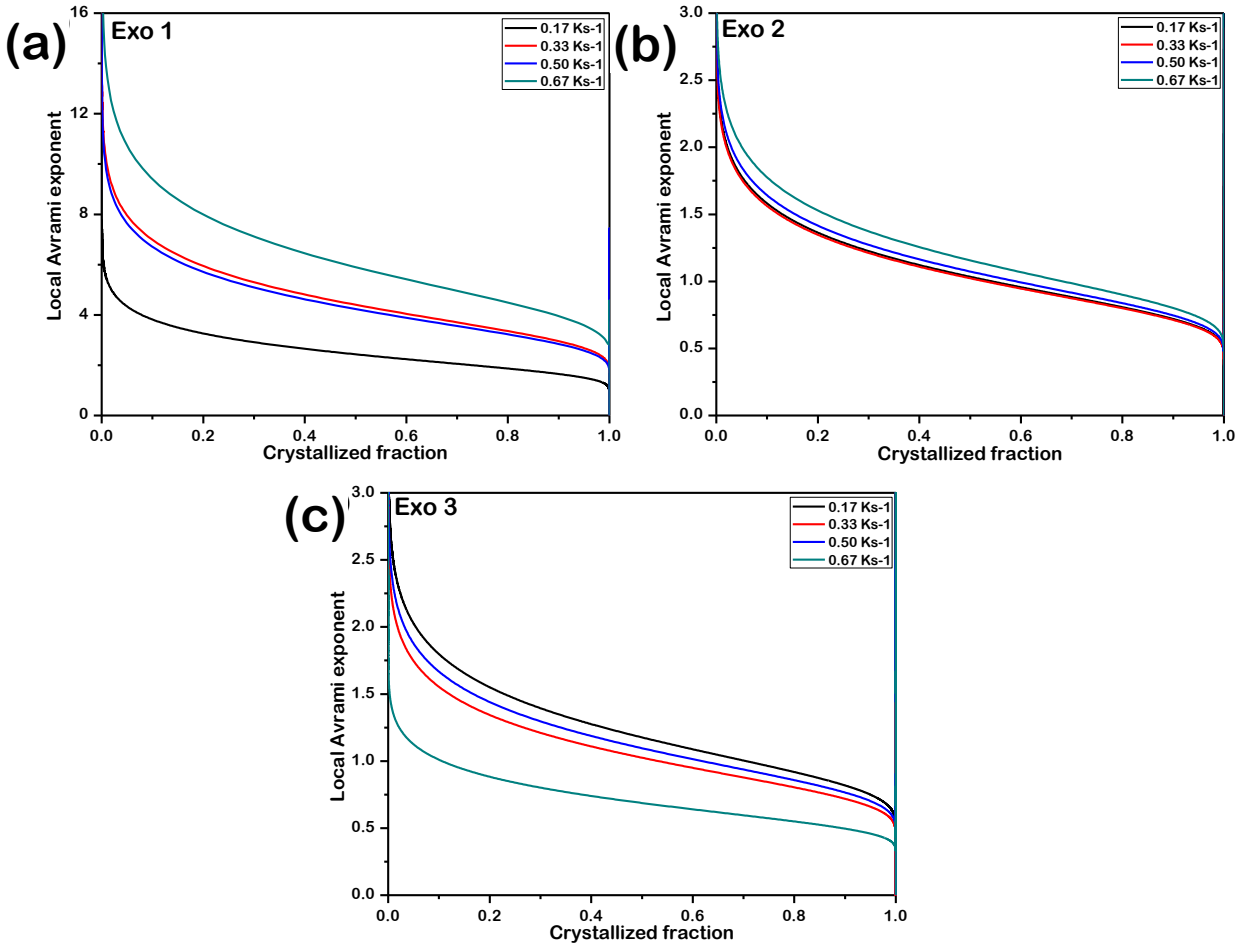

Figure 45: Local Avrami exponent as a function of crystallized fraction of (a) Exo 1, (b) Exo 2 and (c) Exo 3 in $Fe_{48}Cr_{15}Mo_{14}Y_2C_{15}B_6$ metallic glass powder estimated with T_o optimized to $T_p/2$ following Blazquez *et. al*

3.8 Effect of Y-modification

A comparison of the phase evolution and crystallization kinetics of the Y-modified $Fe_{48}Cr_{15}Mo_{14}Y_2C_{15}B_6$ alloy, employed in the present investigation, with those of the unmodified $Fe_{50}Cr_{15}Mo_{14}C_{15}B_6$ one revealed the effect of addition of minor amount of yttrium. The evolution of phases in this metallic glass as a result of isochronal annealing is exhibited by the x-ray diffraction (XRD) spectra presented in Fig. 46. It can be observed that the increase

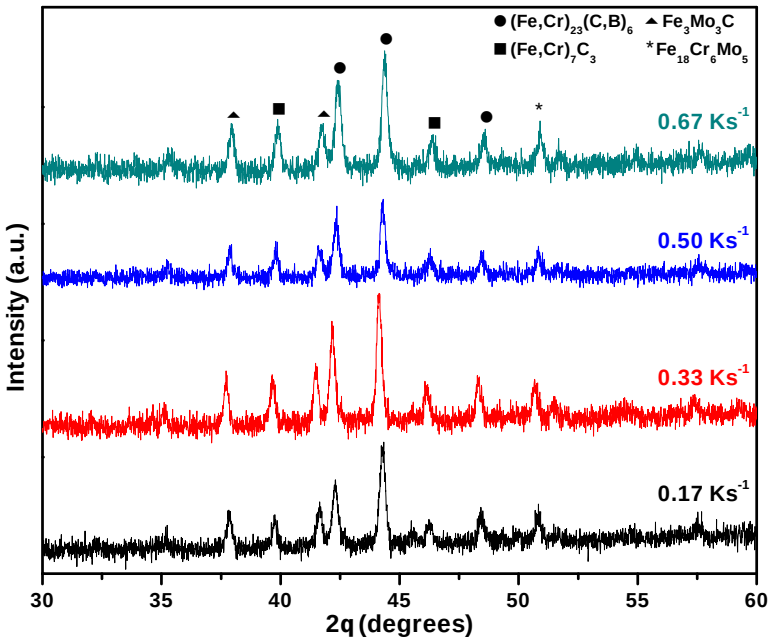

Figure 46: X-ray diffraction spectra of $Fe_{48}Cr_{15}Mo_{14}Y_2C_{15}B_6$ metallic glass powder annealed up to 1200 K at different heating rates

in heating rate does not affect the evolution of phases. Identical phases have been observed during the isochronal annealing of $Fe_{50}Cr_{15}Mo_{14}C_{15}B_6$ metallic glass where the sequence of crystallization was reported to be $Fe_{18}Cr_6Mo_5$ followed by $(Fe,Cr)_{23}(C,B)_6$, $(Fe,Cr)_7C_3$ and finally Fe_3Mo_3C [6]. The exothermic transformations in the present investigation, namely Exo 1, Exo 2, Exo 3 and Exo 4 can thus, by comparison, be designated as $Fe_{18}Cr_6Mo_5$, $(Fe,Cr)_{23}(C,B)_6$, $(Fe,Cr)_7C_3$ and Fe_3Mo_3C respectively. Additionally it can be concluded that the Y-modification does not alter the nature of the resulting crystalline phases. A close agreement was observed between the ratio of phases estimated from the DSC traces and XRD spectra which indicates the reliability of the deconvolution performed (Fig. 40).

The onset crystallization temperature, T_o of the $Fe_{50}Cr_{15}Mo_{14}C_{15}B_6$ metallic glass has been reported to be 878 K whereas it was observed to be increased to 916 K for $Fe_{48}Cr_{15}Mo_{14}Y_2C_{15}B_6$

Table 8: Comparison of crystallization kinetics of yttrium-modified (M) and unmodified (UM) Fe-based metallic glasses after [6]

Phase	**Local Avrami exponent**	
	UM	**M**
$Fe_{18}Cr_6Mo_5$	2.5	2.5 - 1.5
$(Fe,Cr)_{23}(C,B)_6$	2.5	<1.5
$(Fe,Cr)_7C_3$	6.3	<1.5

in the present investigation. Additionally, the local Avrami exponents of the crystalline transformations of the $Fe_{18}Cr_6Mo_5$, $(Fe,Cr)_{23}(C,B)_6$ and $(Fe,Cr)_7C_3$ phases were also altered as presented in Table 8 [6].

While the local Avrami exponent for the unmodified alloy is 2.5 or higher, upon modification it reduced to the range of 2.5-1.5 or even lesser. According to Table 6, it can thus be concluded that in the unmodified alloy crystallization progresses with an increasing nucleation rate while upon Y-modification growth occurs with a decreasing nucleation rate or from nuclei that have already formed. This reduction in nucleation rate can be attributed to the relative disparity between the sizes of the atoms. Yttrium has an atomic radius of 1.8 Å and is the largest among the atoms of all the constituent elements in the alloy [173]. The presence of this bulky atom results in an increase in the local density of the Y-modified alloy due to formation of a larger number of short range ordered colonies. This leads to a significant decrease in the diffusivity [174] of the atoms that manifests itself in a reduced nucleation rate [175] and hence decreased n. The impediment to crystallization is also supported by the complete absence of precipitation of the α-Fe phase during crystallization

of both the alloys. Yttrium also possesses the highest affinity towards oxygen among all the constituent elements of the alloy as exhibited by the largest enthalpy of formation of its oxide [174]. Thus during rapid solidification of the liquid melt of the alloy, yttrium aids in the elimination of oxygen impurity in the form of oxides. This, combined with the large negative heat of mixing of yttrium with boron ($-35\,\mathrm{kJ\,mol^{-1}}$) [176] possibly increases the thermal stability of the alloy and increases T_o by almost 40 K.

4 Crystallization in spark plasma sintered $Fe_{48}Cr_{15}Mo_{14}Y_2C_{15}B_6$ metallic glass powder

4.1 Structural analysis

The x-ray diffraction (XRD) spectrum of the iron based metallic glass spark plasma sintered at 550 °C is presented in Fig. **??**. It only exhibits a diffused peak, characteristic of fully amorphous materials whereas sharp peaks, indicative of crystalline phases are absent. Thus it can be concluded that upon spark plasma sintering (SPS) at a temperature of 550 °C, the iron based metallic glass sample retained an amorphous structure. The differential scanning calorimetric thermogram of this iron based metallic glass manifests a glass transition temperature, T_g of about 575 °C and a crystallization onset temperature, T_x of about 653 °C [177]. Thus it is comprehensible that the sample sintered at 550 °C, a temperature below T_g, remains in the glassy state. The XRD spectra of the iron based metallic glass spark plasma sintered at 550 °C and then annealed at 700 °C and 725 °C for 100 min each, are also presented. In contrast to solely a broad peak, these spectra exhibit additional peaks,

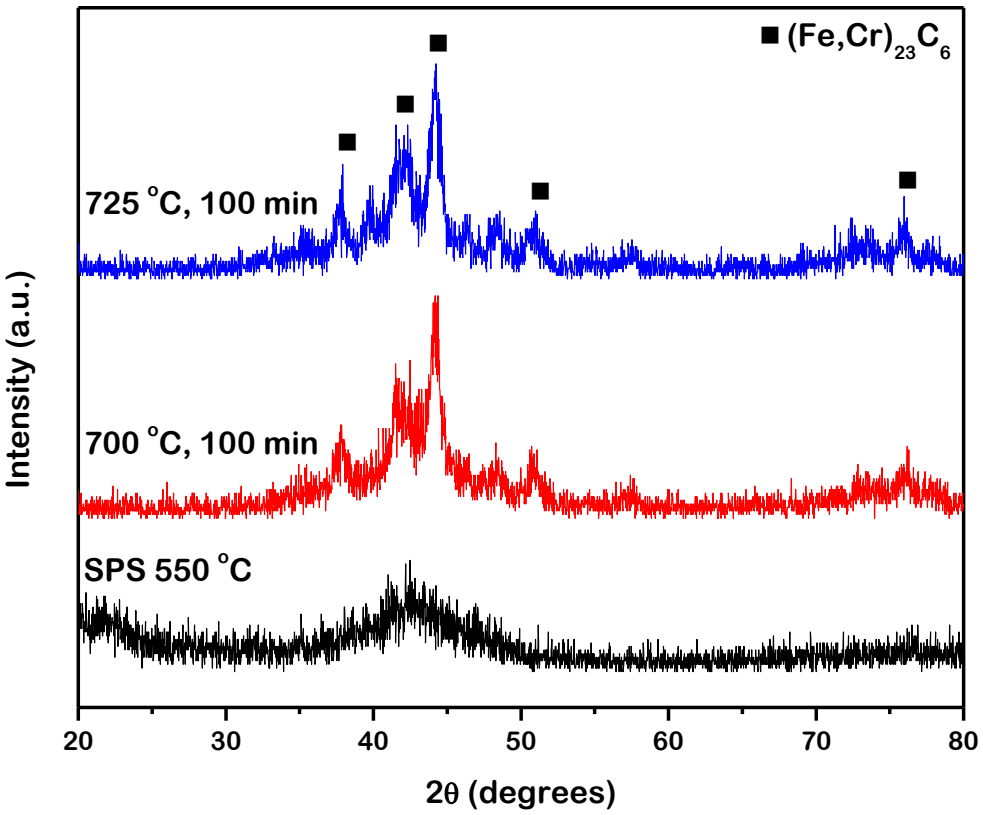

Figure 47: X-ray diffraction spectra of the iron based metallic glass spark plasma sintered at 550 °C and then annealed at 700 °C and 725 °C for 100 min each. The sintered sample retained a fully amorphous structure while the annealed ones developed ($(Fe,Cr)_{23}C_6$) crystals

superimposed on the amorphous background, characteristic to crystals evolved within the iron based metallic glass matrix. The temperatures of annealing (700 °C and 725 °C) are considerably higher than the T_x of this metallic glass which resulted in the evolution of these crystals.

The peaks corresponding to the crystals, identified to be complex carbides of $(Fe,Cr)_{23}C_6$ [104, 178], are observed to exhibit significant broadening which are suggestive of their small sizes. The size of crystals evolved from an amorphous matrix of iron based metallic glass upon thermal processing can be approximately estimated according to the Scherrer equation

expressed as [179]:

$$D = \frac{0.9\lambda}{\beta cos\theta_{\mathrm{B}}} \tag{V.16}$$

where D (Å) is the size of the crystals, λ (Å) is the wavelength of x-rays, β (rad) is the integrated breadth of the Bragg peak and θ_{B} (°) is the Bragg angle. The estimated size of crystals according to Eq. V.16 is about 9 nm for samples annealed at both 700 °C and 725 °C for 100 min. This result is consistent with previous observations where the size of $(Fe,Cr)_{23}C_6$ crystals evolved during annealing at 700 °C for 180 min estimated by the Scherrer equation was reported to be about 16 nm [178]. However, a number of limitations in employing the Scherrer equation must be noted. In utilizing Eq. V.16, the shape factor, size factor, strain factor and preferred orientation factor have not been accounted for. As a result, Eq. V.16 yields only an approximate estimate of the crystal dimensions as opposed to an accurate size. Moreover, the evolution of crystals in a metallic glass due to annealing is a complex phenomenon driven by nucleation and growth of a number of concentration gradients [104]. It is unlikely that such a phenomenon would result in a monodispersed size distribution of crystals in the metallic glass matrix, as estimated from Eq. V.16. This distribution in size of crystals was investigated further by microstructural characterization as detailed in the following section. Fe_3Mo_3C has also been reported to have evolved during annealing of this metallic glass at 700 °C and above [180]. However, presence of this phase could not be detected from the XRD spectra in the present investigation.

4.2 Microstructural characterization

The transmission electron microscope (TEM) dark field images of the SP sintered iron based metallic glass samples annealed at 700 °C and 725 °C for 100 min are presented in Fig. 48(a) and (b) respectively. The regions of brighter contrast depict the crystals evolved due to annealing from the metallic glass matrix depicted by the regions of darker contrast. The crystals are observed to be distributed homogeneously throughout the metallic glass matrix. Size of the individual crystals were measured from these dark field TEM images by ImageJ with some representative measurements presented herewith. As discussed in the previous section, in contrast to a monodispersed size distribution, the crystals exhibit a range of sizes from about 5 nm to about 16 nm. However, the relative volume fractions of the individual crystal sizes distributed throughout the entire samples cannot be obtained by this manual measurement technique.

The corresponding selected area diffraction patterns (SADPs) of the annealed samples are presented in Fig. 48(c) and (d). The diffuse rings observed in the patterns confirm that a significant volume fraction of the amorphous metallic glass matrix is retained even after annealing. The remaining volume fraction, evolved into crystals of $(Fe,Cr)_{23}C_6$ and Fe_3Mo_3C resulting in the diffraction spots superimposed on the diffuse rings. A detailed quantitative estimate of the size distribution of crystals and their relative volume fractions is obtained from the small angle neutron scattering (SANS) analysis presented in the following sections.

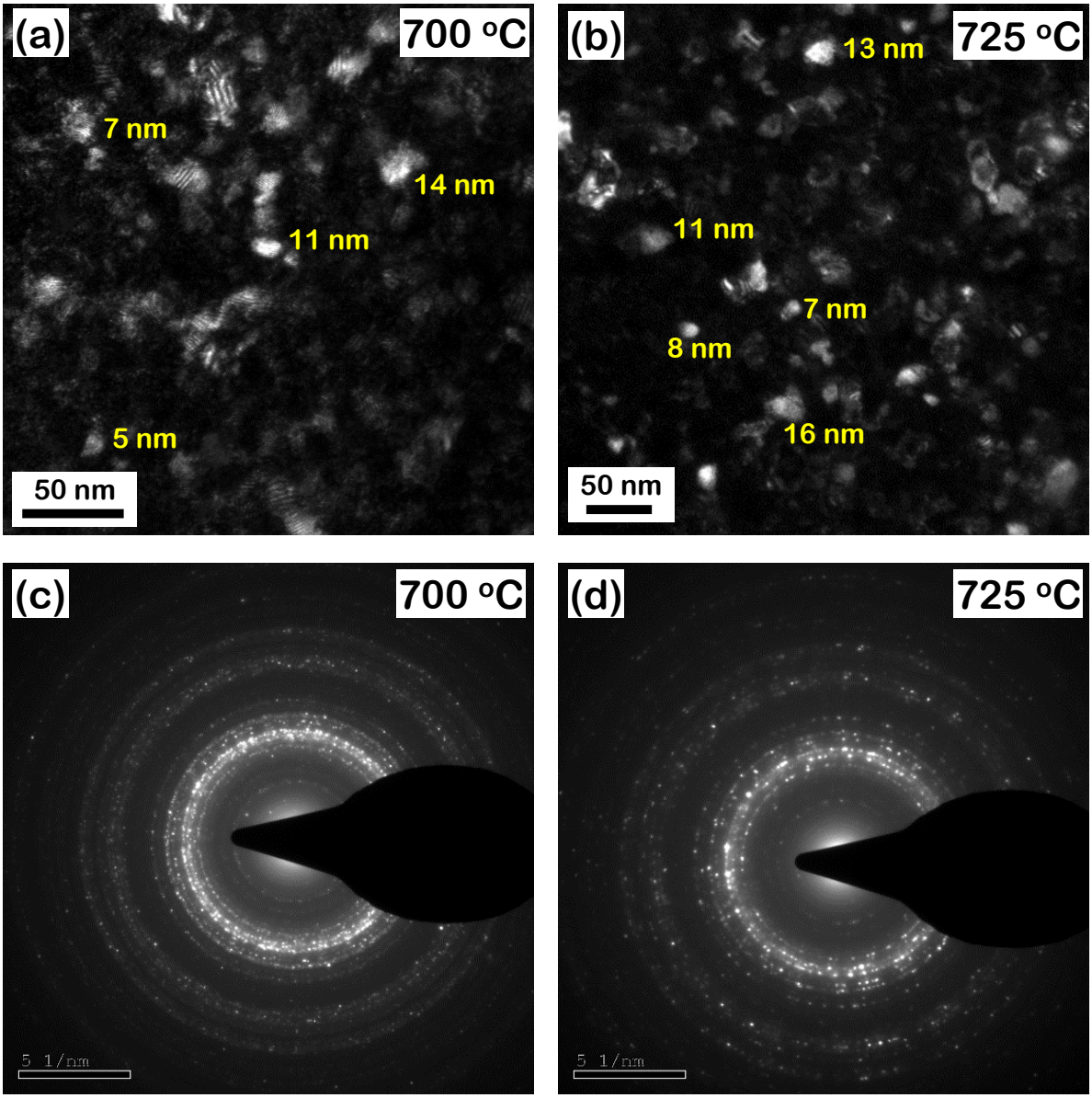

Figure 48: (a) and (b) Transmission electron microscope dark field images and (c) and (d) corresponding selected area diffraction patterns of spark plasma sintered iron based metallic glass annealed at 700 °C and 725 °C for 100 min. Regions of brighter contrast in (a) and (b) represent crystals embedded within the metallic glass matrix that exhibit a range of sizes from 5 to 16 nm.

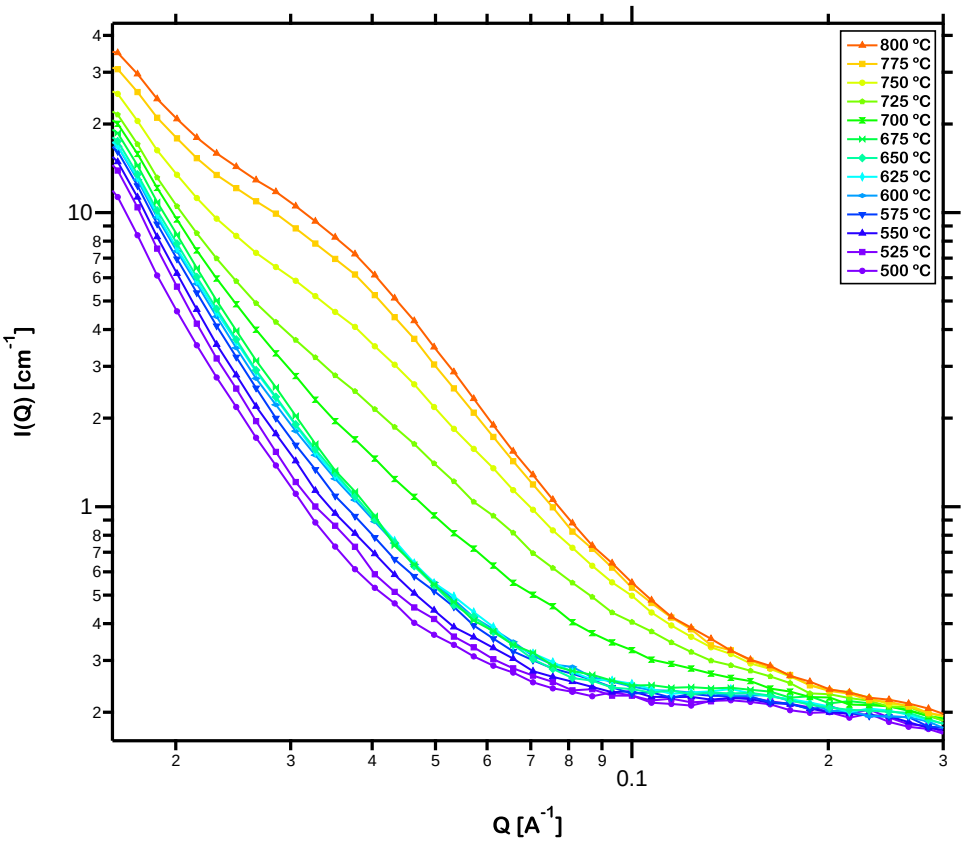

Figure 49: Log-log plot of *in-situ* small angle neutron scattering intensity measured over a Q-range of 0.02 to 0.3 $Å^{-1}$ for the sintered sample continuously annealed from ambient up to different temperatures from 500 °C to 800 °C

4.3 Evolution of structure based on *in-situ* small angle neutron scattering

The structural evolution of the iron based metallic glass was quantitatively analyzed by *in-situ* SANS during annealing. Fig. 49 presents the SANS intensity over a Q-range of 0.02 to 0.3 $Å^{-1}$ in a log-log plot for the sintered sample continuously annealed from ambient up to different temperatures from 500 °C to 800 °C. The characteristics of scattering, corresponding interpretation as representative of phenomena occurring over distinct length scales and their evolution with increase in annealing temperature are discussed across three discrete Q-ranges as follows.

First, over the low Q-range below $0.02\,\text{Å}^{-1}$, the presence of scattering indicates the presence of structural inhomogeneities that are larger than those that can be effectively resolved by the present experiments. The size of these inhomogeneities are larger than 30 nm and could possibly be Y and Mo-rich precipitate free zones (PFZs) embedded within the metallic glass matrix [181]. These PFZs have been observed during annealing of as-cast iron based metallic glass with diameter up to 200 nm [178]. They develop from the metallic glass matrix and upon further enrichment by Y possess an increased glass forming ability (GFA) [182]. Thus they retain their amorphous nature and are hence not detectable in the XRD spectrum (Fig. 47). The PFZs have high thermal stability and thus continue to contribute to the scattering intensity over this Q-range at higher temperatures up to 800 °C [178]. The neutron scattering length densities, ρ (m^{-2}) of the PFZs and $(\text{Fe,Cr})_{23}\text{C}_6$ and their corresponding contrasts, $\Delta\rho^2$ (m^{-4}) with respect to the $\text{Fe}_{48}\text{Cr}_{15}\text{Mo}_{14}\text{Y}_2\text{C}_{15}\text{B}_6$ metallic glass matrix can be calculated based upon their reported composition [180]. The composition of the PFZs at low temperatures is $\text{Fe}_{41}\text{Cr}_{16}\text{Mo}_{29}\text{Y}_{14}$ (at.%). They get enriched in Y and Mo and depleted of Fe and Cr with increase in temperature and has a composition of $\text{Fe}_{35}\text{Cr}_{11}\text{Mo}_{37}\text{Y}_{17}$ at 700 °C. This fact is incorporated while calculating the scattering contrasts, presented in Table 9. The composition of $(\text{Fe,Cr})_{23}\text{C}_6$ remains fairly constant with temperature. It can be seen that the scattering contrast of the Y and Mo-rich PFZs is always higher than that of $(\text{Fe,Cr})_{23}\text{C}_6$. This results in a higher measured intensity at the Q-range characteristic of the PFZs (below $0.02\,\text{Å}^{-1}$) than that at the Q-range characteristic of the $(\text{Fe,Cr})_{23}\text{C}_6$ carbides (from 0.02 to 0.2 Å^{-1}). Moreover, the scattering contrast of the

Table 9: Composition and neutron scattering length density, ρ of the iron based metallic glass matrix, precipitate free zones and carbide and their corresponding neutron scattering contrasts with respect to the metallic glass matrix

Composition	ρ (x 10^{-14} m^{-2})	$\Delta\rho^2$ (x 10^{-28} m^{-4})
$Fe_{48}Cr_{15}Mo_{14}Y_2C_{15}B_6$	6.75	0
$Fe_{41}Cr_{16}Mo_{29}Y_{14}$	4.95	3.24
$Fe_{35}Cr_{11}Mo_{37}Y_{17}$	4.69	4.25
$(Fe,Cr)_{23}C_6$	7.28	1.15

PFZs increases with temperature which is manifested in the increase in scattering intensity with temperature over the Q-range below $0.02\,\text{Å}^{-1}$.

Second, over the mid Q-range from 0.02 to 0.2 Å^{-1}, scattering results from the evolution of $(Fe,Cr)_{23}C_6$ crystals withing the iron based metallic glass matrix during continuous annealing. The size of the carbides is in the range of about 3 to 30 nm, in good agreement with those reported earlier [178]. The formation of the PFZs results in the depletion of Y content in the surrounding matrix that results in a reduction of the GFA. These regions are thus enriched in Fe and Cr eventually evolving into crystalline carbides. Fig. 49 shows that significant increase in scattering intensity does not occur until 675 °C which exhibits the stability of this iron based metallic glass and its resistance to crystallization. Thereafter, with further increase in temperature beyond 700 °C, profuse crystallization occurs resulting in a monotonic increase in the scattering intensity in this Q-range.

Finally, over the high Q-range above $0.2\,\text{Å}^{-1}$, background scattering occurred due to the presence of roughness at the sample surface, the detector and other minute variations. These contributions are unrelated to the evolution of crystals and are roughly independent of Q [154]. This is further supported by the fact that the background scattering does not

vary with increment in the temperature of annealing.

4.4 Crystal size distribution

The SANS intensity over the Q-range of 0.02 to 0.06 $Å^{-1}$ was utilized to analyze the distribution of size and volume fraction of $(Fe,Cr)_{23}C_6$ crystals. The maximum entropy model [183] in the size distribution tool available in IRENA software suite [90] was employed for this purpose. It is assumed in this model that the scattering particles are approximately equiaxed which is valid in the present case as can be observed from Fig. 48(a) and (b) where the growth of crystals is reasonably isotropic and no particular growth direction appears to be favored over another. Under this assumption the tool fits and thereby estimates the size distribution of spheres, each with a uniform diameter. Fig. **??** presents a representative maximum entropy model fit to the measured intensity for the sample annealed at 800 °C. The measured intensity is higher than the fitted model at higher Q which suggests that there exists additional scattering, possibly from Fe_3Mo_3C, however of extremely small magnitude due to the much lower scattering contrast, 0.04×10^{-28} m^{-4} as compared to that of $(Fe,Cr)_{23}C_6$ (Table 9) with respect to the metallic glass. The size distribution analysis of various carbides including $(Fe,Cr)_{23}C_6$ and Fe_3Mo_3C evolved in steels as a result of annealing has been successfully performed and the results validated with microscopic characterization techniques [184]. This indicates that the magnetic contribution from these carbides does not affect the distribution of size and volume fraction estimated from fitting the SANS intensity. Additionally, since the experiments were carried out in the absence of a magnetic field the ferromagnetic coupling between the crystals is unlikely to affect the estimated size

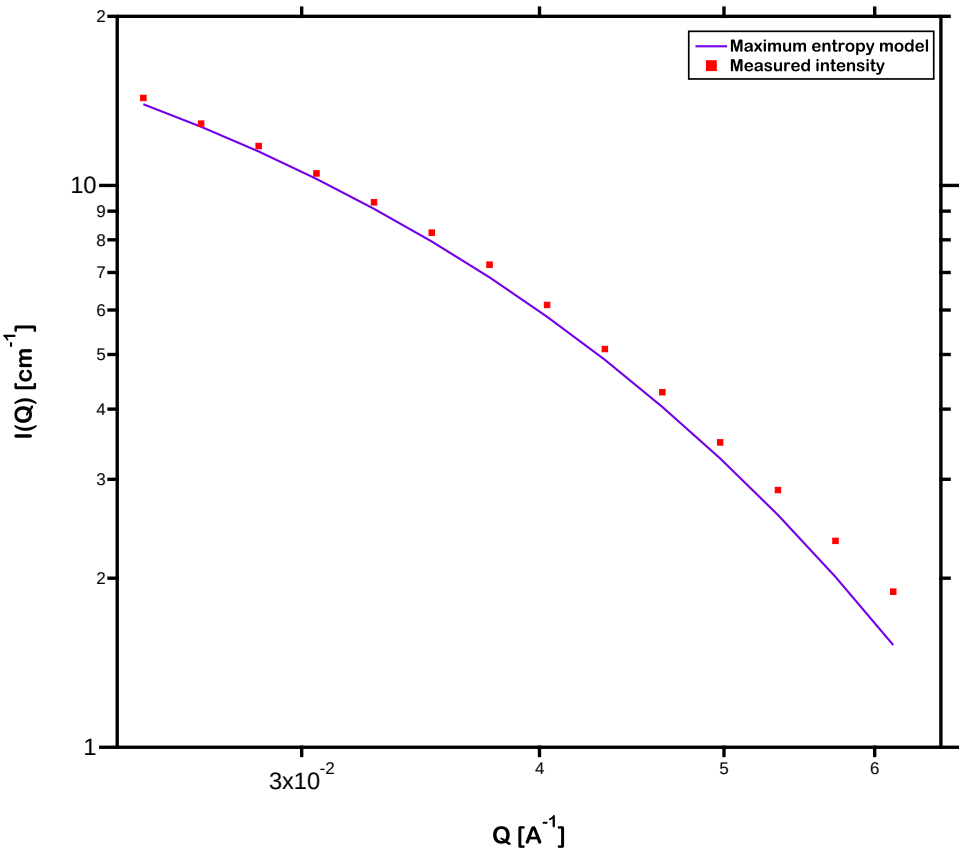

Figure 50: Representative fit of the maximum entropy model to the measured small angle neutron scattering intensity over a Q-range of 0.02 to 0.06 Å^{-1} utilized to analyze the distribution of size and volume fraction of $(Fe,Cr)_{23}C_6$ crystals. The fitted model agrees well with the measured data with the misfit at higher Q originating from additional scattering from Fe_3Mo_3C

distribution [104].

This fitting routine is employed to the measured intensity for the samples isothermally annealed at 700 °C and 725 °C for 100 min, presented in Fig. 51. The higher intensity of scattering clearly confirms the higher volume fraction of crystals evolved at the higher temperature of annealing. The resulting distribution of the volume of $(Fe,Cr)_{23}C_6$ crystals of various sizes is presented in Fig. 52. It can be observed that the crystals evolved have sizes ranging from 3 to 18 nm, in agreement with the sizes observed in the TEM dark field images (Fig. 48(a) and (b)). This confirms the earlier argument that the magnetic contributions

do not affect the estimated size distribution analysis. Among these sizes, the crystals with size 9 nm is observed to be in highest abundance, again in accord with that estimated by the Scherrer equation in section 4.1. With increase in duration of isothermal annealing, the volume fraction of all crystal sizes increases. The total volume fraction of $(Fe,Cr)_{23}C_6$ crystals during isothermal annealing increased from 0.07 to 0.13 at 700 °C and from 0.10 to 0.22 at 725 °C. It can also be observed from Fig. 52 that the increase in volume fraction of carbides evolved with time is rapid during the early stages of isothermal annealing and slows down during the later stages. These crystals develop preferentially in the regions depleted of Y and Mo and enriched in Fe and Cr and the rate of growth is rapid due to the large driving force resulting from the reduction in free energy from amorphous to crystalline state. With time, concentration gradients in regions neighboring these crystals grow and eventually encounter with one another, a process termed 'soft impingement', and suppress the rate of coarsening of the crystals [166].

4.5 Crystallization mechanism

In order to establish the mechanism of isothermal crystallization in the spark plasma sintered iron based metallic glass, the results obtained from the *in-situ* small angle neutron scattering analysis of the distribution of volume fraction of $(Fe,Cr)_{23}C_6$ crystals were modeled by the Johnson-Mehl-Avrami equation, expressed as [169, 168]:

$$\ln[-\ln(1-x)] = n\ln t + n\ln k \tag{V.17}$$

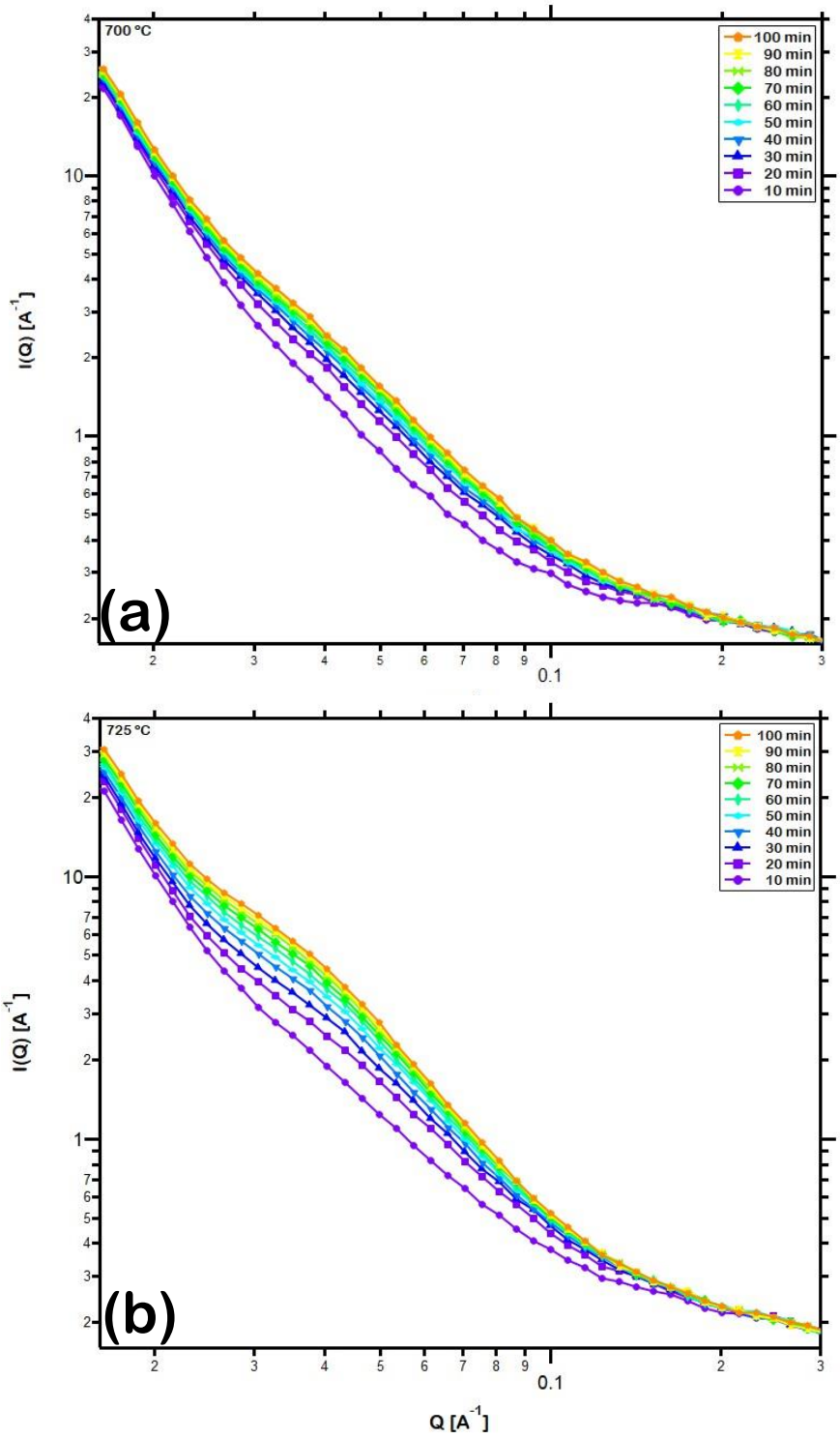

Figure 51: Log-log plot of *in-situ* small angle neutron scattering intensity measured over a Q-range of 0.02 to 0.3 Å^{-1} for the sintered sample isothermally annealed at (a) 700 °C and (b) 725 °C for 100 min.

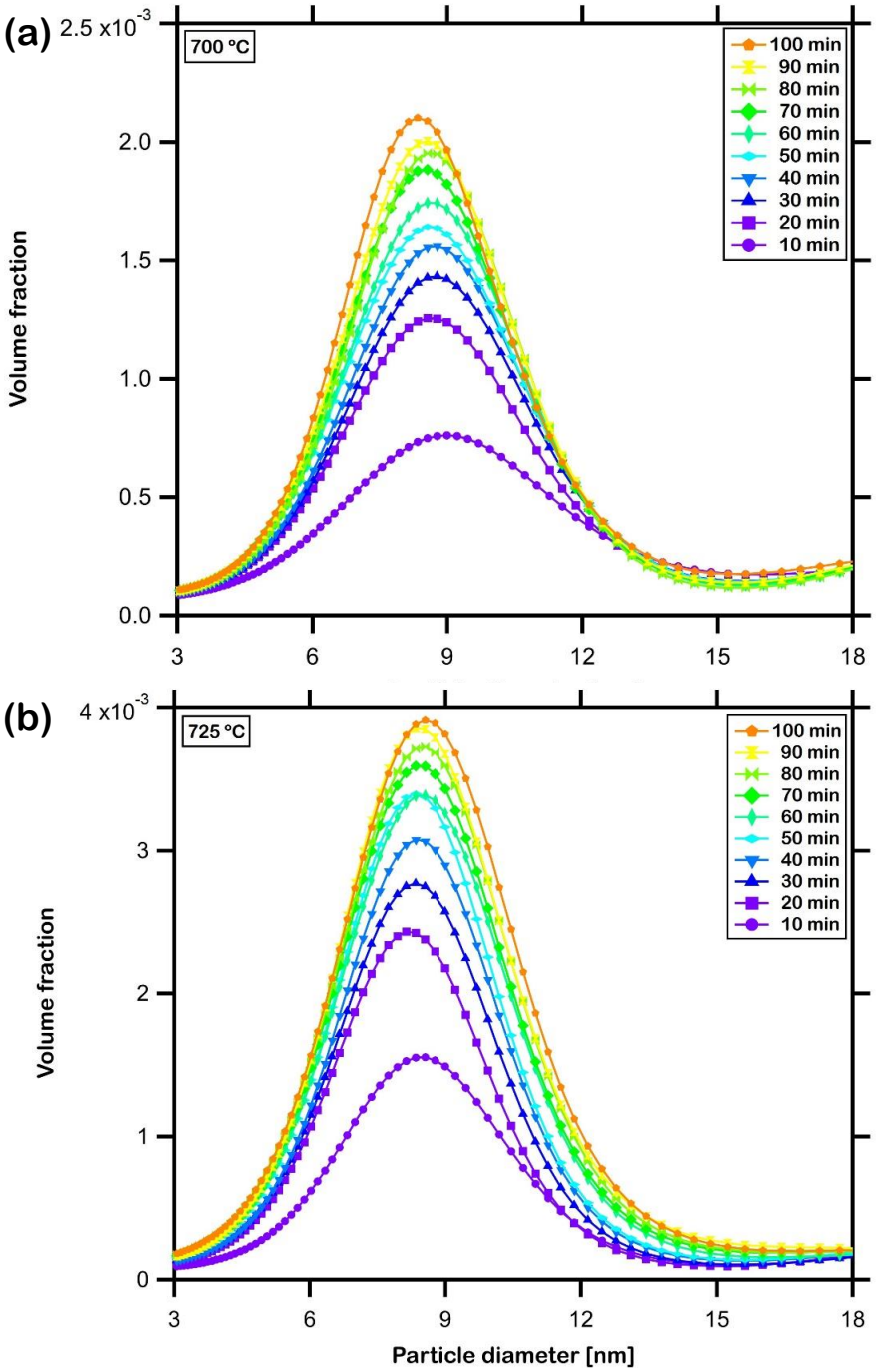

Figure 52: Distribution of the volume fraction of $(Fe,Cr)_{23}C_6$ crystals of various sizes estimated by fitting *in-situ* small angle neutron scattering intensity measured during isothermal annealing of the sintered sample at (a) 700 °C and (b) 725 °C for 100 min. The crystals exhibit a range of sizes from 3 to 18 nm and the highest abundance of those with size 9 nm

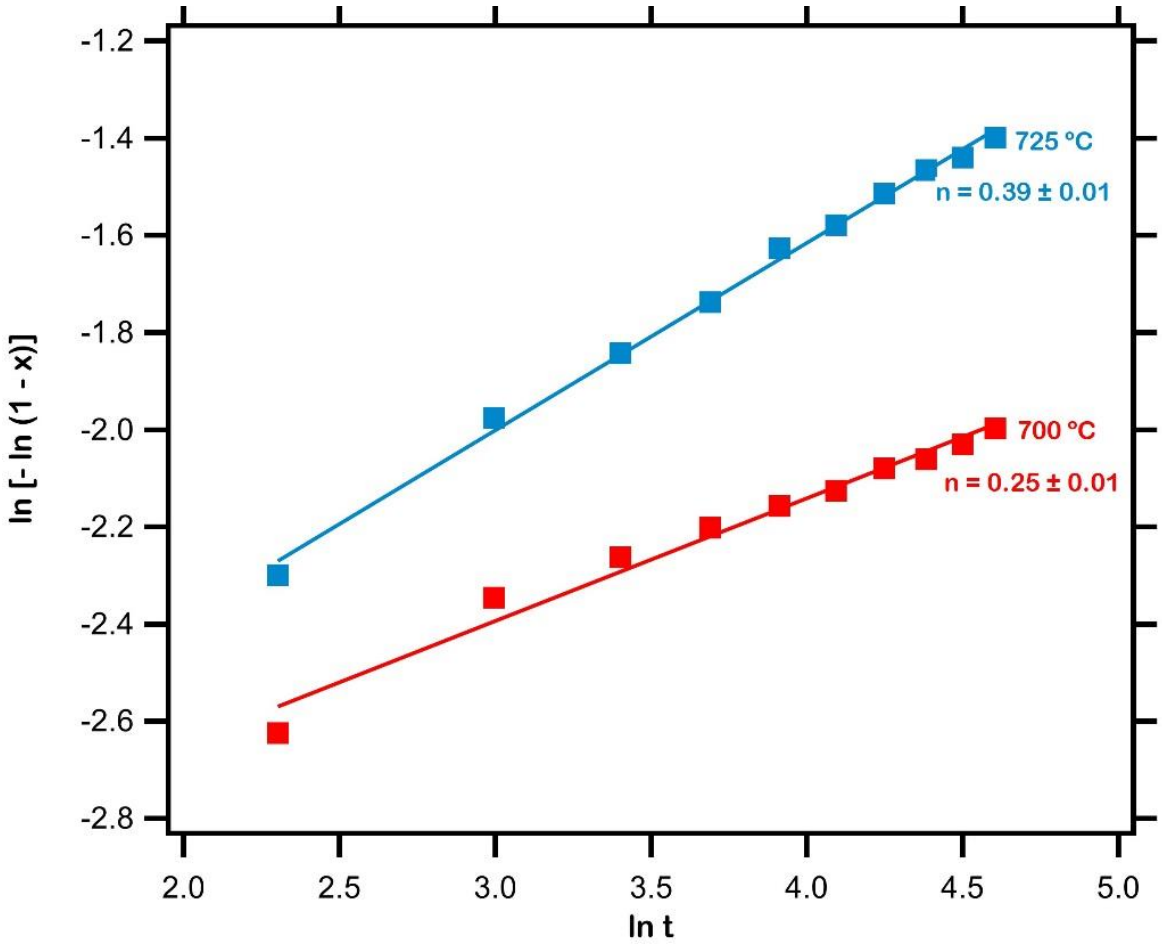

Figure 53: Plots of ln[-ln(1-x)] versus ln$t$ for the evolution of $(Fe,Cr)_{23}C_6$ crystals during isothermal annealing of $Fe_{48}Cr_{15}Mo_{14}Y_2C_{15}B_6$ metallic glass. The estimated Avrami exponents, 0.25 ± 0.01 and 0.39 ± 0.01 at 700 °C and 725 °C respectively, established that crystals evolved from pre-existing nuclei

where x is the total volume fraction of crystals, n is the Avrami exponent, t (min) is the isothermal annealing time and k is the reaction rate constant. The plots of ln[-ln(1-x)] with respect to ln$t$ are presented in Fig. 53. The Avrami exponent n was estimated, by linear fit to the plots, to be 0.25 ± 0.01 and 0.39 ± 0.01 at 700 °C and 725 °C respectively.

The Avrami exponent is representative of the nucleation behavior prevalent during the progress of crystallization in metallic glass [3]. In particular, a value of n less than 1.5, as in the present case, shows that the evolution of $(Fe,Cr)_{23}C_6$ crystals within the iron

based metallic glass during isothermal annealing both at 700 °C as well as 725 °C occurs from pre-existing nuclei [4, 5]. It was observed from Fig. 49 that during annealing from ambient up to 700 °C and 725 °C the nuclei developed in the metallic glass matrix resulted in the increase in scattering intensity. Thus at the beginning of isothermal annealing at these temperatures nuclei of $(Fe,Cr)_{23}C_6$ are pre-existent. With the progress of annealing time, these pre-existing nuclei grow into well developed crystals, as manifested by the estimated values of the Avrami exponent.

Chapter VI

Conclusions

Analysis of the thermal responses of $Fe_{48}Cr_{15}Mo_{14}Y_2C_{15}B_6$ metallic glass powder has resulted in the establishment of the densification behavior, oxidation kinetics and crystallization kinetics in this thesis. The conclusions deduced from both are summarized as follows.

1 Densification behavior

Normal distribution in the size of particles led to efficient densification with the larger particles forming a continuous network while the smaller particles saturated the intermediate voids. Large densification occurred during spark plasma sintering in the supercooled liquid region primarily due a decrease in the viscosity of the material. During isochronal sintering, densification occurred in two stages. During Stage I the samples were fully amorphous up to the temperature of peak densification rate while in Stage II it was partially crystalline. The shrinkage of the powder compact analyzed in the temperature interval between onset densification and peak densification rate exhibited an activation energy of $94.0 \pm 0.2\,\mathrm{kJ\,mol^{-1}}$

at a heating rate of 25 °C min^{-1} which is of the order of magnitude as that of the viscosity measured by three point bending of the same material. The reduction in the value resulted from a difference in the driving forces in the two measurement techniques. An increase in the isochronal heating rate during spark plasma sintering resulted in a decrease in the temperature of peak densification rate while the peak densification rate increased. This was a result of the reduction in activation energy from 76.2 ± 0.4 through 64.0 ± 0.9 to 55.2 ± 1.0 kJ mol^{-1} due to an increase in isochronal heating rate from 50 through 100 to 150 °C min^{-1}. This reduction occurred due a directional structural relaxation (DSR) in the metallic glass. Under the aegis of the unified Arrhenius and DSR models, the functional relationship between the activation energy and heating rate was established as Q = (-22.8 ± 0.4)lnc + 73.7 kJ mol^{-1}.

An increase in the uniaxial compressive pressure from 20 to 70 MPa resulted in an increase in the final fractional density of the sintered compacts from 0.80 to 0.98. The geometry of the powder particles evolved with sintering from spherical to polyhedral in shape. The macroscopic applied pressure was increased by 3 orders of magnitude to microscopic interparticle contact pressure of 10 GPa which resulted in micro-viscous flow deformation of the particles. The total deformation of the particles was estimated to be up to 18 µm under the framework of deformation of single particles between two flat plates. The total deformation was utilized to theoretically calculate the fractional density which exhibited a close agreement with the experimentally observed ones. The limitations of this model lie in the underestimation of the densification of the compact due to consideration of only the

viscous flow deformation. Overestimation of density also occurs on the assumption that densification can proceed unimpeded in spite of a restriction from adjoining particles and die walls.

2 Oxidation behavior

Oxidation of $Fe_{48}Cr_{15}Mo_{14}Y_2C_{15}B_6$ metallic glass powder at 580 °C for 720 min and 650 °C for 300 min results primarily in the formation of polycrystalline Fe_2O_3. This oxide grows over the entire surface of the powder particles as a uniform shell which further constitutes of multiple grains. The ultra-small angle X-ray scattering intensity acquired *in-situ* during isothermal oxidation and modelled based on this hierarchical structure of the oxide, enumerated the increase in thickness of the oxide with time, rapid initially which gradually decreased. The relative gain in mass due to oxidation computed theoretically from this model, relatively underestimates that measured in practice owing to the distribution in size of the pristine particles. Overall, the results presented here establish the chemical identification, structural analysis and quantitative computation of isothermal oxidation in metallic glass powder. In the broad perspective, this manifests the potential to unfold new paradigms of research on interfacial reactions in powder materials at elevated temperatures and develop predictive analytical capabilities built on complementary *ex-situ* and *in-operando* scattering techniques.

3 Crystallization kinetics

Thermal analysis of the $Fe_{48}Cr_{15}Mo_{14}Y_2C_{15}B_6$ metallic glass powder exhibited that the isochronal crystallization in this material consisted of four exothermic transformations occurring over a temperature interval from 900 to 1100 K. These transformations, Exo 1, Exo 2, Exo 3 and Exo 4 were identified to be $Fe_{18}Cr_6Mo_5$, $(Fe, Cr)_{23}(C, B)_6$, $(Fe, Cr)_7C_3$ and Fe_3Mo_3C, respectively. The transformations involve a strong kinetic effect as exhibited by the progressive increase in the onset crystallization temperature, T_o and the enthalpy of transformation with increase in heating rate from 10 to 40 $K\,min^{-1}$. Kissinger analysis of the activation energies of transformations from the deconvoluted Gaussian profiles showed that the energy barrier for Exo 1 is the lowest while that of Exo 2 is highest. The crystallized fraction of the transformations increased in a sigmoidal fashion indicating the mechanism of nucleation and growth. It was established from the estimated local Avrami exponents of the transformations that the nucleation occurred at a decreasing rate and growth of crystals occurred from the pre-existing nuclei. The conclusions drawn from the estimation of local Avrami exponents was found to be identical for the utilization of both the crystallization onset temperature as well as half of the peak crystallization temperature.

Bibliography

[1] LH Liu, C Yang, YG Yao, F Wang, WW Zhang, Y Long, and YY Li. Densification mechanism of ti-based metallic glass powders during spark plasma sintering process. *Intermetallics*, 66:1–7, 2015.

[2] HA Wriedt. The fe-o (iron-oxygen) system. *Journal of Phase Equilibria*, 12(2):170–200, 1991.

[3] Parthiban Ramasamy, Mihai Stoica, AH Taghvaei, KG Prashanth, Ravi Kumar, and Jürgen Eckert. Kinetic analysis of the non-isothermal crystallization process, magnetic and mechanical properties of fecobsinb and fecobsinbcu bulk metallic glasses. *Journal of Applied Physics*, 119(7):073908, 2016.

[4] Yifang Ouyang, Luyang Wang, Hongmei Chen, Xiaoying Cheng, Xiaping Zhong, and Yuanping Feng. The formation and crystallization of amorphous al 65 fe 20 zr 15. *Journal of Non-crystalline Solids*, 354(52):5555–5558, 2008.

[5] C Peng, ZH Chen, XY Zhao, AL Zhang, LK Zhang, and D Chen. Crystallization kinetics of zr 60 cu 25 fe 5 al 10 bulk metallic glass. *Journal of Non-Crystalline Solids*, 405:7–11, 2014.

[6] Maria Jazmin Duarte, Aleksander Kostka, Daniel Crespo, Jose Antonio Jimenez, A C Dippel, Frank Uwe Renner, and Gerhard Dehm. Kinetics and crystallization path of a fe-based metallic glass alloy. *Acta Materialia*, 127:341–350, 2017.

[7] Shlomo Alexander. Amorphous solids: their structure, lattice dynamics and elasticity. *Physics reports*, 296(2-4):65–236, 1998.

[8] Aamer Ali Shah, Fariha Hasan, Abdul Hameed, and Safia Ahmed. Biological degradation of plastics: a comprehensive review. *Biotechnology advances*, 26(3):246–265, 2008.

[9] Edward D Weil and Sergei Levchik. A review of current flame retardant systems for epoxy resins. *Journal of fire sciences*, 22(1):25–40, 2004.

[10] D Porter, E Metcalfe, and MJK Thomas. Nanocomposite fire retardantsa review. *Fire and Materials*, 24(1):45–52, 2000.

[11] Irving Friedman and William Long. Hydration rate of obsidian. *Science*, 191(4225):347–352, 1976.

[12] W Klement, RH Willens, and POL Duwez. Non-crystalline structure in solidified gold–silicon alloys. *Nature*, 187(4740):869–870, 1960.

[13] HS Chen and D Turnbull. Formation, stability and structure of palladium-silicon based alloy glasses. *Acta Metallurgica*, 17(8):1021–1031, 1969.

[14] HW Kui, Al L Greer, and D Turnbull. Formation of bulk metallic glass by fluxing. *Applied Physics Letters*, 45(6):615–616, 1984.

[15] YQ Cheng and E Ma. Atomic-level structure and structure–property relationship in metallic glasses. *Progress in materials science*, 56(4):379–473, 2011.

[16] Atakan Peker and William L Johnson. A highly processable metallic glass: Zr41. 2ti13. 8cu12. 5ni10. 0be22. 5. *Applied Physics Letters*, 63(17):2342–2344, 1993.

[17] Akihisa Inoue, Nobuyuki Nishiyama, and Hisamichi Kimura. Preparation and thermal stability of bulk amorphous pd40cu30ni10p20 alloy cylinder of 72 mm in diameter. *Materials Transactions, JIM*, 38(2):179–183, 1997.

[18] Tao Zhang and Akihisa Inoue. Bulk glassy alloys with low liquidus temperature in pt-cu-p system. *Materials Transactions*, 44(6):1143–1146, 2003.

[19] Tao Zhang and Akihisa Inoue. Ti-based amorphous alloys with a large supercooled liquid region. *Materials Science and Engineering: A*, 304:771–774, 2001.

[20] Tao Zhang and Akihisa Inoue. New bulk glassy ni-based alloys with high strength of 3000 mpa. *Materials Transactions*, 43(4):708–711, 2002.

[21] Ran Li, Shujie Pang, Chaoli Ma, and Tao Zhang. Influence of similar atom substitution on glass formation in (la–ce)–al–co bulk metallic glasses. *Acta Materialia*, 55(11):3719–3726, 2007.

[22] Akihisa Inoue, Akira Takeuchi, and Tao Zhang. Ferromagnetic bulk amorphous alloys. *Metallurgical and Materials Transactions A*, 29(7):1779–1793, 1998.

[23] Akihisa Inoue and Jin Seon Gook. Fe-based ferromagnetic glassy alloys with wide supercooled liquid region. *Materials Transactions, JIM*, 36(9):1180–1183, 1995.

[24] V Ponnambalam, S Joseph Poon, and Gary J Shiflet. Fe-based bulk metallic glasses with diameter thickness larger than one centimeter. *Journal of Materials Research*, 19(5):1320–1323, 2004.

[25] Kenji Amiya and Akihisa Inoue. Fe-(cr, mo)-(c, b)-tm bulk metallic glasses with high strength and high glass-forming ability. *Materials Transactions*, 47(6):1615–1618, 2006.

[26] Baolong Shen and Akihisa Inoue. Soft magnetic properties of bulk nanocrystalline fe–co–b–si–nb–cu alloy with high saturated magnetization of 1.35 t. *Journal of Materials Research*, 19(9):2549–2552, 2004.

[27] GC Lavorato, G Fiore, A Castellero, M Baricco, and JA Moya. Preparation and characterization of fe-based bulk metallic glasses in plate form. *Physica B: Condensed Matter*, 407(16):3192–3195, 2012.

[28] Z Zhou, L Wang, DY He, FC Wang, and YB Liu. Microstructure and wear resistance of fe-based amorphous metallic coatings prepared by hvof thermal spraying. *Journal of Thermal Spray Technology*, 19(6):1287–1293, 2010.

[29] C Zhang, L Liu, KC Chan, Q Chen, and CY Tang. Wear behavior of hvof-sprayed fe-based amorphous coatings. *Intermetallics*, 29:80–85, 2012.

[30] Dong Wang, Teilin Shi, Jie Pan, Guanglan Liao, Zirong Tang, and Lin Liu. Finite element simulation and experimental investigation of forming micro-gear with zr–cu–ni–al bulk metallic glass. *Journal of Materials Processing Technology*, 210(4):684–688, 2010.

[31] Z Zhou, L Wang, FC Wang, HF Zhang, YB Liu, and SH Xu. Formation and corrosion behavior of fe-based amorphous metallic coatings by hvof thermal spraying. *Surface and Coatings Technology*, 204(5):563–570, 2009.

[32] LS Garca-Coln, LF Del Castillo, and Patricia Goldstein. Theoretical basis for the vogel-fulcher-tammann equation. *Physical Review B*, 40(10):7040, 1989.

[33] VA Khonik. The kinetics of irreversible structural relaxation and homogeneous plastic flow of metallic glasses. *physica status solidi (a)*, 177(1):173–189, 2000.

[34] Randall M German. Powder injection molding. 1990.

[35] Mark Telford. The case for bulk metallic glass. *Materials Today*, 7(3):36–43, 2004.

[36] A Lindsay Greer. Metallic glasses on the threshold. *Materials Today*, 12(1-2):14–22, 2009.

[37] Eugen Axinte. Metallic glasses from alchemy to pure science: Present and future of design, processing and applications of glassy metals. *Materials & Design*, 35:518–556, 2012.

[38] Herbert Gleiter. Our thoughts are ours, their ends none of our own: are there ways to

synthesize materials beyond the limitations of today? *Acta Materialia*, 56(19):5875–5893, 2008.

[39] Tanaji Paul, Archana Loganathan, Arvind Agarwal, and Sandip P Harimkar. Kinetics of isochronal crystallization in a fe-based amorphous alloy. *Journal of Alloys and Compounds*, 753:679–687, 2018.

[40] YQ Cheng and E Ma. Atomic-level structure and structure–property relationship in metallic glasses. *Progress in Materials Science*, 56(4):379–473, 2011.

[41] BA Sun and WH Wang. The fracture of bulk metallic glasses. *Progress in Materials Science*, 74:211–307, 2015.

[42] A Reza Yavari, JJ Lewandowski, and J Eckert. Mechanical properties of bulk metallic glasses. *MRS Bulletin*, 32(8):635–638, 2007.

[43] Morgana Martin Trexler and Naresh N Thadhani. Mechanical properties of bulk metallic glasses. *Progress in Materials Science*, 55(8):759–839, 2010.

[44] Thierry Gloriant. Microhardness and abrasive wear resistance of metallic glasses and nanostructured composite materials. *Journal of Non-crystalline Solids*, 316(1):96–103, 2003.

[45] Xiulin Ji, Hui Wang, Yayun Bao, and Dingcong Zheng. Wear resistance of cuzr-based amorphous-forming alloys against bearing steel in 3.5% nacl solution. *Philosophical Magazine*, 97(32):3042–3054, 2017.

[46] Ch Hausleitner and I Turek. Structural, electronic, and magnetic properties of metallic glasses. *Journal of Non-crystalline solids*, 156:210–218, 1993.

[47] Giselher Herzer. Modern soft magnets: Amorphous and nanocrystalline materials. *Acta Materialia*, 61(3):718–734, 2013.

[48] C Suryanarayana and A Inoue. Iron-based bulk metallic glasses. *International Materials Reviews*, 58(3):131–166, 2013.

[49] Baran Sarac, Yurii P Ivanov, Andrey Chuvilin, Thomas Schöberl, Mihai Stoica, Zaoli Zhang, and Jürgen Eckert. Origin of large plasticity and multiscale effects in iron-based metallic glasses. *Nature Communications*, 9(1):1333, 2018.

[50] GC Lavorato, G Fiore, A Castellero, M Baricco, and JA Moya. Preparation and characterization of fe-based bulk metallic glasses in plate form. *Physica B: Condensed Matter*, 407(16):3192–3195, 2012.

[51] Ashish Singh, Tanaji Paul, Shravana Katakam, Narendra B Dahotre, and Sandip P Harimkar. In situ nanocrystallization-induced hardening of amorphous alloy matrix composites consolidated by spark plasma sintering. *JOM*, 68(7):1932–1937, 2016.

[52] Jun Shen, Qingjun Chen, Jianfei Sun, Hongbo Fan, and Gang Wang. Exceptionally high glass-forming ability of an fecocrmocby alloy. *Applied Physics Letters*, 86(15):151907, 2005.

[53] AL Greer, KL Rutherford, and IM Hutchings. Wear resistance of amorphous alloys and related materials. *International Materials Reviews*, 47(2):87–112, 2002.

[54] Shravana Katakam and Narendra Dahotre. Laser patterning of fe–si–b amorphous ribbons in magnetic field. *Applied Physics A*, 117(3):1241–1247, 2014.

[55] Chih Yuan Lin, Hung Yu Tien, and Tsung Shune Chin. Soft magnetic ternary iron-boron-based bulk metallic glasses. *Applied Physics Letters*, 86(16):162501, 2005.

[56] Ajay Gupta. Nanocrystalline soft-magnetic alloys produced by controlled crystallization of amorphous alloys. *Proceedings-Indian National Science Academy Part A*, 67(1):31–46, 2001.

[57] XP Nie, XH Yang, LY Chen, KB Yeap, KY Zeng, D Li, JS Pan, XD Wang, QP Cao, SQ Ding, et al. The effect of oxidation on the corrosion resistance and mechanical properties of a zr-based metallic glass. *Corrosion Science*, 53(11):3557–3565, 2011.

[58] Tae-Hwan Noh and Wan-Hee Jang. Effects of surface oxidation on magnetic properties of amorphous alloy for choke core use. *IEEE Transactions on Magnetics*, 35(5):3388–3390, 1999.

[59] Shu-lan Zhang, He-ping Liu, and Xiao-tong Fu. Oxidation behavior of fe-based amorphous ribbons. *Journal of Iron and Steel Research, International*, 23(11):1219–1225, 2016.

[60] Jing Pang, Keqiang Qiu, Chengjuan Wang, Dongpeng Wang, Anding Wang, Chuntao Chang, Xinmin Wang, and Chain-Tsuan Liu. Oxidation and refreshing behaviors of p-containing fe-based amorphous ribbons. *Journal of Non-Crystalline Solids*, 471:137–141, 2017.

[61] W Kai, TH Ho, HH Hsieh, YR Chen, DC Qiao, F Jiang, G Fan, and PK Liaw. Oxidation behavior of cuzr-based glassy alloys at 400 c to 500 c in dry air. *Metallurgical and Materials Transactions A*, 39(8):1838–1846, 2008.

[62] W Kai, PC Lin, WS Chen, CP Chuang, PK Liaw, HH Huang, and HH Hsieh. Air-oxidation of a zr50cu43al7 bulk metallic glass at 400–500 c. *Corrosion Science*, 64:98–104, 2012.

[63] Hiromi Yamashita, Masahito Yoshikawa, Takuzo Funabiki, and Satohiro Yoshida. Catalysis by amorphous metal alloys. part 6.-factors controlling the activity of skeletal nickel catalysts prepared from amorphous and crystalline ni–zr powder alloys. *Journal of the Chemical Society, Faraday Transactions 1: Physical Chemistry in Condensed Phases*, 83(9):2883–2893, 1987.

[64] SJ Kang, KT Rittgen, SG Kwan, HW Park, R Bennewitz, and A Caron. Importance of surface oxide for the tribology of a zr-based metallic glass. *Friction*, 5(1):115–122, 2017.

[65] Kun Zhou, Shujie Pang, Chen Chen, Ying Liu, Wei Yang, and Tao Zhang. Enhanced wear resistance of zr-based bulk metallic glass by thermal oxidation treatment. *Materials Transactions*, 58(3):520–523, 2017.

[66] DV Louzguine-Luzgin, M Ito, SV Ketov, AS Trifonov, J Jiang, CL Chen, and K Nakajima. Exceptionally high nanoscale wear resistance of a cu47zr45al8 metallic glass with native and artificially grown oxide. *Intermetallics*, 93:312–317, 2018.

[67] Tanaji Paul, S Habib Alavi, Sourabh Biswas, and Sandip P Harimkar. Microstructure and wear behavior of laser clad multi-layered fe-based amorphous coatings on steel substrates. *Lasers in Manufacturing and Materials Processing*, 2(4):231–241, 2015.

[68] Himabindu Kasturi, Tanaji Paul, Sourabh Biswas, S Habib Alavi, and Sandip P Harimkar. Sliding wear behavior of spark-plasma-sintered fe-based amorphous alloy coatings on cu-ni alloy. *Journal of Materials Engineering and Performance*, 27(7):3629–3635, 2018.

[69] Tanaji Paul and Sandip P Harimkar. Initial stage densification during spark plasma sintering of fe-based amorphous alloy powder: Analysis of viscous flow. *Journal of Applied Physics*, 120(13):134901, 2016.

[70] Tanaji Paul, Niraj Chawake, Ravi Sankar Kottada, and Sandip P Harimkar. Pressure controlled micro-viscous deformation assisted spark plasma sintering of fe-based bulk amorphous alloy. *Journal of Alloys and Compounds*, 738:10–15, 2018.

[71] Jan Schroers. The superplastic forming of bulk metallic glasses. *JOM*, 57(5):35–39, 2005.

[72] Tanaji Paul and Sandip P Harimkar. Viscous flow activation energy adaptation by isochronal spark plasma sintering. *Scripta Materialia*, 126:37–40, 2017.

[73] Ning Li, Wen Chen, and Lin Liu. Thermoplastic micro-forming of bulk metallic glasses: a review. *JOM*, 68(4):1246–1261, 2016.

[74] Wei-Hua Wang, Chuang Dong, and CH Shek. Bulk metallic glasses. *Materials Science and Engineering: R: Reports*, 44(2-3):45–89, 2004.

[75] K Mondal, UK Chatterjee, and BS Murty. Oxidation behavior of multicomponent zr-based amorphous alloys. *Journal of Alloys and Compounds*, 433(1-2):162–170, 2007.

[76] Huei-Sen Wang, Wei-Hau Li, Mei-Hui Wu, Hou-Guang Chen, Jason Shian-Ching Jang, and Dong-Yih Lin. The oxidation behavior of a novel ni-free zr–cu-based bulk metallic glass composite in the supercooled liquid and crystallization states. *Intermetallics*, 53:34–39, 2014.

[77] W Kai, IF Ren, RF Wang, PC Kao, and CT Liu. The oxidation behavior of an fe61b15zr8mo7co5y2cr2 bulk metallic glass at 650 c in various oxygen-containing environments. *Intermetallics*, 17(3):165–168, 2009.

[78] HMMN Hennayaka, Ho Seong Lee, and Seonghoon Yi. Surface oxidation of the fe based amorphous ribbon annealed at temperatures below the glass transition temperature. *Journal of Alloys and Compounds*, 618:269–279, 2015.

[79] Yonglong Hu, Wenhuan Cao, and Chanhung Shek. The corrosion and oxidation behavior of zr-based metallic glasses. *Journal of Materials Research*, 29(11):1248–1255, 2014.

[80] Jingpeng Li, Aiquan Jiao, Shuo Chen, Zhengzong Wu, Enbo Xu, and Zhengyu Jin. Application of the small-angle x-ray scattering technique for structural analysis studies: A review. *Journal of Molecular Structure*, 1165:391–400, 2018.

[81] Peter Fratzl. Small-angle scattering in materials science-a short review of applications in alloys, ceramics and composite materials. *Journal of Applied Crystallography*, 36(3-1):397–404, 2003.

[82] Jan Ilavsky, Fan Zhang, Ross N Andrews, Ivan Kuzmenko, Pete R Jemian, Lyle E Levine, and Andrew J Allen. Development of combined microstructure and structure characterization facility for *in situ* and *operando* studies at the advanced photon source. *Journal of Applied Crystallography*, 51(3):867–882, 2018.

[83] Jan Ilavsky, Fan Zhang, AJ Allen, LE Levine, PR Jemian, and GG Long. Ultra-small-angle x-ray scattering instrument at the advanced photon source: History, recent development, and current status. *Metallurgical and Materials Transactions A*, 44(1):68–76, 2013.

[84] NV Chirikov and YA Skakov. Analysis of concentration inhomogeneities of amorphous metal-alloys with the aid of small-angle scattering of x-rays and neutrons. *Industrial Laboratory*, 54(6):633–640, 1988.

[85] Fan Zhang, Lyle E Levine, Andrew J Allen, Mark R Stoudt, Greta Lindwall, Eric A Lass, Maureen E Williams, Yaakov Idell, and Carelyn E Campbell. Effect of heat treatment on the microstructural evolution of a nickel-based superalloy additive-manufactured by laser powder bed fusion. *Acta Materialia*, 152:200–214, 2018.

[86] Alexis Deschamps and Frederic De Geuser. Quantitative characterization of precipi-

tate microstructures in metallic alloys using small-angle scattering. *Metallurgical and Materials Transactions A*, 44(1):77–86, 2013.

[87] Fan Zhang, Lyle E Levine, Andrew J Allen, Carelyn E Campbell, Adam A Creuziger, Nataliya Kazantseva, and Jan Ilavsky. In situ structural characterization of ageing kinetics in aluminum alloy 2024 across angstrom-to-micrometer length scales. *Acta Materialia*, 111:385–398, 2016.

[88] Von Otto Glatter and Otto Kratky. *Small angle x-ray scattering*. London: Academic Press Inc. Ltd., 1982.

[89] Elina Tjioe and William T Heller. Ornl_sas: software for calculation of small-angle scattering intensities of proteins and protein complexes. *Journal of Applied Crystallography*, 40(4):782–785, 2007.

[90] Jan Ilavsky and Peter R Jemian. Irena: tool suite for modeling and analysis of small-angle scattering. *Journal of Applied Crystallography*, 42(2):347–353, 2009.

[91] H Liebermann. H. and graham, cd. *IEEE Trans. Mag., MAG-12*, 921, 1976.

[92] Susanne Schneider. Bulk metallic glasses. *Journal of Physics: Condensed Matter*, 13(34):7723, 2001.

[93] Mark Telford. The case for bulk metallic glass. *Materials today*, 7(3):36–43, 2004.

[94] T Egami and Y_ Waseda. Atomic size effect on the formability of metallic glasses. *Journal of Non-Crystalline Solids*, 64(1-2):113–134, 1984.

[95] Akihisa Inoue, Akira Takeuchi, and Tao Zhang. Ferromagnetic bulk amorphous alloys. *Metallurgical and Materials Transactions A*, 29(7):1779–1793, 1998.

[96] A Lindsay Greer. Metallic glasses. *Science*, 267(5206):1947–1953, 1995.

[97] Tanya Aycan Baser and Marcello Baricco. Fe-based bulk metallic glasses with y addition. *Journal of Alloys and Compounds*, 434:176–179, 2007.

[98] Jong Hyun Na, Marios D Demetriou, and William L Johnson. Fragility of iron-based glasses. *Applied Physics Letters*, 99(16):161902, 2011.

[99] James P Kelly, Seth M Fuller, Kyungah Seo, Ekaterina Novitskaya, Veronica Eliasson, Andrea M Hodge, and Olivia A Graeve. Designing in situ and ex situ bulk metallic glass composites via spark plasma sintering in the super cooled liquid state. *Materials & Design*, 93:26–38, 2016.

[100] Yi Qun Gao, Wego Wang, Fu Qian Zheng, and Xiong Liu. On the crystallization kinetics of pd80b4si16 glass. *Journal of Non-crystalline Solids*, 81(1-2):135–139, 1986.

[101] JS Blázquez, JM Borrego, CF Conde, A Conde, and S Lozano-Pérez. Extension of the classical theory of crystallization to non-isothermal regimes: Application to nanocrystallization processes. *Journal of Alloys and Compounds*, 544:73–81, 2012.

[102] OA Graeve, MS Saterlie, R Kanakala, S Diaz de la Torre, and JC Farmer. The kinetics of devitrification of amorphous alloys: The time–temperature–crystallinity diagram describing the spark plasma sintering of fe-based metallic glasses. *Scripta Materialia*, 69(2):143–148, 2013.

[103] Mayuresh K Shete, I Singh, R Narasimhan, and U Ramamurty. Effect of strain hardening and volume fraction of crystalline phase on strength and ductility of bulk metallic glass composites. *Scripta Materialia*, 124:51–55, 2016.

[104] Ashish Singh, Shravana Katakam, Jan Ilavsky, Narendra B Dahotre, and Sandip P Harimkar. Nanocrystallization in spark plasma sintered fe48cr15mo14y2c15b6 bulk amorphous alloy. *Journal of Applied Physics*, 114(5):054903, 2013.

[105] ASTM-B962. Standard test methods for density of compacted or sintered powder metallurgy (pm) products using archimedes principle. 962, 2008.

[106] ASTM-B311. Standard test method for density of powder metallurgy (pm) materials containing less than two percent porosity. 962, 2008.

[107] Jan Ilavsky, Pete R Jemian, Andrew J Allen, Fan Zhang, Lyle E Levine, and Gabrielle G Long. Ultra-small-angle x-ray scattering at the advanced photon source. *Journal of Applied Crystallography*, 42(3):469–479, 2009.

[108] George D Wignall, Kenneth C Littrell, William T Heller, Yuri B Melnichenko, Kathy M Bailey, Gary W Lynn, Dean A Myles, Volker S Urban, Michelle V Buchanan, Douglas L Selby, et al. The 40 m general purpose small-angle neutron scattering instrument at oak ridge national laboratory. *Journal of Applied Crystallography*, 45(5):990–998, 2012.

[109] Kevin D Berry, Katherine M Bailey, Justin Beal, Yacouba Diawara, Loren Funk, J Steve Hicks, Amy Black Jones, Kenneth C Littrell, SV Pingali, PR Summers, et al.

Characterization of the neutron detector upgrade to the gp-sans and bio-sans instruments at hfir. *Nuclear Instruments and Methods in Physics Research Section A: Accelerators, Spectrometers, Detectors and Associated Equipment*, 693:179–185, 2012.

[110] RM German. Sintering densification for powder mixtures of varying distribution widths. *Acta Metallurgica et Materialia*, 40(9):2085–2089, 1992.

[111] BR Patterson, VD Parkhe, and JA Griffin. Effect of particle size distribution on sintering. In *Sintering 85*, pages 43–51. Springer, 1987.

[112] A Basu, AN Samant, SP Harimkar, J Dutta Majumdar, I Manna, and Narendra B Dahotre. Laser surface coating of fe–cr–mo–y–b–c bulk metallic glass composition on aisi 4140 steel. *Surface and Coatings Technology*, 202(12):2623–2631, 2008.

[113] GC Kuczynski and I Zaplatynskyj. Sintering of glass. *Journal of the American Ceramic Society*, 39(10):349–350, 1956.

[114] GC Kuczynski. Study of the sintering of glass. *Journal of Applied Physics*, 20(12):1160–1163, 1949.

[115] VV Dabhade, TR Rama Mohan, and P Ramakrishnan. Viscous flow during sintering of attrition milled nanocrystalline titanium powders. *Materials research bulletin*, 42(7):1262–1268, 2007.

[116] Ivan B Cutler. Sintering of glass powders during constant rates of heating. *Journal of the American Ceramic Society*, 52(1):14–17, 1969.

[117] Wayne S Young and Ivan B Cutler. Initial sintering with constant rates of heating. *Journal of the American ceramic Society*, 53(12):659–663, 1970.

[118] Yunzhuo Lu, Yongjiang Huang, Jun Shen, Xing Lu, Zuoxiang Qin, and Zhihua Zhang. Effect of co addition on the shear viscosity of fe-based bulk metallic glasses. *Journal of Non-Crystalline Solids*, 403:62–66, 2014.

[119] Sandip P Harimkar, Sameer R Paital, Ashish Singh, Robert Aalund, and Narendra B Dahotre. Microstructure and properties of spark plasma sintered fe–cr–mo–y–b–c bulk metallic glass. *Journal of Non-Crystalline Solids*, 355(43-44):2179–2182, 2009.

[120] B Movahedi, MH Enayati, and CC Wong. On the crystallization behavior of amorphous fe–cr–mo–b–p–si–c powder prepared by mechanical alloying. *Materials letters*, 64(9):1055–1058, 2010.

[121] VA Khonik, VA Mikhailov, and IA Safonov. Non-isothermal creep of metallic glasses. *Scripta materialia*, 37(7), 1997.

[122] AV Lysenko, SA Lyakhov, VA Khonik, and Yazvitskiĭ. Shear viscosity of the pd 40 cu 40 p 20 metallic glass under conditions of isochronous heating below the glass transition temperature.

[123] K Csach, OP Bobrov, VA Khonik, SA Lyakhov, and Kazuo Kitagawa. Relationship between the shear viscosity and heating rate of metallic glasses below t g. *Physical Review B*, 73(9):092107, 2006.

[124] R Busch, W Liu, and WL Johnson. Thermodynamics and kinetics of the mg 65 cu 25 y 10 bulk metallic glass forming liquid. *Journal of Applied Physics*, 83(8):4134–4141, 1998.

[125] DV Louzguine-Luzgin, AI Bazlov, SV Ketov, AL Greer, and A Inoue. Crystal growth limitation as a critical factor for formation of fe-based bulk metallic glasses. *Acta Materialia*, 82:396–402, 2015.

[126] LH Liu, C Yang, YG Yao, F Wang, WW Zhang, Y Long, and YY Li. Densification mechanism of ti-based metallic glass powders during spark plasma sintering process. *Intermetallics*, 66:1–7, 2015.

[127] Tanaji Paul and Sandip P Harimkar. Prediction of heating rate controlled viscous flow activation energy during spark plasma sintering of amorphous alloy powders. *Journal of Physics D: Applied Physics*, 50(27):27LT01, 2017.

[128] ZA Munir, U Anselmi-Tamburini, and M Ohyanagi. The effect of electric field and pressure on the synthesis and consolidation of materials: A review of the spark plasma sintering method. *Journal of Materials Science*, 41(3):763–777, 2006.

[129] Michael Nöthe, Tobias Rasp, Torsten Kraft, and Bernd Kieback. Theory of sintering in presence of pressure and torque. *Journal of the American Ceramic Society*, 98(11):3453–3459, 2015.

[130] Randall M German. *Handbook of mathematical relations in particulate materials processing*, volume 3. John Wiley & Sons, 2009.

[131] Robert L Coble. Sintering crystalline solids. i. intermediate and final state diffusion models. *Journal of Applied Physics*, 32(5):787–792, 1961.

[132] Wei Ji, Sahibzada Shakir Rehman, Weimin Wang, Hao Wang, Yucheng Wang, Jinyong Zhang, Fan Zhang, and Zhengyi Fu. Sintering boron carbide ceramics without grain growth by plastic deformation as the dominant densification mechanism. *Scientific Reports*, 5:15827, 2015.

[133] Robert L Coble. Diffusion models for hot pressing with surface energy and pressure effects as driving forces. *Journal of Applied Physics*, 41(12):4798–4807, 1970.

[134] Bjoern Brandt and Torsten Rabe. Compilation and evaluation of the pressure-assisted master sintering surface for low-temperature cofired ceramics. *Journal of the American Ceramic Society*, 98(11):3503–3508, 2015.

[135] ASTM-E209. Standard practice for compression tests of metallic materials at elevated temperatures with conventional or rapid heating rates and strain rates. *Annual Book of ASTM Standards*, 03.01, 2010.

[136] N Yodoshi, R Yamada, A Kawasaki, and A Makino. Micro viscous flow processing of fe-based metallic glassy particles. *Journal of Alloys and Compounds*, 615:S61–S66, 2014.

[137] M Lakshmi Prasanna, Bhaskar Majumdar, VL Niranjani, and SV Kamat. Microstructure and mechanical properties of [(fe0. 5co0. 5) 0.75 b0. 2si0. 05] 96nb4 bulk metallic glass compacts. *Transactions of the Indian Institute of Metals*, 68(6):1033–1037, 2015.

[138] Cyril Stanley Smith. Some elementary principles of polycrystalline microstructure. *Metallurgical Reviews*, 9(1):1–48, 1964.

[139] Eduard Arzt, Michael F Ashby, and Kenneth Edwin Easterling. Practical applications of hotisostatic pressing diagrams: four case studies. *Metallurgical Transactions A*, 14(1):211–221, 1983.

[140] Wolfgang A Kaysser, M Asian, Eduard Arzt, Mirjana Mitkov, and Günther Petzow. Microstructural development and densification during hipping of ceramics and metals. *Powder Metallurgy*, 31(1):63–69, 1988.

[141] Tanaji Paul, Ashish Singh, and Sandip P Harimkar. Densification and crystallization in fe–based bulk amorphous alloy spark plasma sintered in the supercooled liquid region. *Advanced Engineering Materials*, 19(8), 2017.

[142] Bashir Ahmmad, Kwati Leonard, Md Shariful Islam, Junichi Kurawaki, Manickavachagam Muruganandham, Takahiro Ohkubo, and Yasushige Kuroda. Green synthesis of mesoporous hematite (α-fe2o3) nanoparticles and their photocatalytic activity. *Advanced Powder Technology*, 24(1):160–167, 2013.

[143] Liqiao Chen, Xianfeng Yang, Jian Chen, Jia Liu, Hao Wu, Hongquan Zhan, Chaolun Liang, and Mingmei Wu. Continuous shape-and spectroscopy-tuning of hematite nanocrystals. *Inorganic Chemistry*, 49(18):8411–8420, 2010.

[144] Jie-Feng Lu and Cho-Jen Tsai. Hydrothermal phase transformation of hematite to magnetite. *Nanoscale Research Letters*, 9(1):230, 2014.

[145] Harry F Rizzo. Oxidation of boron at temperatures between 400 and 1300 c in air. In *Boron Synthesis, Structure, and Properties*, pages 175–189. Springer, 1960.

[146] Wu Kai, IF Ren, PC Kao, RT Huang, and CT Liu. The oxidation behavior of an fe61b15zr8mo7co5y2cr2 bulk metallic glass at 550–700 c. *Intermetallics*, 17(4):205–210, 2009.

[147] W Kai, YH Wu, WS Chen, LW Tsay, HL Jia, and PK Liaw. Air-oxidation behavior of a [(fe50co50) 75b20si5] 96nb4 bulk metallic glass at 500–650 c. *Corrosion Science*, 66:26–32, 2013.

[148] YY Wang, ZH Ni, ZX Shen, HM Wang, and YH Wu. Interference enhancement of raman signal of graphene. *Applied Physics Letters*, 92(4):043121, 2008.

[149] Song-Lin Li, Hisao Miyazaki, Haisheng Song, Hiromi Kuramochi, Shu Nakaharai, and Kazuhito Tsukagoshi. Quantitative raman spectrum and reliable thickness identification for atomic layers on insulating substrates. *ACS Nano*, 6(8):7381–7388, 2012.

[150] Simon JA Pope and Yvonne D West. Comparison of the ft raman spectra of inorganic tetrahedral ions over the temperature range 77 to 473 k. *Spectrochimica Acta Part A: Molecular and Biomolecular Spectroscopy*, 51(12):2027–2037, 1995.

[151] Fred LaPlant, George Laurence, and Dor Ben-Amotz. Theoretical and experimental uncertainty in temperature measurement of materials by raman spectroscopy. *Applied Spectroscopy*, 50(8):1034–1038, 1996.

[152] C Ozge Topal, Susheng Tan, Hongbing Lu, Nicholas Leventis, and A Kaan Kalkan. Resonant two-photon oxidation in vanadium oxyhydrate nanowires above a threshold laser intensity. *The Journal of Physical Chemistry C*, 116(18):10186–10192, 2012.

[153] D. S. Sivia. *Elementary Scattering Theory: For X-ray and Neutron Users*. Oxford University Press, 2011.

[154] SD Imhoff, J Ilavsky, F Zhang, P Jemian, PG Evans, and JH Perepezko. Kinetic transition in the growth of al nanocrystals in al-sm alloys. *Journal of Applied Physics*, 111(6):063525, 2012.

[155] Heimo Schnablegger and Yashveer Singh. *The SAXS guide: getting acquainted with the principles*. Austria: Anton Paar GmbH, 2011.

[156] Ross N Andrews, Joseph Serio, Govindarajan Muralidharan, and Jan Ilavsky. An in situ usaxs–saxs–waxs study of precipitate size distribution evolution in a model ni-based alloy. *Journal of Applied Crystallography*, 50(3):734–740, 2017.

[157] B Movahedi, MH Enayati, and CC Wong. On the crystallization behavior of amorphous fe–cr–mo–b–p–si–c powder prepared by mechanical alloying. *Materials Letters*, 64(9):1055–1058, 2010.

[158] YH Zhang, YC Liu, ZM Gao, and DJ Wang. Study on crystallization of nanocrystalline/amorphous al-based alloy. *Journal of Alloys and Compounds*, 469(1-2):565–570, 2009.

[159] Yunzhuo Lu, Yongjiang Huang, Xing Lu, Zuoxiang Qin, and Jun Shen. Specific heat capacities of fe–co–cr–mo–c–b–y bulk metallic glasses and their correlation with glass-forming ability. *Materials Letters*, 143:191–193, 2015.

[160] TA Baser, M Baricco, S Enzo, G Vaughan, and AR Yavari. Analysis of crystallization behavior of fe 48 cr 15 mo 14 y 2 c 15 b 6 bulk metallic glass by synchrotron radiation. *Journal of Materials Research*, 23(8):2166–2173, 2008.

[161] Hung M Ha and Joe H Payer. Devitrification of fe-based amorphous metal sam 1651: a structural and compositional study. *Metallurgical and Materials Transactions A*, 40(11):2519–2529, 2009.

[162] Homer E Kissinger. Variation of peak temperature with heating rate in differential thermal analysis. *Journal of Research of the National Bureau of Standards*, 57(4):217–221, 1956.

[163] LH Kong, YL Gao, TT Song, G Wang, and QJ Zhai. Non-isothermal crystallization kinetics of fezrb amorphous alloy. *Thermochimica Acta*, 522(1):166–172, 2011.

[164] K Nakamura, K Katayama, and T Amano. Some aspects of nonisothermal crystallization of polymers. ii. consideration of the isokinetic condition. *Journal of Applied Polymer Science*, 17(4):1031–1041, 1973.

[165] Arun Pratap, Kirit N Lad, T Lilly Shanker Rao, Pinal Majmudar, and NS Saxena. Kinetics of crystallization of amorphous cu 50 ti 50 alloy. *Journal of Non-crystalline Solids*, 345:178–181, 2004.

[166] Pere Bruna, Eloi Pineda, Jose I Rojas, and Daniel Crespo. Phase-field modelling of microstructural evolution in primary crystallization. *Journal of Alloys and Compounds*, 483(1):645–649, 2009.

[167] William A Johnson. Reaction kinetics in process of nucleation and growth. *Transaction of AIME*, 135:416–458, 1939.

[168] YH Li, C Yang, LM Kang, HD Zhao, SG Qu, XQ Li, WW Zhang, and YY Li. Non-isothermal and isothermal crystallization kinetics and their effect on microstructure of sintered and crystallized tinbzrtasi bulk alloys. *Journal of Non-crystalline Solids*, 432:440–452, 2016.

[169] C Yang, LH Liu, YG Yao, YH Li, and YY Li. Intrinsic relationship between crystallization mechanism of metallic glass powder and microstructure of bulk alloys fabricated by powder consolidation and crystallization of amorphous phase. *Journal of Alloys and Compounds*, 586:542–548, 2014.

[170] JS Blázquez, CF Conde, and A Conde. Non-isothermal approach to isokinetic crystallization processes: application to the nanocrystallization of hitperm alloys. *Acta Materialia*, 53(8):2305–2311, 2005.

[171] Mihai Stoica, Ran Li, Alain Reza Yavari, Gavin Vaughan, Jürgen Eckert, Nele Van Steenberge, and Daniel Ruiz Romera. Thermal stability and magnetic properties of fecobsinb bulk metallic glasses. *Journal of Alloys and Compounds*, 504:S123–S128, 2010.

[172] ME McHenry, F Johnson, H Okumura, T Ohkubo, VRV Ramanan, and DE Laughlin. The kinetics of nanocrystallization and microstructural observations in finemet, nanoperm and hitperm nanocomposite magnetic materials. *Scripta Materialia*, 48(7):881–887, 2003.

[173] ON Senkov and DB Miracle. Effect of the atomic size distribution on glass forming ability of amorphous metallic alloys. *Materials Research Bulletin*, 36(12):2183–2198, 2001.

[174] Z. P. Lu, C. T. Liu, and W. D. Porter. Role of yttrium in glass formation of fe-based bulk metallic glasses. *Applied Physics Letters*, 83(13):2581–2583, 2003.

[175] Qingjun Chen, Deliang Zhang, Jun Shen, Hongbo Fan, and Jianfei Sun. Effect of yttrium on the glass-forming ability of fe–cr–mo–c–b bulk amorphous alloys. *Journal of Alloys and Compounds*, 427(1):190–193, 2007.

[176] F. R. Deoboer, R Boom, W. C. M. Mattens, A. R. Miedema, and A. K. Niessen. Cohesion in metals: transition metal alloys. *Cohesion in Metals (Amsterdam: North-Holland)*, 1, 1988.

[177] Tanaji Paul and Sandip P Harimkar. Initial stage densification during spark plasma sintering of fe-based amorphous alloy powder: Analysis of viscous flow. *Journal of Applied Physics*, 120(13):134901, 2016.

[178] Hung M Ha and Joe H Payer. Devitrification of fe-based amorphous metal sam 1651:

a structural and compositional study. *Metallurgical and Materials Transactions A*, 40(11):2519–2529, 2009.

[179] Sameehan S Joshi, Anna V Gkriniari, Shravana Katakam, and Narendra B Dahotre. Dynamic crystallization during non-isothermal laser treatment of fe–si–b metallic glass. *Journal of Physics D: Applied Physics*, 48(49):495501, 2015.

[180] Maria Jazmin Duarte, Aleksander Kostka, Jose Antonio Jimenez, P Choi, Julia Klemm, Daniel Crespo, Dierk Raabe, and Frank Uwe Renner. Crystallization, phase evolution and corrosion of fe-based metallic glasses: An atomic-scale structural and chemical characterization study. *Acta materialia*, 71:20–30, 2014.

[181] A Shamimi Nouri, Y Liu, and JJ Lewandowski. Effects of thermal exposure and test temperature on structure evolution and hardness/viscosity of an iron-based metallic glass. *Metallurgical and Materials Transactions A*, 40(6):1314–1323, 2009.

[182] Abderrezak Bouchareb, Badis Bendjemil, Rafael Piccin, and Marcello Baricco. Influence of rare-earth substitution for iron in fecrmocb bulk metallic glasses. *Chinese Physics Letters*, 27(7):076103, 2010.

[183] PR Jemian, JR Weertman, GG Long, and RD Spal. Characterization of 9cr-1movnb steel by anomalous small-angle x-ray scattering. *Acta Metallurgica et Materialia*, 39(11):2477–2487, 1991.

[184] Baohui Tian, Oskar Paris, Gerald A Zickler, Christoph Lind, Gregor Wasle, and

Roland P May. Sans investigation of phase separation in hot-deformed nimonic 80a. *Scripta Materialia*, 47(1):25–30, 2002.

VITA

Tanaji Paul

Candidate for the Degree of:

Doctor of Philosophy

Dissertation: Structural Evolution During Spark Plasma Sintering, Oxidation and Crystallization of Iron-Based Metallic Glass

Major Field: Mechanical Engineering

Biographical:

Education: Completed the requirements for Doctor of Philosophy in Mechanical Engineering at Oklahoma State University, Stillwater, Oklahoma in May, 2019.

Completed the requirements for Master of Engineering in Materials Engineering at Indian Institute of Science, Bangalore, India in June, 2014.

Completed the requirements for Bachelor of Engineering in Metallurgy and Materials Engineering at Bengal Engineering and Science University, Shibpur, India in July, 2012.

Experience: Employed by Oklahoma State Univeristy in the position of Research Associate in Stillwater, Oklahoma from August, 2015 to date.